

UC Santa Barbara

UC Santa Barbara Electronic Theses and Dissertations

Title

Strategies for Tailoring the Mechanical Response of Lattices and Foams

Permalink

<https://escholarship.org/uc/item/7fs8p450>

Author

Ruschel, Amanda L.

Publication Date

2023

Supplemental Material

<https://escholarship.org/uc/item/7fs8p450#supplemental>

Peer reviewed|Thesis/dissertation

UNIVERSITY OF CALIFORNIA
Santa Barbara

**Strategies for Tailoring the Mechanical Response of Lattices and
Foams**

A dissertation submitted in partial satisfaction
of the requirements for the degree

Doctor of Philosophy
in
Materials

by

Amanda Leigh Ruschel

Committee in charge:

Professor Frank Zok, Chair

Professor Matthew Begley

Professor Daniel Gianola

Professor Elliot Hawkes

March 2023

The dissertation of Amanda Leigh Ruschel is approved.

Professor Matthew Begley

Professor Daniel Gianola

Professor Elliot Hawkes

Professor Frank Zok, Committee Chair

March 2023

Strategies for Tailoring the Mechanical Response of Lattices and Foams

Copyright © 2023

by

Amanda Leigh Ruschel

Acknowledgements

I would like to express my sincere gratitude to my advisor Frank Zok for granting me the opportunity to solve interesting and challenging problems, for encouraging my creativity during this journey, and for providing invaluable guidance along the way. He has been instrumental in teaching me how to refine and effectively communicate my ideas in both writing and illustrations. I could not have asked for a better mentor.

I would also like to thank my colleagues at UCSB for their guidance and support. In particular, I want to thank Matt Begley for his enthusiastic support and indispensable mechanics knowledge. Our conversations always left me energized and ready to tackle a new challenge. I also want to thank my committee members, Dan Gianola and Elliot Hawkes, for their continued guidance on my research and for sharing their time and expertise. Thanks also to Peter Maxwell and Kirk Fields for their help overcoming obstacles in the lab.

I would also like to express my deepest appreciation to the Zok group for their enthusiasm toward my research despite it being drastically different from their own and for their constant support during the inevitable highs and lows of grad school. In particular, I want to thank Victoria Christensen, Collin Holgate, Maddie McAllister and Lauren Poole for their valuable friendship and for making this journey so wonderful. I also want to thank my closest friend Marissa Karl for her support and encouragement in my personal and academic pursuits.

Finally, I want to thank my parents Robert and Mary Jo Ruschel, my siblings Jessica and William, and my partner Liam Dow for their love and unwavering support. I would not have been able to do this without them.

* * *

I gratefully acknowledge financial support from the Institute for Collaborative Biotechnologies (Task 51: Structural Materials with Enhanced Resilience and Response Properties, Award Number W911NF-09-D-0001-0051).

Curriculum Vitae

Amanda Leigh Ruschel
March 2023

Education

2023 Ph.D. Materials, University of California, Santa Barbara

2022 Graduate Certificate in Technology Management University of California, Santa Barbara

2017 B.S. Materials Science & Engineering, Lehigh University

Publications

1. **Amanda L. Ruschel**, Avery F Samuel, Marco Colin Martinez, Matthew R Begley, and Frank W Zok. "A 3D bi-material lattice concept for tailoring compressive properties." *Materials & Design* 224 (2022): 111265.
2. **Amanda L. Ruschel** and Frank W. Zok. "A bi-material concept for periodic dissipative lattices." *Journal of the Mechanics and Physics of Solids* 145 (2020): 104144.

In Preparation

3. **Amanda L. Ruschel**, J. William Pro, Matthew R Begley, and Frank W Zok. "Effects of Microstructure on the Deformation and Mechanical Response of Elastomeric Foams"

Oral Presentations

1. **Ruschel, A.**, Zok, F.W., Begley, M. *Design Considerations and Performance of Bi-Material Lattices*. Materials Research Society (MRS) Spring Meeting (April 2021)
2. **Ruschel, A.** and Zok, F.W. Tailoring the Response of Bi-material Lattices. Soft Robotics Seminar, UC Santa Barbara (January 2020)
3. **Ruschel, A.** and Zok, F.W. Structure and Properties of Multi-material Lattices. Soft Robotics Seminar, UC Santa Barbara (August 2019)

Abstract

Strategies for Tailoring the Mechanical Response of Lattices and Foams

by

Amanda Leigh Ruschel

Cellular structures, including stochastic foams and ordered lattices, have been used extensively in a wide range of engineering applications. The nearly-constant crushing stress of stochastic foams make them particularly useful for energy absorption. Ordered lattices, on the other hand, are better suited for stiff and strong load-bearing components. Despite their higher strength, ordered lattices fail by internal buckling and exhibit concurrent strain softening during compressive loading, making them undesirable for energy absorption applications. The performance gaps between existing stochastic foams and ordered lattices appear large and motivate the current work.

The overarching goal of this work is to identify design strategies for tailoring the compressive properties of cellular structures, targeting in particular concepts that provide combinations of high strength and high straining capacity. A two-pronged approach is employed. The first involves ordered *bi-material* lattices in which material choices are based on local mechanical requirements. The issues are addressed through a combination of analytical models, finite element simulations, and experimental studies on select lattice structures. Two broad classes of bi-material lattices are introduced: one in 2D and one in 3D. The study on 2D lattices focuses on identifying and analyzing a primitive structural motif and demonstrating the concept by printing and testing rudimentary 2D designs. The ensuing results yield guidelines for bi-material lattice design (to mitigate the most common failure modes) and

highlight deficiencies in the nature of macroscopic straining and in joint design. The study on the 3D versions addresses some of these deficiencies. The focus is specifically on design of joints to facilitate articulation over a wide rotational range and the morphology of structural elements that enable strain reversibility. It also examines the potential for tailoring the topology and morphology of the structural elements to improve load bearing capacity. Structures that combine struts with plate elements appear to exhibit the greatest potential. The studies on both 2D and 3D bi-material lattices demonstrate how emergent multi-material printing capabilities can be exploited in expanding the design space for future lattice materials.

The second prong focuses on the connections between specific microstructural features of stochastic foams and mechanical response. This is done by computationally generating a large number of stochastic foams, analyzing various microstructural characteristics, and simulating their compressive response. Results indicate that cell size polydispersity governs the compressive response of foams. Foams with tight distributions in cell size exhibit stronger responses but are also more sensitive to boundary conditions and finite foam dimensions. This work offers insight into variables that must be considered when tailoring the response of foams including cell size polydispersity, number of cells spanning a unit dimension, and boundary conditions.

Table of Contents

Curriculum Vitae	vi
Abstract	vii
Table of Contents	ix
List of Figures	xi
List of Tables	xiii
Chapter 1 Introduction	1
1.1 Cellular Structures	1
1.2 Open-cell Stochastic Foams	2
1.3 Open-cell Lattices	5
1.4 3D Printing Methods	8
1.5 Dissertation Objectives and Outline	9
Chapter 2 A Bi-Material Concept for Periodic Dissipative Lattices	22
2.1 Introduction	22
2.2 Bi-Material Lattice	27
2.2.1 A Primitive Structural Motif	27
2.2.2 Bi-material Lattice Based on the Primitive Motif	30
2.3 Compressive Response.....	31
2.3.1 Methods	31
2.3.2 Measurements and Analysis of Single-Material Lattices	33
2.3.3 Experimental Measurements on Bi-Material Lattices	35
2.3.4 Analytical Model of Bi-material Lattice Response	37
2.4 Assessment of Analytical Models and FEA.....	41
2.5 Summary and Conclusions	43
2.A Appendix	45
2.A1 Response of Primitive Structural Motif	45
2.A2 Young’s Moduli of Bi-material Triangulated Lattices	46
Chapter 3 A 3D Bi-material Lattice Concept for Tailoring	
Compressive Properties.....	64
3.1 Introduction	65
3.2 Bi-material Lattice Design	69
3.2.1 Primitive Motif and Mechanics Analysis	69
3.2.2 Concept Implementation	70
3.3 Concept Assessment	71
3.3.1 Materials and Test Methods	71
3.3.2 Finite Element Simulations	72
3.3.3 Analytical Model	73
3.3.4 Experimental Measurements and Analytical Model Predictions	74

3.3.5 Finite Element Analysis	75
3.4 Concept Variations	77
3.4.1 Preliminaries	77
3.4.2 Lattices with Curved Struts	77
3.4.3 Preliminary Analysis of Sheet-based Designs	80
3.4.4 Implementation and Assessment of Sheet-based Designs	82
3.4.5 Tiling Concepts	84
3.5 Conclusions	84
3.A Appendix: Deformation and Failure Analysis of Lattices with Straight Struts	86
3.A1 Primitive Structural Motif	86
3.A2. FiniteLattice Structures	88
3.B Appendix: Arruda-Boyce Hyperelastic Constitutive Law	90
3.C Appendix: Analysis of Lattices with Curved Struts	91
3.C1 Primitive Structural Motif	91
3.C2. Finite Lattice Structures	92
Chapter 4 Effects of Microstructure on the Deformation and	
Mechanical Response of Elastomeric Foams.....	107
4.1 Introduction	107
4.2 Foam Microstructures	111
4.2.1 Real Foam Microstructures	112
4.2.2 Regularized Voronoi Foams	113
4.2.3. Bubble Growth Algorithm	114
4.3 Scope of the Study and Numerical Approach	116
4.4 Results and Discussion	119
4.4.1 A Comparison of Cell Geometry Distributions of Different Foam Types...	119
4.4.2 Mechanical Response of Different Foam Types	120
4.3 Microstructural Features that Impact Foam Response	123
4.4 Impact of Foam Aspect Ratio on Response	127
5. Conclusions	129
Appendix 4.A: Microstructure Analysis of Real Foams	135
Appendix 4.B: Finite Element Simulations Supplementary Material	135
Appendix 4.C: Deformation and Response of Honeycombs	136
Appendix 4.D: Bending and Stretching Energy Partitioning for Each Foam Type	137
Chapter 5 Conclusions and Recommendations	163
5.1 General Conclusions and Impact	163
5.2 Future Work	168

List of Figures

1.1 Four categories of cellular structures	20
1.2 Examples and illustrations of four lattice characteristics	21
2.1 Comparison between single-material lattices and tensegrities	54
2.2 Compressive deformation of a primitive bi-material structural motif	54
2.3 Design guidelines for a primitive bi-material structural motif	55
2.4 Design and idealized deformation of multi-cell bi-material lattice	56
2.5 Photographs of 3D printed single material and bi-material lattices	57
2.6 Tensile stress-strain response and material properties of constituent materials	57
2.7 Stress-strain curves and deformation of single and bi-material lattices	58
2.8 Compressive responses of bi-material lattices compared to results from the analytical and FE predictions	59
2.9 Full field rotation maps and measurements at bi-material joints	60
2.10 Surface node displacement measurements plotted against analytical and FE predictions	61
2.11 Measured strut tensile strains plotted against analytical predictions	62
2.12 Design guidelines for bi-material lattices having finite sized nodes	62
2.A1 Geometries of triangulated lattices in compression with internal force distributions	63
3.1 Examples and illustrations of multi-material lattice characteristics	97
3.2 Design and predicted response of a 3D bi-material structural motif	98
3.3 3D rendering of bi-material structure and photograph of 3D printed sample	98
3.4 Tensile stress-strain response of constituent materials	99
3.5 3D rendering of bi-material structure highlighting pertinent dimensions	99

3.6 Compressive response of bi-material structures plotted with analytical and FE predictions	100
3.7 Measured rotations of lattice components compared to analytical and FE predictions	101
3.8 Modified bi-material structures with predicted and measured compressive responses	102
3.9 Measured responses and accompanying strain maps of modified bi-material structures	103
3.10 Uniaxial and biaxial response of various Arruda-Boyce elastomers	104
3.11 Photographs and measured responses of sheet-based bi-material structures	104
3.12 Strain energy density distributions within strut and sheet-based designs	105
3.13 Photographs and diagrams of failure sites in sheet-based bi-material structures	106
4.1 Illustrations of foam microstructures and typical stress-strain responses	139
4.2 Image analysis of real foam microstructure	140
4.3 Microstructure analysis of real foams using a multivariate density plot	141
4.4 Illustrative example of the bubble growth algorithm	142
4.5 Evolution of microstructural characteristics with bubble growth	143
4.6 Multivariate density plots for synthetic foam models	144
4.7 Multivariate density plots for synthetic foams having different cell dimensions	145
4.8 Compressive stress-strain results for synthetic foam models	146
4.9 Stress-strain response of foams generated using regularity parameters	146
4.10 Comparison of measured Young's modulus and characteristic stress of foams	147
4.11 Normalized tangent moduli measurements for each foam type	148
4.12 Probability density functions and strain energy maps for 30x30 cell foams	149
4.13 Plots showing the relationship between cell size and normalized energy	150

4.14	Probability density functions and strain energy maps for 10x10 cell foams	151
4.15	Compressive stress-strain results for foams with different aspect ratios	152
4.16	Probability density functions and deformation maps of Honeycomb 90 foams	153
4.17	Probability density functions and deformation maps of Honeycomb 0 foams	154
4.18	Probability density functions and deformation maps of bubble growth foams	155
4.19	Probability density functions and deformation maps of Voronoi foams	156
4.A1	Multivariate density plots for real foam microstructures	157
4.B1	Images of foam models used in finite element simulations	158
4.B2	Images of foam models with different aspect ratios used in FE simulations ...	159
4.B3	Mesh convergence studies on two foam types	160
4.B4	Results from foam simulations using frictionless and fixed platens	161
4.C1	Stress-strain curves for 30x30 cell honeycombs marked with points of interest	161
4.D1	Total bending and stretching stress components for each foam type	162

List of Tables

2.1	Nomenclature	53
4.1	Summary of results from previous foam studies	138

Chapter 1

Introduction

1.1 Cellular Structures

Cellular structures are made up of networks of interconnected struts or plates. They provide excellent energy absorbing capabilities when structural elements are distributed in a non-periodic manner or when nodal connectivity is low ¹. When elements are distributed in a periodic manner with high nodal connectivities, stiffness and strength of the structure can exceed that of a stochastic foam by a factor of 10^2 . Due to advancements in additive manufacturing, cellular structures with precisely defined features are found in many applications. In biomedical products such as cellular bone implants ³, the structural stiffness of the implants can be tailored to match that of bone, thereby reducing stress shielding ⁴⁻⁶. Its open structure also allows for bone ingrowth, improving integration of bone into the implant ^{5,7}. In aerospace and automotive components, cellular structures are designed to lightweight parts leading to reduced fuel consumption ⁸⁻¹². In athletic applications such as footwear, structures can be designed for improved running patterns ¹³ and can be customized for individual needs ^{14,15}. These are only a few of the many applications.

Cellular structures can be placed into one of four categories based on internal order and constituent structural elements. Structures made up of networks of randomly-oriented cells that are sealed off from their neighbors are *closed-cell stochastic foams* (Fig. 1.1a). In this case, thin plates make up each cell wall. When closed-cell structures have internal order, meaning they are created by a repeating unit cell, they fall under the category of *closed-cell periodic lattices* (Fig. 1.1b.). Cellular structures made up of randomly-oriented cells connected by open space are *open-cell stochastic foams* (Fig. 1.1c). In this case, cells are defined by collections

of struts instead of plates. Adding order to open cell structures results in *periodic open-cell lattices* (Fig. 1.1d).

1.2 Open-cell Stochastic Foams

Stochastic foams are commonly used for impact mitigation. When loaded in compression, open-cell foams exhibit, first, a linear elastic region, dominated by strut bending, and then a transition to a nearly constant crushing stress, useful for keeping stresses below critical levels to prevent injury or damage. Polymer foams are commonly produced by processes involving nucleation and growth of gas bubbles. Gas can be introduced into the polymer liquid by (i) chemical blowing agents that react with isocyanate groups to form CO₂ or (ii) physical blowing agents like compressed gases and volatile liquids such as N₂, CO₂, ketones and alcohols that vaporize from the heat generated by the exothermic polymerization reaction¹⁶. Then, the nucleated gas bubbles grow and sometimes merge with another, especially when size differences between bubbles are large^{17,18}. Bubble growth is then stabilized by cooling or by the presence of surfactants¹⁷. The scalability¹⁹ of foam production coupled with the energy absorbing capabilities of foams make them widely used in applications such as cushioning and packaging^{20,21} and sporting gear, including helmets, pads, and shoes²²⁻²⁴.

Estimates of foam properties can be obtained by analyzing unit cells of prototypical bending-dominated structures, e.g., hexagonal cells for 2D and cubic cells for 3D. From these analyses, the Young's moduli of open-cell foams in axial compression are given by $E^* / E_s \approx \bar{\rho}^{-2}$ for 3D foams and $E^* / E_s \approx 1.5\bar{\rho}^{-3}$ for 2D foams. Here, E^* and E_s are the Young's modulus of the foam and constituent material, respectively. Relative density, $\bar{\rho}$, is the ratio between the density of the foam, ρ^* , and the density of the constituent material, ρ_s (

$\bar{\rho} = \rho^* / \rho_s$). Scaling relations for elastic collapse are $\sigma_{el} / E_s \approx 0.05 \bar{\rho}^{-2}$ for 3D foams and $\sigma_{el} / E_s \approx 0.14 \bar{\rho}^{-3}$ for 2D ²⁰. Here σ_{el} is the stress that causes the foam to collapse by elastic buckling. While useful, these scaling relations neglect microstructural details found in real foams, resulting in discrepancies in the scaling coefficients obtained from experiment and from the analyses ^{20,25,26}. Although the impact of cell structure on foam response is generally acknowledged, connections between microstructural features and mechanical response are poorly understood.

Work to date on connecting foam microstructure to mechanical response has focused on simulating the response of representative volume elements (RVEs) of foams ²⁷⁻³⁴. Here, an RVE is a geometric model having the smallest dimensions or smallest number of cells that produces results representative of a continuum foam. Analyses of RVEs are useful for reducing the computational cost of nonlinear simulations and providing a sound understanding of microstructural effects in large foams. However, the utility of RVEs diminish when the number of cells that span a component dimension become small. In helmet liners and running shoes, for example, tens of cells can span part dimensions. This motivates studying the combined effects of microstructure, number of cells and boundary conditions on foam response.

To capture random variations in foam microstructures, methods of computationally generating foams have been based on Voronoi tessellations made from points in 2D or 3D space coupled with a regularity parameter that governs the minimum allowable distance between the seed points in the point array ^{29-31,33,34}. The degree of regularity has been shown to influence the mechanical response, especially in foams with low relative density (1-10%). At low strains, conflicting conclusions have been made about how irregularity impacts the

stiffness of a foam ^{30,34}. For example, some studies have shown that foams with irregular microstructures exhibit stiffnesses between 25% ²⁹ and 66% ³⁰ *higher* than hexagonal honeycombs. Other studies have shown that foams with irregular microstructures exhibit stiffnesses from 3%³⁴ to as much as 40%³⁵ *lower* than ordered honeycombs. At higher compressive strains, studies show wide agreement that as microstructure irregularity increases, the collapse stress decreases. For example, the elastic collapse stress of highly irregular foams has been shown to be about half that of ordered honeycombs ³⁶.

While many studies have demonstrated that regularity affects certain features of the compressive response ^{30,32–34,36–42}, they have not precisely identified the governing microstructural features nor explained how they cause property differences. In one study, Zhu et al. ²⁹ suggest that the effective Young's modulus can be related to cell size distribution, although they do not explain the connection between this distribution and foam stiffness. Additionally, the authors state that other geometric properties may affect the response. Indeed, studies have shown that irregularity affects many different microstructural features including the number of struts per cell, cell interior angles, strut lengths, cell perimeters, and cell areas ⁴³. Studies investigating the effects of irregularity on collapse stress of foams also have not clearly identified governing microstructural features that cause differences in response. Instead, most studies explain that more irregular foams may behave similarly to springs in series ^{33,36,42}, meaning, cells experience the same compressive stress but different compressive strains leading to a weaker response. However, the reason for this proposed behavior has not been elucidated.

Complementary studies have examined the effects of specific microstructural features on the compressive response. Recently, a study looked at the effects of cell size polydispersity

on the response of open-cell 3D foams⁴⁴. The study concluded that as polydispersity increases both the elastic modulus and the collapse stress decrease. A foam with the largest variation in cell size exhibited a compressive strength 33% lower than a monodisperse foam⁴⁴. While the study further concludes that polydispersity in cell size leads to a stable response, connections between cell size and features like Young's modulus and collapse stress were not investigated. The deficiencies in mechanistic understanding motivate the pursuit to better understand which specific features in regular and irregular microstructures govern the compressive response of foams.

1.3 Open-cell Lattices

Periodic lattices are useful alternatives to stochastic foams where high load bearing capacity is required. The structure of open cell periodic lattices can be defined by four characteristics. The first is *strut morphology*. This describes the length, shape, and cross section of the constituent struts (Fig. 1.2a). Strut morphology can include variations in cross section along the strut length (to minimize stress concentrations, for example^{45,46}), hollow struts (to improve buckling resistance^{47,48}), or composite struts consisting of thin-walled struts with a different material in the interior, to improve toughness⁴⁹ or damping⁵⁰. Strut morphology affects other features of a lattice such as strut slenderness ratio, t/l , where t and l are the thickness and length of struts.

The second characteristic is *node morphology*. This describes the dimensions and shape of the connection points between constituent elements (Fig. 1.2b). Nodes in open cell lattices are key structural features as they transmit load between adjoining struts. They can be particularly susceptible to failure if there are no accommodations made for the reduced load bearing area of nodes relative to that of the struts. The nodes otherwise are sites of elevated

stress⁵¹⁻⁵⁴. Design features known to reduce stress concentrations include fillets between struts and nodes⁵¹ and variations in strut cross section in which a disproportionate amount of material is placed near the nodes^{45,46}. Identifying design concepts to minimize stress concentrations at nodes while effectively transmitting loads through a lattice remains an important but relatively unexplored area of research.

The other two lattice characteristics describe the ways in which struts and nodes are arranged. The first of these is *network topology*, defined by the number of connections at a node. Lattices with several different network topologies are illustrated in Fig. 1.2c-e. The second of these, *network morphology*, defines the spatial relationship between node locations and orientations and lengths of struts (Fig. 1.2f-h). To demonstrate the latter two characteristics, Figures 1.2c and 2f show lattices that have the same network topology (4 connections at each node), but different network morphology. These characteristics are key to understanding connections between design and performance of periodic cellular structures.

In design of lattices for structural applications, network topology is arguably the most important characteristic. Depending on the number of strut connections at a node, strut elements can bear loads in one of two ways: through *bending* or through *stretching*. A sufficient condition for stretch-dominated behavior is given by Maxwell's criterion for static determinacy. It states that the unit cell of a 2D lattice with b struts and j frictionless joints will be stretch-dominated if $b - 2j + 3 \geq 0$; for a 3D lattice, the criterion is $b - 3j + 6 \geq 0$ ². For lattices with similarly situated nodes (meaning the internal structure appears identical from the vantage point of each node) the necessary and sufficient condition for stretch-dominated deformation is that the average connectivity Z at each node is at least 6 for 2D lattices and at least 12 for 3D lattices².

Bend- and stretch-dominated lattices exhibit distinctly different mechanical responses. Bend-dominated lattices exhibit low stiffness and strength, but, if composed of materials with high ductility, can accommodate large strains at nearly constant stress⁵⁵. This is important for impact applications where stresses must be maintained below safe levels, e.g., crash protection,⁵⁶ packaging, and helmets^{57,58}. In stretch-dominated lattices, loads are transmitted via axial tension/compression of the struts⁵⁵. These lattices exhibit higher stiffness and strength relative to bend-dominated lattices, making them better suited for applications that require high strength but not large straining capability.

The stiffness and yield strength of 3D stretch-dominated lattices scale linearly with relative density: $E^* / E_s \propto \bar{\rho}$ and $\sigma_{pl} / \sigma_y \propto \bar{\rho}$. Here, σ_{pl} is the plastic collapse stress, and σ_y is the yield stress of the constituent material. Bend-dominated lattices exhibit different scalings: $E^* / E_s \propto \bar{\rho}^{-2}$ and $\sigma_{pl} / \sigma_y \propto \bar{\rho}^{-1.5}$. These scalings reflect more compliant and weaker responses. The high strength of stretch-dominated lattices is usually offset by their limited straining capability. In stretch-dominated lattices made of ductile materials, compressive failure occurs by strut buckling which leads to rapid strain softening^{55,59}. This feature makes them undesirable for energy absorption applications.

Improving the straining capability of stretch-dominated lattices has been an area of interest in the lattice community^{52,60-63}. The overarching goal has been to identify design concepts that lead to both high compressive strength and high straining capacity. Potential solutions may lie between two structure types: single-material stretch-dominated periodic lattices and bi-material stretch-dominated tensegrities. As previously noted, single-material stretch-dominated lattices exhibit high stiffness and strength but low strain capacity. Tensegrity structures consist of two dissimilar element types: stiff, discontinuous struts that

carry compressive loads and compliant, pre-stressed cables or springs that carry only tensile loads ⁶⁴. To attain high macroscopic strains, the two structural elements are connected by pinned joints. Tensegrities generally exhibit a softer response (relative to periodic lattices) but can be deformed to higher strains. While experimental exploration of the intervening design space has been limited historically by manufacturing constraints, advances in 3D printing have enabled implementation of new concepts in multi-material lattice structures.

1.4 3D Printing Methods

Identifying, testing, and iterating on new lattice design concepts have been enabled by innovations in 3D printing. Focusing on polymer printing methods, photopolymer jetting, also known as Polyjet 3D printing, allows for multiple materials to be incorporated into a single print. Polyjet printers operate similarly to inkjet printers, but instead of using ink they use droplets of a photopolymer resin. After deposition, the droplets are cured by a trailing UV light ⁶⁵. Multiple print heads allow for multi-material printing of disparate types of polymers. An alternative method for 3D printing recently developed by Carbon (Carbon DLS™) involves Continuous Liquid Interface Production (CLIP), also referred to as Digital Light Synthesis (DLS). The method utilizes an oxygen-permeable window with an ultraviolet image projected into a liquid resin. What sets this printing method apart from methods based on stereolithography is the “dead zone” of uncured resin created by oxygen permeation through the window ⁶⁶. Only tens of microns thick, the dead zone enables continuous printing without the conventional layer-by-layer printing. The high print speeds – 5 to 10 times greater than that of the fastest high-resolution printer ⁶⁷ – facilitate economical high-volume manufacturing.

In addition to increased print speed, material advancements have been made in dual-cure resins. These resins have a UV-curable component which is activated during DLS printing

and a thermally-curable component which is activated in a subsequent thermal bake ⁶⁸. The thermally curable component is a critical innovation that yields material properties that are superior to those of single-cure resins. In some cases, UV curable resins are subjected to a second post-print “flood curing” which continues the same reaction. While this two-step single-mode curing method may provide some benefit to the manufacturing process and yield some property improvements, the resulting materials remain inferior to those made with dual-cure resins.

The combined advancements in print speed and print material make Carbon DLS printing well-suited for relatively large-scale production. Indeed, commercialized lattice products from companies like Adidas, Osprey, and Fizik have made it successfully to market. This is only the beginning. A new printing method, iCLIP, combines the rapid printing speed and incredible resolution of Carbon DLS with the multimaterial printing capabilities of Polyjet ⁶⁹. Additional advancements in 3D printing will undoubtedly help to reduce costs and increase manufacturing capacity while also enabling implementation of previously infeasible design concepts. However, lattice concepts that can fully exploit these technologies remain largely unexplored.

1.5 Dissertation Objectives and Outline

The goals of this research are twofold. The first is to identify design strategies for tailoring the compressive properties of lattices, targeting concepts that provide combinations of high strength and high straining capacity. The second goal is to establish connections between microstructural features of stochastic foams and resultant mechanical properties, including stiffness, collapse stress, and strain-dependent tangent modulus. These goals are pursued through a combination of (i) analytical mechanics models to predict compressive responses,

(ii) 3D printing to produce test samples, (iii) mechanical testing in conjunction with digital image correlation (DIC) to understand overall response and deformation mechanisms, and (iv) finite element analyses to interpret the experimental measurements and to probe a broader range of structures.

The dissertation is organized in the following way: Chapter 2 focuses on identifying and analyzing 2D bi-material lattices that allow for high strength and straining capability. In this design, material choices are based on local mechanical requirements. To begin, a primitive structural motif that exhibits the desired response is identified and an analytical model is used to make connections between structural features and response. Then, the design is extended to multi-cell experimental samples that are printed, tested, and analyzed. Results of experiments are compared to analytical and numerical models in order to develop guidelines for design of bi-material structures that mitigate the most common failure modes. Experimental results also highlight deficiencies in the nature of macroscopic straining and in joint design.

In Chapter 3, the bi-material concept is extended to 3D. Here, some of the deficiencies of the 2D lattice are addressed. The focus is specifically on design of joints to facilitate articulation over a wide rotational range and the morphology of structural elements that enable strain reversibility. Assessments of proposed structures are made by conducting experiments on 3D printed samples and comparing results to analytical models and finite element simulations. The successful performance of a strut-based unit cell affirms the importance of joint design in multimaterial lattices. The potential for tailoring the topology and morphology of the structural elements to improve load bearing capacity is also examined. The studies on both 2D and 3D bi-material lattices demonstrate how emergent multi-material printing capabilities may be exploited in the future in expanding the design space for lattice materials.

In Chapter 4, the focus shifts to stochastic foams, specifically the connections between microstructural features and mechanical response. This is done by computationally generating a large number of stochastic foams, analyzing various microstructural characteristics, and simulating their compressive response. Finally, conclusions and recommendations for future research are presented in Chapter 5.

References

1. Nazir, A., Abate, K. M., Kumar, A. & Jeng, J. Y. A state-of-the-art review on types, design, optimization, and additive manufacturing of cellular structures. *Int. J. Adv. Manuf. Technol.* 104, (2019).
2. Deshpande, V. S., Ashby, M. F. & Fleck, N. A. Foam topology: Bending versus stretching dominated architectures. *Acta Mater.* 49, 1035–1040 (2001).
3. JP, H., MR, B. & JE, B. Truss implant technologyTM for interbody fusion in spinal degenerative disorders: profile of advanced structural design, mechanobiologic and performance characteristics. *Expert Rev. Med. Devices* 18, 707–715 (2021).
4. Liu, B. *et al.* Capability of auxetic femoral stems to reduce stress shielding after total hip arthroplasty. *J. Orthop. Transl.* 38, 220–228 (2023).
5. Liu, B., Wang, H., Zhang, N., Zhang, M. & Cheng, C. K. Femoral Stems With Porous Lattice Structures: A Review. *Frontiers in Bioengineering and Biotechnology* 9, (2021).
6. Murr, L. E. *et al.* Microstructure and mechanical properties of open-cellular biomaterials prototypes for total knee replacement implants fabricated by electron beam melting. *J. Mech. Behav. Biomed. Mater.* 4, 1396–1411 (2011).
7. Singh, R., Lee, P. D., Dashwood, R. J. & Lindley, T. C. Titanium foams for biomedical applications: A review. *Mater. Technol.* 25, (2010).
8. Harris, J. A., Winter, R. E. & McShane, G. J. Impact response of additively manufactured metallic hybrid lattice materials. *Int. J. Impact Eng.* 104, 177–191 (2017).
9. Moon, S. K., Tan, Y. E., Hwang, J. & Yoon, Y.-J. Application of 3D Printing

- Technology for Designing Light-weight Unmanned Aerial Vehicle Wing Structures. *Int. J. Precis. Eng. Manuf. Technol.* 1, 223–228 (2014).
10. Shapiro, A. A. *et al.* Additive manufacturing for aerospace flight applications. *Journal of Spacecraft and Rockets* 53, (2016).
 11. Aslan, B. & Yıldız, A. R. Optimum design of automobile components using lattice structures for additive manufacturing. *Mater. Test.* 62, 633–639 (2020).
 12. Chantarapanich, N. *et al.* Fabrication of three-dimensional honeycomb structure for aeronautical applications using selective laser melting: a preliminary investigation. *Rapid Prototyp. J.* 20, 551–558 (2014).
 13. Clermont, C. *et al.* The influence of midsole shear on running economy and smoothness with a 3D-printed midsole. *Sport. Biomech.* (2022).
doi:10.1080/14763141.2022.2029936
 14. Zolfagharian, A., Lakhi, M., Ranjbar, S. & Bodaghi, M. Custom Shoe Sole Design and Modeling Toward 3D Printing. *Int. J. Bioprinting* 7, (2021).
 15. Cheng, H., Liu, B., Liu, M. & Cao, W. Design of three-dimensional Voronoi strut midsoles driven by plantar pressure distribution. *J. Comput. Des. Eng.* 9, 1410–1429 (2022).
 16. Feldman, D. Polymeric foam materials for insulation in buildings. *Mater. Energy Effic. Therm. Comf. Build.* 257–273 (2010). doi:10.1533/9781845699277.2.257
 17. Jin, F. L., Zhao, M., Park, M. & Park, S. J. Recent trends of foaming in polymer processing: A review. *Polymers* 11, (2019).
 18. Tamaro, D. & Di Maio, E. Early bubble coalescence in thermoplastic foaming. *Mater. Lett.* 228, (2018).

19. Mills, N., Jenkins, M. & Kukureka, S. *Plastics: microstructure and engineering applications*. (Butterworth-Heinemann, 2020).
20. Gibson, L. J. & Ashby, M. F. *Cellular solids: structure and properties*. (Cambridge University Press, 1997).
21. Liu, P. S. & Chen, G. F. Applications of Polymer Foams. *Porous Mater.* 383–410 (2014). doi:10.1016/B978-0-12-407788-1.00008-3
22. Lyn, G. & Mills, N. J. Design of foam crash mats for head impact protection. *Sport. Eng.* 4, (2001).
23. Mills, N. J., Fitzgerald, C., Gilchrist, A. & Verdejo, R. Polymer foams for personal protection: Cushions, shoes and helmets. *Compos. Sci. Technol.* 63, 2389–2400 (2003).
24. Arton Tomin, M. & Kmetty, A. Polymer foams as advanced energy absorbing materials for sports applications-A review. (2021). doi:10.1002/app.51714
25. Ashby, M. F. *et al. Metal foams: a design guide*. (Butterworth-Heinemann, 2000). doi:10.1016/S0261-3069(01)00049-8
26. Fischer, F., Lim, G. T., Handge, U. A. & Altsädt, V. Numerical simulation of mechanical properties of cellular materials using computed tomography analysis. *J. Cell. Plast.* 45, (2009).
27. Silva, M. J. & Gibson, L. J. The effects of non-periodic microstructure and defects on the compressive strength of two-dimensional cellular solids. *Int. J. Mech. Sci.* 39, 549–563 (1997).
28. Van der Burg, M. W. D., Shulmeister, V., Van der Geissen, E. & Marissen, R. On the Linear Elastic Properties of Regular and Random Open-Cell Foam Models. *J. Cell.*

- Plast.* 33, 31–54 (1997).
29. Zhu, H. X., Hobdell, J. R. & Windle, A. H. Effects of cell irregularity on the elastic properties of 2D Voronoi honeycombs. *J. Mech. Phys. Solids* 49, 857–870 (2001).
 30. Sotomayor, O. E. & Tippur, H. V. Role of cell regularity and relative density on elasto-plastic compression response of random honeycombs generated using Voronoi diagrams. *Int. J. Solids Struct.* 51, 3776–3786 (2014).
 31. Alkhader, M. & Vural, M. Mechanical response of cellular solids: Role of cellular topology and microstructural irregularity. *Int. J. Eng. Sci.* 46, 1035–1051 (2008).
 32. Duan, Y. *et al.* The cell regularity effects on the compressive responses of additively manufactured Voronoi foams. *Int. J. Mech. Sci.* 164, 105151 (2019).
 33. Zhu, H. X. & Windle, A. H. Effects of cell irregularity on the high strain compression of open-cell foams. *Acta Mater.* 50, 1041–1052 (2000).
 34. Alsayednoor, J., Harrison, P. & Guo, Z. Large strain compressive response of 2-D periodic representative volume element for random foam microstructures. *Mech. Mater.* 66, 7–20 (2013).
 35. Sotomayor, O. E. & Tippur, H. V. Role of cell regularity and relative density on elastoplastic compression response of 3-D open-cell foam core sandwich structure generated using Voronoi diagrams. *Acta Mater.* 78, (2014).
 36. Zhu, H. X., Thorpe, S. M. & Windle, A. H. The effect of cell irregularity on the high strain compression of 2D Voronoi honeycombs. *Int. J. Solids Struct.* 43, 1061–1078 (2006).
 37. Ajdari, A., Nayeb-Hashemi, H., Canavan, P. & Warner, G. Effect of defects on elastic–plastic behavior of cellular materials. *Mater. Sci. Eng. A* 487, 558–567 (2008).

38. Zhu, H. X., Hobdell, J. R. & Windle, A. H. Effects of cell irregularity on the elastic properties of open-cell foams. *Acta Mater.* 48, 4893–4900 (2000).
39. Babaei, S., Jahromi, B. H., Ajdari, A., Nayeb-Hashemi, H. & Vaziri, A. Mechanical properties of open-cell rhombic dodecahedron cellular structures. *Acta Mater.* 60, (2012).
40. Liu, W., Wang, N., Huang, J. & Zhong, H. The effect of irregularity, residual convex units and stresses on the effective mechanical properties of 2D auxetic cellular structure. *Mater. Sci. Eng. A* 609, (2014).
41. Qi, C., Jiang, F. & Yang, S. Advanced honeycomb designs for improving mechanical properties: A review. *Composites Part B: Engineering* 227, (2021).
42. Shi, X., Liu, S., Nie, H., Lu, G. & Li, Y. Study of cell irregularity effects on the compression of closed-cell foams. *Int. J. Mech. Sci.* 135, (2018).
43. Zhu, H. X., Thorpe, S. M. & Windle, A. H. The geometrical properties of irregular two-dimensional Voronoi tessellations. *Philos. Mag. A Phys. Condens. Matter, Struct. Defects Mech. Prop.* 81, (2001).
44. Luan, S., Kraynik, A. M. & Gaitanaros, S. Microscopic and macroscopic instabilities in elastomeric foams. *Mech. Mater.* 164, (2022).
45. Al-Ketan, O. *et al.* Microarchitected Stretching-Dominated Mechanical Metamaterials with Minimal Surface Topologies. *Adv. Eng. Mater.* 20, 1800029 (2018).
46. Zhao, M. *et al.* Improved mechanical properties and energy absorption of BCC lattice structures with triply periodic minimal surfaces fabricated by SLM. *Materials (Basel)*. 11, (2018).
47. Wadley, H. N. G. Cellular metals manufacturing. *Adv. Eng. Mater.* 4, (2002).

48. Queheillalt, D. T. & Wadley, H. N. G. Pyramidal lattice truss structures with hollow trusses. *Mater. Sci. Eng. A* (2005). doi:10.1016/j.msea.2005.02.048
49. Mueller, J., Raney, J. R., Shea, K. & Lewis, J. A. Architected Lattices with High Stiffness and Toughness via Multicore–Shell 3D Printing. *Adv. Mater.* 30, 1705001 (2018).
50. Wehmeyer, S. C., Compton, B. G., Pro, J. W., Zok, F. W. & Begley, M. R. Damping in cellular structures made from composite struts and walls with elastic and viscoelastic phases. *J. Mech. Phys. Solids J. homepage* 145, 104106 (2020).
51. Latture, R. M., Rodriguez, R. X., Holmes, L. R. & Zok, F. W. Effects of Nodal Fillets and External Boundaries on Compressive Response of an Octet Truss. *Acta Mater.* 149, 78–87 (2017).
52. Hammetter, C. I., Rinaldi, R. G. & Zok, F. W. Pyramidal Lattice Structures for High Strength and Energy Absorption. *J. Appl. Mech.* 80, (2013).
53. Maskery, I. *et al.* A mechanical property evaluation of graded density Al-Si10-Mg lattice structures manufactured by selective laser melting. *Mater. Sci. Eng. A* 670, 264–274 (2016).
54. Smith, M., Guan, Z. & Cantwell, W. J. Finite element modelling of the compressive response of lattice structures manufactured using the selective laser melting technique. *Int. J. Mech. Sci.* 67, (2013).
55. Ashby, M. . The properties of foams and lattices. *Philos. Trans. R. Soc. A Math. Phys. Eng. Sci.* 364, 15–30 (2005).
56. Wang, C. Y. *et al.* Structure design and multi-objective optimization of a novel crash box based on biomimetic structure. *Int. J. Mech. Sci.* 138–139, (2018).

57. Jafferson, J. M. & Pattanashetti, S. Use of 3D printing in production of personal protective equipment (PPE) - A review. in *Materials Today: Proceedings* 46, (2021).
58. Clough, E. C. *et al.* Elastomeric Microlattice Impact Attenuators. *Matter* 1, (2019).
59. Zok, F. W. *et al.* A protocol for characterizing the structural performance of metallic sandwich panels: application to pyramidal truss cores. *Int. J. Solids Struct.* 41, 6249–6271 (2004).
60. Hammetter, C. I. & Zok, F. W. Compressive Response of Pyramidal Lattices Embedded in Foams. *J. Appl. Mech.* (2013). doi:10.1115/1.4024408
61. Bernal Ostos, J. *et al.* Deformation stabilization of lattice structures via foam addition. *Acta Mater.* (2012). doi:10.1016/j.actamat.2012.07.053
62. MT Hsieh, C. H. Z. X. S. K. V. K. X. Z. Stiff and strong, lightweight bi-material sandwich plate-lattices with enhanced energy absorption. *J. Mater. Res.* (2021). doi:10.1557/s43578-021-00322-2
63. Evans, A. G. *et al.* Concepts for enhanced energy absorption using hollow micro-lattices. *Int. J. Impact Eng.* 37, 947–959 (2010).
64. R.E. Skelton, M.C. Oliveira. *Tensegrity Systems*. (Springer, 2009).
65. Patpatiya, P., Chaudhary, K., Shastri, A. & Sharma, S. A review on polyjet 3D printing of polymers and multi-material structures. *Proc. Inst. Mech. Eng. Part C J. Mech. Eng. Sci.* 236, 7899–7926 (2022).
66. Tumbleston, J. R. *et al.* Continuous liquid interface production of 3D objects. *Science* (80-.). 347, (2015).

67. Firtina, N. Stanford's new 3D printing tech is up to 10 times faster than the quickest printer. *Interesting Engineering* (2022). Available at: <https://interestingengineering.com/innovation/stanfords-new-3d-printing-tech-10-times-faster>.
68. Poelma, J. & Rolland, J. Rethinking digital manufacturing with polymers. *Science* 358, (2017).
69. Lipkowitz, G. *et al.* Injection continuous liquid interface production of 3D objects. *Sci. Adv.* 8, 3917 (2022).
70. Deshpande, V. S., Fleck, N. A. & Ashby, M. F. Effective properties of the octet-truss lattice material. *J. Mech. Phys. Solids* 49, 1747–1769 (2001).
71. Berger, J. B., Wadley, H. N. G. & McMeeking, R. M. Mechanical metamaterials at the theoretical limit of isotropic elastic stiffness. *Nature* 543, 533–537 (2017).
72. Okolieocha, C., Raps, D., Subramaniam, K. & Altstädt, V. Microcellular to nanocellular polymer foams: Progress (2004–2015) and future directions - A review. *Eur. Polym. J.* 73, 500–519 (2015).
73. Zok, F. W. Integrating lattice materials science into the traditional processing-structure-properties paradigm. *MRS Commun.* 9, 1284–1291 (2019).

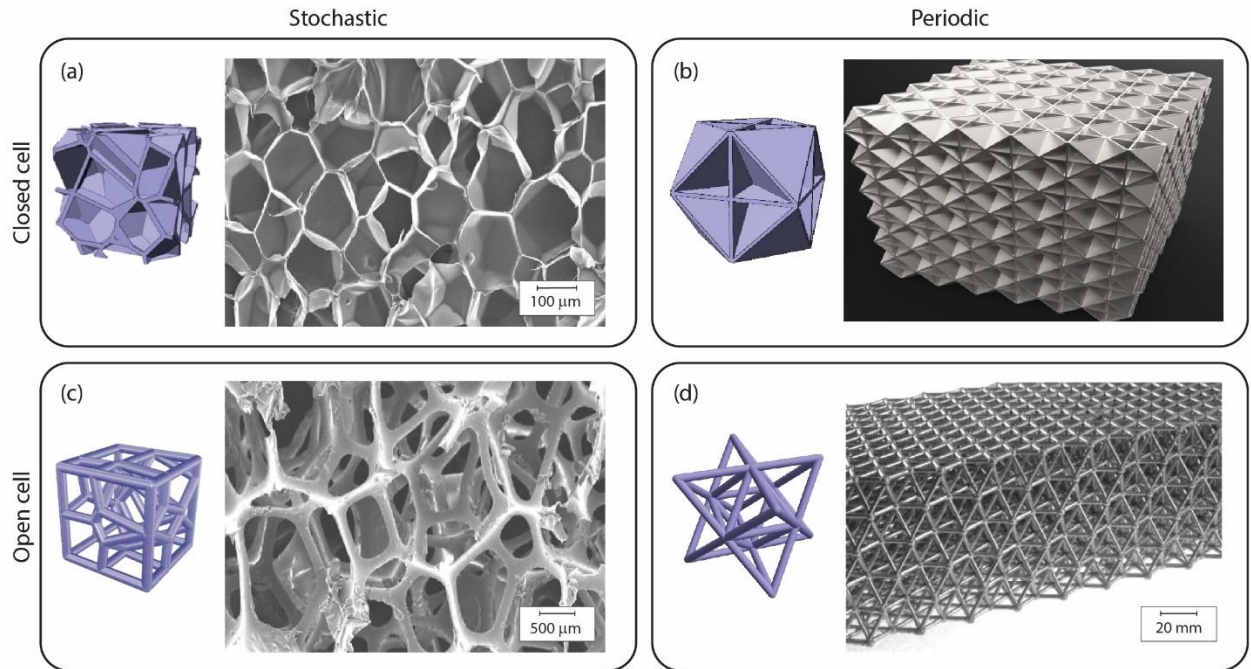


Figure 1.1: Four categories of cellular structures: (a) closed cell stochastic foam, (b) closed cell periodic lattice, (c) open cell stochastic foam, and (d) open cell periodic lattice. Adapted from V.S. Deshpande, N.A. Fleck, and M.F. Ashby; J.B. Berger, H. N. G. Wadley, and R. M. McMeeking; C. Okolieocha, D. Raps, K. Subramaniam, and V. Altstädt^{70–72} with permission from Springer Nature and Elsevier.

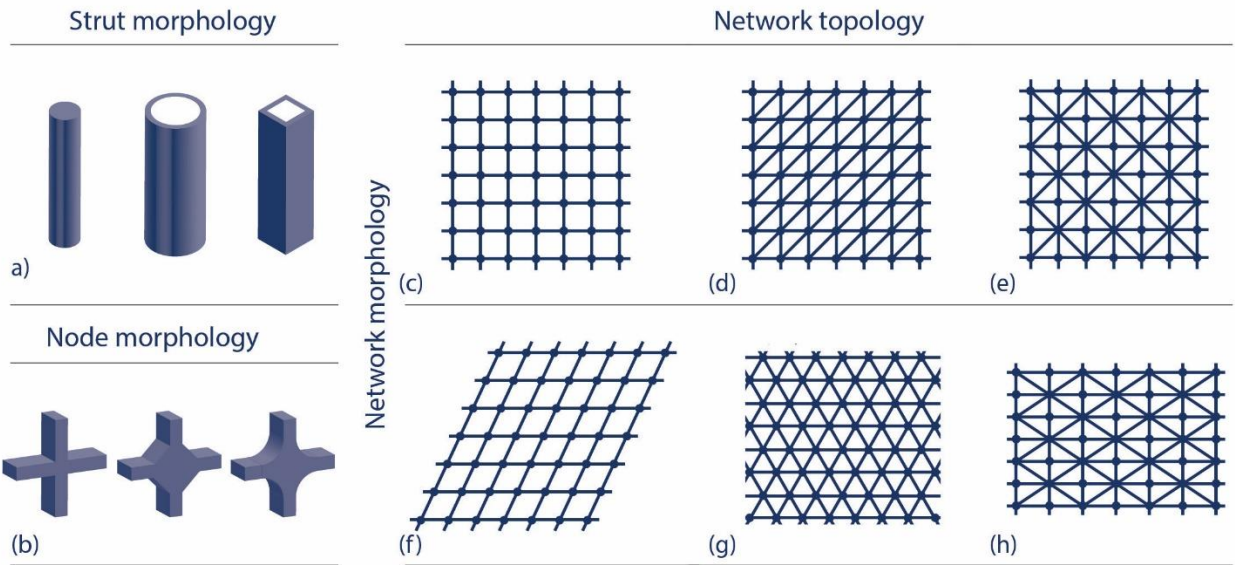


Figure 1.2: (a and b) Examples of strut and node morphologies. (c-e) 2D lattice network topologies with various nodal connectivities. (f-h) Lattices with the same network topologies as those in (c-e) but with variations in network morphologies. Adapted from Zok⁷³.

Chapter 2

A Bi-Material Concept for Periodic Dissipative Lattices

Abstract

¹Structural periodic lattices made of two or more dissimilar materials can be viewed conceptually in terms of a spectrum of structure types, bounded by stretch-dominated lattices of a single material at one end and tensegrities of tensile and compressive struts at the other. The present chapter probes the unexplored domain within this lattice-tensegrity spectrum with a focus on dissipative bi-material lattices. To begin, a primitive structural motif that exhibits the desired behavior is identified and its compressive response is analyzed. A 2D multi-cell lattice based on the primitive motif is designed and several material variants are fabricated and tested. Analysis of test results addresses effects of finite node dimensions, constraints on strut rotation at the nodes, free edges, and friction with the loading platens as well as limits dictated by rupture of tensile struts or buckling or yielding of compressive struts. The study culminates with guidelines on design of bi-material lattices with high strength and high straining capability.

2.1 Introduction

The elastic and plastic responses of periodic lattice materials are dictated by: (i) network *topology*, characterized by the nodal connectivity Z of the constituent struts; (ii) network *morphology*, defined by the spatial relationships between nodal locations and hence

¹ The content of this chapter has previously appeared in the Journal of the Mechanics and Physics of Solids (A.L. Ruschel and F.W. Zok, A bi-material concept for periodic dissipative lattices, *Journal of the Mechanics and Physics of Solids* (2020)). Available at: <https://doi.org/10.1016/j.jmps.2020.104144>

orientations and lengths of the struts; (iii) *strut morphology*, characterized by strut length and shape and dimensions of strut cross-sections; (iv) *node morphology*, characterized by node shape and dimensions; and (v) properties of the constituent materials ¹. When the nodal connectivity is low ($Z < 6$ in 2D and $Z < 12$ in 3D), some or all of the struts may deform through bending; when it is high, the struts deform by axial tension or compression ². The former is exemplified by in-plane loading of a 2D *hexagonal* honeycomb ($Z = 3$) and the latter by in-plane loading of a 2D *triangular* honeycomb ($Z = 6$). Hexagonal honeycombs exhibit low stiffness and strength but, if made of a ductile material, can accommodate large strains at nearly constant stress after yielding occurs^{3,4}. Triangular honeycombs, on the other hand, exhibit high stiffness and strength; but, when they fail, typically by strut buckling (either elastically or plastically), they undergo rapid strain softening. One of the outstanding challenges involves identifying lattice designs that are stiff and strong *and* have the capacity for large macroscopic deformation. Viewed more generally, strategies for *tailoring* the compressive response – beyond that obtained in purely bend-dominated or purely stretch-dominated lattices – would enable design of lattice materials for specific requirements of engineering components ⁵.

Design of lattices with high energy absorption capacity in particular has been of great interest, in part because of the wide range of applications requiring dissipative systems and in part because of the extraordinary developments in additive manufacturing that have greatly expanded the design options. One approach that has been pursued focuses on preventing or delaying buckling of compressive members in stretch-dominated lattices and exploiting the plastic straining capabilities of the strut materials while the struts are deformed in uniaxial compression ⁶. This strategy invariably leads to designs with stubby struts and hence high relative density. Alternatively, buckling of slender struts can be delayed by the addition of a

secondary structure comprising a low relative density foam or lattice at a finer length scale. Here the secondary structure provides lateral support to the struts and elevates the buckling load and, in turn, increases the propensity for axial yielding of the struts⁷. But the addition of the secondary structure comes at the expense of an overall increase in relative density. Even if the tradeoffs between the addition of a secondary structure and the increased strength are favorable, plastic buckling is likely to intervene and lead to strain softening at larger strains.

While the aim of the preceding approaches is to *inhibit* strut buckling, lightweight structures designed to *exploit* buckling instabilities for damping, dynamic energy dissipation or elastic energy trapping have also been pursued. The concept of utilizing instabilities for energy dissipation was first introduced by Lakes et al.⁸ in the context of damping in materials with negative stiffness inclusions. Subsequent work on structures that exhibit snap-through instabilities due to elastic buckling of constrained compressive members has been extensive^{9–25}. Such structures can be designed to undergo reversible snap-through, whereby the structure returns to its original configuration upon unloading and exhibits enhanced damping upon dynamic cyclic loading. Alternatively, intermediate states following a snap-through event can be locked in, thereby leading to energy trapping.

Yet another potential approach to tailoring properties of interest – especially stiffness, strength and energy absorption – involves integration of multiple materials into a single lattice structure. In essence, materials for the constituent struts would be selected to best match local mechanical requirements. The concept emerges from the recognition that, when periodic lattices are subjected to a macroscopically-uniform strain, the constituent struts experience strains that differ appreciably from the applied strain and differ among the various strut populations^{3,26–28}. For example, when a triangular honeycomb lattice is loaded elastically in

uniaxial compression, $2/3$ of the struts (those inclined at 30° to the loading direction) experience uniaxial *compression* and a strain equal to $2/3$ of the applied macroscopic strain; the remaining $1/3$ (oriented perpendicular to the loading direction) experience uniaxial *tension* and a strain equal to $-1/3$ of the applied strain. When, instead, the material is loaded in uniaxial tension, $2/3$ of the struts are in tension and $1/3$ are in compression. One of the implications is that, regardless of whether a stretch-dominated structure is loaded in tension or compression, some struts are always in tension while others are in compression. Consequently, *compressive* strength may be controlled by *tensile* rupture while *tensile* strength may be controlled by *compressive* buckling. In this context, the weaker of the two failure modes may dictate strength under *both* macroscopic tension and macroscopic compression. These behavioral characteristics suggest a bi-material strategy for attaining both high strength and high straining capacity *for a prescribed loading* (compression or tension). In this strategy, struts loaded in compression would be made from a stiff and strong material (to inhibit buckling) while those in tension would be made from a more compliant material with high tensile ductility. This strategy is the inverse of that used to generate snap-through instabilities in the sense that the macroscopic deformation is accommodated by internal strut stretching while buckling is prevented.

From a broader perspective, structural lattices made of two dissimilar materials can be viewed conceptually in terms of a spectrum of structure types, bounded by stretch-dominated lattices of a single material at one end and tensegrities at the other (Fig. 2.1). Tensegrities consist of discrete (non-touching) struts that carry compression and pre-stressed wires or springs that carry only tension²⁹. Together the constituents are mechanically stable and may be designed to exhibit a wide range of mechanical responses that could not be obtained by either

one of the two constituents alone. In the context of this conceptual lattice-tensegrity spectrum, a wide domain of material topology and material combination remains unexplored.

The present work is motivated in part by the recognition that some additive manufacturing technologies are capable of integrating two or more dissimilar materials into a single print operation³⁰. But if bi-material lattices are to be made in one operation (not through assembly of printed parts), special attention will need to be focused on how the materials are connected to one another at the nodal locations. The challenge involves striking a balance between the mechanical integrity of nodes (and hence the ability to transmit forces) and the need for articulation, to accommodate large macroscopic strains and accompanying rotations. A potential node design is presented in due course.

The main objective of this chapter is to present a bi-material concept for dissipative periodic lattice materials. To illustrate the behavioral type of interest, a primitive structural motif is identified, and its mechanical response is analyzed. The analysis yields insights into the trade-offs between structural properties (*i.e.* strength and straining capacity), geometry, and properties of the constituent materials. The primitive motif is used as the basis for design of a multi-cell 2D lattice. The design is implemented using additive manufacturing. Compression tests on lattices with several different material combinations along with high-resolution strain mapping via digital image correlation (DIC) are used to elucidate the nature of mechanical response both globally and locally. Analytical mechanical models (building on that for the primitive motif) are assessed through complementary finite element analyses (FEA) and are used both to interpret the experimental measurements and to identify designs that produce high strength and high straining capacity. (A comprehensive list of symbols is presented in Table 2.1.)

2.2 Bi-Material Lattice

2.2.1 A Primitive Structural Motif

A primitive 2D structural motif that exhibits the desired behavior is illustrated in Fig. 2.2. It consists of four inclined struts of equal length in a diamond pattern and a transverse strut joining two of the resulting nodes. The inclined struts are made of a stiff, strong material and the transverse strut from a highly extensible material. Under macroscopic compression (along the y-axis), load is distributed through axial compression of inclined struts and axial tension of the transverse strut.

The following analysis of the compressive response of this structural motif is based on the assumptions that: inclined struts are much stiffer than the transverse strut, nodes are pin-jointed, strut thicknesses are infinitesimal, and the transverse strut is elastomeric with linear stress-strain response. All results were checked by FEA with the same assumptions. Details of the analysis are present in Appendix 2.A1. The key results follow.

The macroscopic response is given by

$$\Phi_a = (1 - \varepsilon_a) \left[\tan \theta_0 - \left(\csc^2 \theta_0 - (1 - \varepsilon_a)^2 \right)^{-1/2} \right] \quad (2.1)$$

where Φ_a is the normalized force, $\Phi_a \equiv F_a / E_t t_t$, F_a is the applied force (per unit depth), E_t and t_t are the Young's modulus and the thickness of the transverse member, θ_0 is the initial strut inclination angle, ε_a is the nominal compressive strain defined by $\varepsilon_a = v / H_0$, v is axial displacement and H_0 is the initial height. The corresponding tensile strain ε_t in the transverse strut is

$$\varepsilon_t = \tan \theta_0 \left[\csc^2 \theta_0 - (1 - \varepsilon_a)^2 \right]^{1/2} - 1 \quad (2.2)$$

while the compressive force F_c within the inclined struts, expressed in the non-dimensional form $\Phi_c \equiv F_c/E_t t_t$, is:

$$\Phi_c = \frac{1}{2} \left[\sec \theta_0 - \left(1 - \sin^2 \theta_0 (1 - \varepsilon_a)^2 \right)^{-1/2} \right] \quad (2.3)$$

The maximum values of ε_t and Φ_c are obtained at $\varepsilon_a = 1$; they are $\varepsilon_t^{\max} = \sec \theta_0 - 1$ (from Eq. 2.2) and $\Phi_c^{\max} = (\sec \theta_0 - 1)/2$ (from Eq. 2.3). (Full densification, *i.e.* $\varepsilon_a = 1$, is obtained because of the assumed infinitesimal thicknesses of struts and nodes.)

Absent failure, the structural response, $\Phi_a(\varepsilon_a)$, exhibits: (i) a rising portion with an initial stiffness of $d\Phi_a/d\varepsilon_a = \tan^3 \theta_0$; (ii) a local maximum at a strain of $\varepsilon_a^{\max} = 1 - \csc \theta_0 \left(1 - \cos^{2/3} \theta_0 \right)^{1/2}$ and a force of $\Phi_a^{\max} = \left(\sec^{2/3} \theta_0 - 1 \right)^{3/2}$; and (iii) a softening portion ending at $\Phi_a = 0$ at $\varepsilon_a = 1$ (Fig. 2.3). The shape of the $\Phi_a - \varepsilon_a$ curves reflects two competing mechanisms: hardening due to stretching of the transverse strut and softening due to progressive reduction in inclination angle and hence reduced efficiency with which the tensile force in the transverse strut can be transmitted into macroscopic compression.

Attaining the full response through to densification relies on the transverse strut having a high tensile ductility, ε_t^* . If tensile rupture is to be avoided, the initial inclination angle must be below a critical value of $\theta_0^* = \sec^{-1} \left(1 + \varepsilon_t^* \right)$ (from Eq. 2.2, with $\varepsilon_a = 1$). Otherwise, if $\theta_0 > \theta_0^*$, tensile rupture precedes densification and, from Eq. 2.2, occurs at an applied strain of

$$\varepsilon_a^* = 1 - \csc \theta_0 \left[1 - \cos^2 \theta_0 \left(1 + \varepsilon_t^* \right)^2 \right]^{1/2} \quad (2.4)$$

Attaining full densification also requires that the inclined struts do not buckle or yield. The critical strut buckling force is $\Phi_c^{buc} \equiv F_c^{buc} / E_t t_t$ where $F_c^{buc} = \pi^2 E_c t_c^3 / 12 K^2 L_c^2$ (the Euler buckling force), E_c is the Young's modulus of the inclined strut, t_c and L_c are strut thickness and length, respectively, and K is the effective length parameter. Combining these results yields a buckling force of $\Phi_c^{buc} = \Gamma$ where Γ is a non-dimensional buckling parameter defined by $\Gamma \equiv \pi^2 E_c t_c^3 / 12 E_t t_t L_c^2 K^2$. Buckling is avoided when $\Phi_c^{\max} < \Phi_c^{buc}$ or, equivalently, $\theta_0 < \theta_0^{buc} = \sec^{-1}(2\Gamma + 1)$. When $\theta_0 > \theta_0^{buc}$, buckling occurs at an applied strain of

$$\varepsilon_a^{buc} = 1 - \csc \theta_0 \left[1 - (\sec \theta_0 - 2\Gamma)^{-2} \right]^{1/2} \quad (2.5)$$

Analogously, the critical strut yielding force is $\Phi_c^{yield} \equiv F_c^{yield} / E_t t_t$ where $F_c^{yield} = \sigma_y t_c$ and σ_y is the yield stress of the compressive strut material. Again, combining these results produces a yielding force of $\Phi_c^{yield} = \Lambda$ where Λ is a non-dimensional yielding parameter defined by $\Lambda \equiv \sigma_y t_c / E_t t_t$. Yielding is avoided when $\Phi_c^{\max} < \Phi_c^{yield}$ or when $\theta_0 < \theta_0^{yield} = \sec^{-1}(2\Lambda + 1)$. When $\theta_0 > \theta_0^{yield}$, yielding occurs at an applied strain of

$$\varepsilon_a^{yield} = 1 - \csc \theta_0 \left[1 - (\sec \theta_0 - 2\Lambda)^{-2} \right]^{1/2} \quad (2.6)$$

To demonstrate the trade-offs between structural properties, lattice geometry and constituent materials, the predicted force-displacement curves in Fig. 2.3a are augmented by a set of failure loci corresponding to tensile strut rupture (Eq. 2.4) and to inclined strut buckling (Eq. 2.5) and yielding (Eq. 2.6). The trade-offs that emerge highlight the need for concurrent selection of geometry and constituent materials for optimal lattice design.

2.2.2 Bi-material Lattice Based on the Primitive Motif

A conceptual design of a 2D multi-cell lattice based on the primitive motif is illustrated in Fig. 2.4a. With the expectation of large geometric changes accompanying macroscopic axial compression and thus the need for strut rotation, the nodes are designed (nominally) as ball-and-socket joints. The balls are located at the ends of the inclined struts and the sockets are created within a circular common hub. A thin (ca. 250 μm) layer of the elastomeric material used for the transverse struts is placed between the surfaces of the balls and sockets. The same material envelops the hub and seamlessly transitions into the transverse struts to reduce stress concentrations^{31,32}. Flat spots on the hubs located at the external surfaces facilitate loading.

A series of test specimens with the design in Fig. 2.4(a) were fabricated via multi-material 3D printing (Objet500 Connex3, Stratasys). Print fidelity is evidenced by comparisons of the CAD drawings with photographs of the printed lattices (Fig. 2.4a and Fig. 2.5). In all cases, the inclined struts are made from a stiff acrylic-like material (VeroWhite). The tensile struts are made from one of four elastomers, designated Agilus 30A, 50A, 85A, and 95A by the manufacturer. (The numbers denote the nominal Shore A hardness.) The relative density of the lattice, calculated as the projected area of solids within a rectangular area defined by the centers of the four outermost nodes, is 0.40. The properties of the constituent materials were obtained from tensile tests on dog-bone specimens that had been printed in an identical manner. These properties are summarized in Fig. 2.6. To establish baseline lattice properties, single-material lattices with the same design were also printed and tested (Figs. 2.5c and 2.5d). The latter lattices were made of VeroWhite, Agilus 50A and Agilus 85A.

2.3 Compressive Response

2.3.1 Methods

Lattices were tested in uniaxial compression using Teflon platens to reduce friction. Full-field displacement measurements of the entire lattice were made on the “front” surface using 2D digital image correlation (DIC). A more detailed displacement map of the center-most node alone was obtained on the opposing (“back”) face of the lattice. The tests included occasional unload-reload cycles to probe hysteresis intrinsic to the transverse struts and hysteresis due to friction between the external nodes and the loading platens.

In preparation for testing, random speckles with a diameter of approximately 200 μm were applied to the front face using aerosol paint. On the back face (where higher magnification displacement mapping of a single node would occur), speckles with a mean diameter of 50 μm were applied using an airbrush. Images were taken using two digital cameras (Point Grey Research Grasshopper), each with a CCD resolution of 2448x2048 pixels, at magnifications of 14 and 90 pixels/mm on the front and back face, respectively. With this magnification, the area of the entire sample (1750 x 775 pixels) and the node (1900 x 1900) could be monitored during testing while maintaining a minimum of 3 pixels/speckle in subsequent analyses, as recommended for accurate correlation³³. The data were analyzed using incremental correlation with a subset size and step size of, respectively, 15 pixels and 3 pixels on the front face, and 25 pixels and 3 pixels on the back face. The macroscopic compressive strain was obtained from the DIC data using five virtual extensometers spanning the node centers on opposing faces. The stress was computed from the measured force and the projected area of the test samples between the centers of the outer nodes on the loading platens.

Three local deformation metrics were computed from the DIC data: (i) von Mises equivalent strains, ε_{eq} , and (ii) axial strains in transverse struts ε_t within each strut as well as (iii) rotations ω . Von Mises equivalent strains were found through ε_x , ε_y , and γ_{xy} strain components. Axial strains in transverse struts, ε_t , were found from virtual extensometers on individual struts, neglecting portions residing within the node regions. Finally, rotations were calculated for each inclined strut at two locations: one at the center of the ball at the end of the inclined strut and one along the strut centerline 6 mm away.

Corresponding finite element analyses (FEA) were performed using Abaqus/Standard (Version 2018, Dassault Systèmes, Providence, RI). In the model, each strut was discretized using 20 Timoshenko beam elements with rectangular cross-section and with dimensions matching those of the test specimens. Each hub was modeled using 6 beam elements connected to form a rigid hexagon, as shown schematically in Figs. 2.4b–d. Inclined struts were assumed to be linear-elastic with a Young's modulus obtained from the uniaxial tensile tests on the same material (e.g. $E_0 = 1.35$ GPa for the VeroWhite). The tensile response of the transverse struts was assumed to be linear with Young's moduli obtained from the tensile tests. Loading platens were modeled using two-node, rigid-beam elements (RB2D2).

The influence of friction was studied by assigning contact properties to the surfaces of discretely rigid platens and the external surfaces of top and bottom hexagonal hubs. The surface-based contact simulations probed two cases: one with a friction coefficient $\mu = 0$ and another with $\mu = 0.12$. The latter value had been obtained by placing the lattice on a Teflon platen, placing a known mass on top of it, and measuring the lateral force needed for sliding using a force spring scale. In both contact scenarios, joints between lattice struts and the hexagonal hubs were modeled as pinned. Additionally, to maintain contact normals between

external nodes and platens, the hexagonal hubs were constrained against rotation. Rigid body motion of the lattice was prevented by fixing translational degrees of freedom of the center node at the bottom platen. The other nodes on this platen were constrained from displacement in the loading (y) direction, i.e., $v=0$. Uniaxial cyclic compression was simulated by prescribing displacement to the top platen that varied as a function of time to match the loading cycles in the experiments.

2.3.2 Measurements and Analysis of Single-Material Lattices

The elastic modulus of all single-material lattices is about $E/E_s = 0.13$ where E_s is the modulus of the parent material (Fig. 2.7). By comparison, a mechanics analysis of this lattice (with $\theta_0 = 60^\circ$ and thus $L_c = L_t \equiv L$) yields a modulus of

$$\frac{E}{E_s} = \frac{3\sqrt{3}t_c}{4L(1+t_c/11t_t)} \quad (2.7)$$

(Derivations of moduli for this and other cases are presented in Appendix 2.A2.) Taking $t_c = 2$ mm, $t_t = 4$ mm and $L = 27$ mm (the distance between node centers as defined in Figure 2.4a), the predicted modulus is $E/E_s = 0.092$. The discrepancies between predicted and measured moduli are attributable to the finite node size (radius $R_h = 3.5$ mm) and corresponding differences in strut lengths. Taking the *effective* strut length to be $L^{eff} = L - 2R_h = 20$ mm (as illustrated in Figure 2.4b) and assuming the nodes to be rigid, the modulus becomes $E/E_s = 0.12$, essentially the same as the measured values.

Lattices of the elastomeric materials 50A and 85A exhibit peak stresses of 0.005 MPa and 0.017 MPa, respectively. The peaks are obtained at the end of the linear domain, at a

nominal strain of $\varepsilon_a \approx 0.05$. Strain maps in Figs. 2.7a and 2.7b show that the strut buckling begins at the stress peaks. For comparison, the predicted applied stress for elastic buckling is given by

$$\sigma_a^{buc} = \frac{11\pi^2 E t_c^3 \sin \theta_0}{72L(KL^*)^2} \quad (2.8)$$

where, for fixed joints (assumed to be the case here), $K = 0.5$, and L^* is the pertinent compressive strut length. Two values of L^* are considered: (i) the effective length, $L_c^{eff} = 20\text{mm}$, which excludes the central hubs but includes the adjoining fillet region, and (ii) the length over which the strut thickness is uniform, which excludes both the hubs and the fillet ($L^* = 11\text{ mm}$). Using these estimates, the predicted buckling stress for the 50A lattice falls in the range 0.0035–0.012 MPa while that for the 85A lattice falls in the range of 0.010–0.034 MPa. Although somewhat broad, these ranges encompass the measured peak stresses.

Beyond the stress peaks, the elastomeric lattices exhibit slight softening and attainment of a plateau, followed by rapid hardening once internal self-contact is made (at a strain of about 0.3). The unloading-reloading loops show significant hysteresis but with the strain returning to nearly zero upon complete unloading. The transverse lattice strains remain negligibly small throughout.

The failure mode of the acrylic lattice is somewhat ill-defined. The peak compressive stress is 4.1 MPa, obtained at a strain of 0.04. The predicted elastic buckling stress, computed using the parameter values presented above, falls in the range 5.2–17 MPa, somewhat above the measured value. Additionally, the predicted stress for strut *yielding* ($\sigma_a = 11t\sigma_y \sin \theta_0 / L$, with σ_y being the material yield strength) is about 5.3 MPa: close to the lower end of the

predicted buckling stress range but still somewhat above the measured peak (by about 30%). In light of the similarities in the predicted buckling and yield stresses, and recognizing that in the transitional domain between elastic buckling and yielding the failure stress is lower than that for either mode alone, we surmise that failure here involves nearly-concurrent yielding and buckling. Beyond the peak, the lattice exhibits rapid softening as the inclined struts undergo plastic collapse (Fig 2.7c). Here again the transverse lattice strain remains negligible throughout.

2.3.3 Experimental Measurements on Bi-Material Lattices

The compressive responses of the bi-material lattices differ significantly from those of the single-material lattices and depend sensitively on the specific elastomer used for the transverse struts. The VeroWhite/50A typifies lattices with the softer elastomers (Fig. 2.8a). Here the forward loading curves exhibit characteristics that are qualitatively similar to those predicted for the primitive structural motif. Notably, the stress rises non-linearly, reaches a peak at a strain of about 0.2 (comparable to that for the primitive motif with the same inclination angle, 60°), and decreases gradually with further straining. But unlike the primitive motif, the experimental lattice attains a strain of only about 0.47. At this strain, transverse struts begin to rupture. The accompanying strain maps show that the macroscopic compressive strain is accommodated by extension of the transverse struts and rotation of the inclined struts up to strains of about 0.25 and by bending of the inclined struts at larger strains. These mechanisms give rise to large transverse strains in the lattice. The response of the lattice with the stiffer elastomer begins similarly, with higher stiffness, but terminates at a lower strain because of rupture of the transverse struts (Fig. 2.8b). This is qualitatively consistent with the trade-offs between strength and ductility in this series of elastomers, shown in Fig. 2.6.

Rotations of material elements near the central node yield insights into the efficacy of the ball-and-socket node design in facilitating rotation of the inclined struts. Both full-field rotations and a plot of the variation in rotation with applied strain at the two lattice locations of interest (at the ball center and at a point 6 mm away) are shown in Fig. 2.9. Predicted rotations based on a geometric model that assumes pinned joints are included for comparison. Although the rotations at short distances from the ball centers match the predicted values well, the rotations *at* the ball centers are considerably lower. The latter rotations are about 50%, 25% and 20% of the predicted values for the lattices with 30A, 50A and 85A elastomers, respectively. The differences in rotations at the ball centers are attributable to the stiffnesses of the constituent elastomers. That is, the lattice with the most compliant elastomer (30A) requires the lowest force to effect deformation and hence exhibits the greatest rotations among the three elastomers. Clearly, the rotation at the ball center is over-constrained by the surrounding elastomer.

Unloading-reloading excursions of the bi-material lattices are accompanied by hysteresis, due in part to viscoelasticity of the elastomeric materials and in part to friction at the points of contact of the external nodes with the loading platens. One clear manifestation of friction is in the load drops obtained upon unloading; these are not accompanied by a change in axial strain and cannot be attributed to viscoelasticity.

Further insights into friction effects emerge from the transverse node displacements during loading and unloading; two illustrative examples are shown in Figs. 2.10a and 2.10b. Upon loading, all surface nodes not located at the lattice center begin to slide laterally shortly after loading begins. Upon initial *unloading*, these nodes remain stationary; they begin to slide in the opposite direction only once the load decrement reaches a critical value. Treating these

nodes as Coulombic friction blocks with a critical transverse force F_l for forward sliding, it follows that the lateral force must drop by $2F_l$ in order for reverse sliding to begin. Further assuming that the lateral forces are proportional to the applied force, the unloading decrement needed for reverse sliding would be twice that for forward sliding. These effects are borne out by the model predictions presented in the subsequent section.

Friction does not appear to affect the tensile strains within the transverse struts. These strains are remarkably uniform across all struts, both internal to the lattice and adjacent to the loading platens, during both loading and unloading (Fig. 2.11). For the lattice with the 85A elastomer, the strains are consistent with the predicted strains from Eq. 2.2 (neglecting finite node size). For the lattices with the two softer elastomers, the strains are about 10–20% greater. These differences are reconciled by modifying the model to account for finite node size, as described below.

2.3.4 Analytical model of bi-material lattice response

The mechanics analysis of the primitive structural motif was extended to the multi-cell lattice in two ways. (To recapitulate, all analyses are based on the assumptions that inclined struts are much stiffer than transverse struts, nodes are pin-jointed, and transverse struts are elastomeric with linear stress-strain response).

The first extension accounts for the finite number of cells and associated edge effects. The results are presented in terms of a normalized applied *stress* per unit depth, $\Sigma_a \equiv \sigma_a L_t / 3E_t t_t$. (Note that Σ_a for the lattice is closely analogous to Φ_a for the primitive motif, differing mainly by the factor 3; this factor arises from the presence of 3 layers of transverse struts in the lattice and only a single layer in the primitive motif.) The predicted

nodal forces were obtained using the method of joints and confirmed via FEA; the results are summarized in the Appendix (Fig. 2.A1c). The resulting lattice stress-strain response is given by:

$$\Sigma_a = \left(\frac{11}{12}\right)(1 - \varepsilon_a) \left[\tan \theta_0 - \left(\csc^2 \theta_0 - (1 - \varepsilon_a)^2 \right)^{-1/2} \right] \quad (2.9)$$

This result differs from the one in Eq. 2.1 by the numerical coefficient 11/12. If the structure were infinite in width and could therefore be represented by a single unit cell, without edge effects, the numerical coefficient in Eq. 2.9 would be simply 1. The present test samples each comprise 4 unit cells but lack the central transverse struts that would otherwise be attached to neighboring cells in an infinite array. The effect of these “missing” transverse struts is a reduction in stress by a factor of 11/12, *i.e.* the fraction of possible transverse struts present in the finite lattice. The tensile strain in the transverse struts is still given by Eq. 2.2.

The second extension accounts for *finite node size*. The node size affects the length of inclined struts and their rotation, the effective length of transverse struts, and the densification strain (Fig. 2.4b-d). Here the hub of each node is assumed to be rigid with each inclined strut now pivoting about a point a distance equal to the hub radius R_h from the hub center. The normalized effective length of inclined struts is therefore $\alpha_c \equiv L_c^{eff} / L_c \approx 1 - 2R_h / L_c$. Additionally, each transverse strut begins at a point R_h from the hub center and thus its normalized effective length is $\alpha_t \equiv L_t^{eff} / L_t \approx 1 - 2R_h / L_t$. From geometry the ratio of effective lengths is $L_c^{eff} / L_t^{eff} = \alpha_c / 2\alpha_t \cos \theta_0$. The inclination angle θ and transverse strut strain ε_t are modified to read:

$$\theta = \sin^{-1} \left[\sin \theta_0 (1 - \varepsilon_a / \alpha_c) \right] \quad (2.10)$$

and

$$\varepsilon_t = \frac{\alpha_c}{\alpha_t} \left[\tan \theta_0 \left(\csc^2 \theta_0 - (1 - \varepsilon_a / \alpha_c)^2 \right)^{1/2} - 1 \right] \quad (2.11)$$

Combining these modifications, the lattice stress-strain response becomes:

$$S_a = \left(\frac{11a_c}{12a_t} \right) \left(1 - e_a / a_c \right) \left[\tan q_0 - \left(\csc^2 q_0 - \left(1 - e_a / a_c \right)^2 \right)^{-1/2} \right] \quad (2.12)$$

The normalized compressive stresses in inclined struts, defined as $\Sigma_c \equiv F_c / 3E_t t_t$, are:

$$\Sigma_c = \frac{\alpha_c}{2\alpha_t} \left[\sec \theta_o - \left(1 - \sin^2 \theta_o (1 - \varepsilon_a / \alpha_c)^2 \right)^{-1/2} \right] \quad (2.13)$$

in the inner struts (i.e. those fully contained within the lattice), and

$$\Sigma_c = \frac{\alpha_c}{3\alpha_t} \left[\sec \theta_o - \left(1 - \sin^2 \theta_o (1 - \varepsilon_a / \alpha_c)^2 \right)^{-1/2} \right] \quad (2.14)$$

in the outer struts. Neglecting constraints on node rotation, densification is assumed to occur when the initially inclined struts are horizontal, as illustrated in Fig. 2.4d. The densification strain is therefore $\varepsilon_a^{den} = \alpha_c$.

The maximum values of ε_t and Σ_c are obtained at $e_a = e_a^{den} = a_c$ and are given by

$$\varepsilon_t^{\max} = \frac{\alpha_c (\sec \theta_0 - 1)}{\alpha_t} \quad (2.15)$$

$$\Sigma_c^{\max} = \frac{\alpha_c (\sec \theta_0 - 1)}{2\alpha_t} \quad (2.16)$$

Tensile rupture is therefore avoided when the initial inclination is below a critical value of $\theta_0^* = \sec^{-1}(1 + \varepsilon_t^* \alpha_t / \alpha_c)$ (from Eq. 2.15). Otherwise, tensile rupture occurs at an applied strain of

$$\varepsilon_a^* = \alpha_c \left\{ 1 - \csc \theta_0 \left(1 - \cos^2 \theta_0 \left(1 + \alpha_t \varepsilon_t^* / \alpha_c \right)^2 \right)^{1/2} \right\} \quad (2.17)$$

Similarly, buckling is avoided when the maximum stress in the inclined struts is less than the buckling stress, $\Sigma_c^{\max} < \Sigma_c^{buc} = F_a^{buc} / 3E_t t_t = \Gamma / \alpha_c^2$, or, equivalently, $\theta_0 < \theta_0^{buc} \equiv \sec^{-1}(1 + 2\Gamma \alpha_t / \alpha_c^3)$ (from Eq. 2.16). Otherwise buckling occurs at a strain of

$$\varepsilon_a^{buc} = \alpha_c \left\{ 1 - \csc \theta_0 \left[1 - \left(\sec \theta_0 - 2\Gamma \alpha_t / \alpha_c^3 \right)^{-2} \right]^{1/2} \right\} \quad (2.18)$$

Lastly, yielding is avoided when the maximum stress in the inclined struts is less than the yielding stress, $\Sigma_c^{\max} < \Sigma_c^{yield} = F_a^{yield} / 3E_t t_t = \Lambda$, or, equivalently, $\theta_0 < \theta_0^{yield} \equiv \sec^{-1}(1 + 2\Lambda \alpha_t / \alpha_c)$. Otherwise yielding occurs at a strain of

$$\varepsilon_a^{yield} = \alpha_c \left\{ 1 - \csc \theta_0 \left[1 - \left(\sec \theta_0 - 2\Lambda \alpha_t / \alpha_c \right)^{-2} \right]^{1/2} \right\} \quad (2.19)$$

To highlight the effects of these modifications, the predicted stress-strain curves and failure loci for finite lattices (Fig. 2.12) are compared with those for the primitive motif (Fig. 2.3). The geometric parameters selected for these comparisons are representative of the present experimental lattices, with the inclination angle θ_0 being the one design variable. Here the lattice height, the effective inclined strut length ($\alpha_c = 0.75$), and the densification strain ($\varepsilon_a^{den} = \alpha_c = 0.75$) are held constant while the effective transverse strut length, α_t , is varied with θ_0 in order to maintain a fixed node size. To achieve full densification, lattices with finite nodes require the transverse strut material to have a higher ductility, because higher tensile strains are obtained in the shortened transverse struts at a given applied lattice strain.

The shortened transverse strut has two other effects. First, it increases the applied stress required to deform the lattice to a prescribed strain. Second, it increases the compressive stresses in inclined struts and therefore *increases* the minimum value of the yielding parameter Λ needed to attain densification without yielding (compare Figs. 2.3b and 2.12b). Additionally, despite the increased stress in the inclined struts, the required value of the buckling parameter Γ needed to reach densification without buckling *decreases*, a consequence of the reduction in the effective compressive strut length and hence an improvement in its buckling resistance (buckling strength being proportional to $1/\alpha_c^2$).

2.4 Assessment of Analytical Models and FEA

The analytical models and FEA results are assessed by comparing them with the various experimental measurements. The focus is on: (i) the stress-strain response in the initial stages of forward loading, (ii) the response at moderate strains, where significant geometric changes

occur, (iii) hysteresis upon loading/unloading, (iv) node displacements, and (v) failure initiation.

The FEA results capture essentially all of the key features observed experimentally to varying degrees of accuracy. The predicted stress-strain curves up to strains of about 0.05 track reasonably well with the measured curves, albeit with somewhat softer response (by about 20-40%). The anomalously soft response can be attributed to the assumption in the model that the nodes are pinned whereas the real ones have finite stiffnesses. Select FEA simulations of cases in which the nodes were assumed to be rigid yielded a stiffness for the VeroWhite/85A lattice that was 30% higher than the experimentally measured value while the result from the pin-jointed simulation was 40% lower. These results bound the experimental values well. Additional simulations for the VeroWhite/50A lattice yielded stiffnesses that were higher than the experimentally measured value by a factor of 2.5. Evidently the disparity between the rigid-node simulations and the experimental measurements increases as the stiffness of the transverse strut material decreases.

One of the features found experimentally but not captured by FEA is progressive softening of the forward loading response following cyclic unloading-reloading, a consequence of the viscoelastic character of the elastomers (evident in the tensile test results in Fig. 2.6) and possibly damage to the material. Clearly this discrepancy is due to the assumption that the elastomer response in the FEA is linear-elastic. The predicted load drops during initial unloading and before the onset of reverse sliding of surface nodes are similar to those measured experimentally. Upon further unloading, the predicted stress-strain curves converge to the origin more rapidly, again a consequence of the hysteretic response of the elastomers. The nodal displacements from FEA match the experimental measurements well,

overestimating the magnitudes of the displacements by only about 10-20% (Figs. 2.10c and 10d). Here again the discrepancy is attributable to the assumption regarding pinned joints in the model. Finally, predictions of failure, based on the attainment of a critical tensile strain in the transverse struts (namely the measured tensile failure strain) without consideration for cyclic effects, are only roughly in line with the measurements.

The analytical prediction of the stress-strain response (neglecting friction) falls midway between the loading and unloading curves obtained experimentally and from FEA. Indeed, FEA simulations without friction (not shown) recover a result nearly identical to the analytical result. The slight deviation is due to the finite ratio between inclined and transverse strut material stiffnesses, E_c / E_t . The analytical model assumes a stiffness ratio of $E_c / E_t = \infty$ while the FE model uses experimentally measured stiffness ratios of $E_c / E_t \approx 1500$ and $E_c / E_t \approx 500$ for the VeroWhite/50A and VeroWhite/85A lattices respectively. Having no inelasticity in the analytical model, the loading and unloading curves are identical. Additionally, the model predictions for node displacement (Figs. 2.10c and d) and for failure initiation (Fig. 2.8) are nearly identical to those from FEA.

2.5 Summary and Conclusions

The present study provides a quantitative framework for preliminary design of a family of structural bi-material lattices with potential for both high strength and high straining capability, incorporating both geometry and material properties. The mechanics analysis of the primitive structural motif yields a particularly useful baseline both for estimating the overall stress-strain response and for predicting failure initiation. Extensions of the analysis to lattices with multiple layers, boundaries, and finite nodes readily capture secondary (though not insignificant) effects

associated with implementation of the concept into a structural design. Even in their current form, the models could be used to begin optimization of the geometry to attain targeted properties. One as-yet unexplored aspect of the response of *large* bi-material structures of this type, with many unit cells in both directions, is the possibility of long-range deformation instabilities. The extent to which these might be controlled or even exploited remains to be studied.

The specific lattice design examined experimentally has two shortcomings. The first is the need for large lateral displacements (with associated friction) to accommodate axial displacements. Variants on the design that enable the lateral displacements to occur entirely within the body of the lattice *without global transverse displacement* can be readily envisioned. Second, the node design yields excessive constraint on strut rotation at large displacements, especially with the stiffest elastomers. These effects could be mitigated through re-design of the size and shape of the ball-and-socket connection as well as selection of alternative elastomers for the intervening gaps. Remediation strategies of this type are the focus of current activities.

Finally, the present structural concept remains to be critically assessed against existing single-material concepts. This would require comparisons of the properties that can be attained using real structural constituent materials in the bi-material lattices and the properties that can be attained with single-material lattices. The growing spectrum of materials being developed for additive manufacturing and the expanding capabilities for printing multiple materials will facilitate these efforts.

2.A Appendix

2.A1 Response of Primitive Structural Motif

The following analysis of the structural response of the primitive motif is based on an energy method. When the structure is compressed, the work U_w done by the applied force F_a is equal to the elastic strain energy U_e in the transverse strut. The work done is $U_w = \int_0^v F_a(v')dv'$ where v is the axial displacement and the prime denotes a dummy variable. The height of the structure is reduced from H_0 to $H = H_0 - v$. The displacement v is accommodated by rotation of the inclined struts from an initial angle θ_0 to θ and elongation of the transverse strut from a length W_0 to $W = W_0 + u$. The strain energy in the transverse strut is

$$U_e = \int_0^u F_t(u')du' = \int_0^u \frac{E_t t_t u' \tan \theta}{H_0} du' \quad (2.A1)$$

where F_t is the force in the transverse strut. Setting $U_e = U_w$, the force-displacement relation

$F_a(v)$ is found to be

$$F_a(v) = \frac{E_t t_t \tan \theta u(v)}{H_0} \frac{du(v)}{dv} \quad (2.A2)$$

From geometry,

$$u(v)/H_0 = \left(\csc^2 \theta_0 - (1 - \varepsilon_a)^2 \right)^{1/2} - \cot \theta_0 \quad (2.A3)$$

$$du(v)/dv = (1 - \varepsilon_a) \left(\csc^2 \theta_0 - (1 - \varepsilon_a)^2 \right)^{-1/2} \quad (2.A4)$$

and $\theta = \sin^{-1} \left[\sin \theta_0 (1 - \varepsilon_a) \right]$. Combining the preceding equations yields Eq. 2.1 in the text.

2.A2 Young's Moduli of Bi-material Triangulated Lattices

Infinite triangular lattice

The Young's modulus of an *infinite* bi-material triangular lattice is obtained from analysis of the representative volume element shown in Fig. 2.A1a. From consideration of mechanical equilibrium of the top node, the force per unit depth of in each inclined (compressive) strut is

$$F_c = F_n \csc \theta_0 / 2 \quad \text{where } F_n \text{ is the axial force on the node, given by } F_n = \sigma_a L_t. \quad \text{The}$$

corresponding stress and strain are

$$\sigma_c = F_c / t_c = \sigma_a L_t \csc \theta_0 / 2 t_c \quad (2.A5)$$

$$\varepsilon_c = \sigma_a L_t \csc \theta_0 / 2 t_c E_c. \quad (2.A6)$$

Similarly, from consideration of equilibrium of the bottom two nodes, the force in the transverse strut is $F_t = \sigma_a L_t \cot \theta_0 / 2$ and thus the stress and strain are

$$\sigma_t = F_t / t_t = \sigma_a L_t \cot \theta_0 / 2 t_t \quad (2.A7)$$

$$\varepsilon_t = \sigma_a L_t \cot \theta_0 / 2 t_t E_t. \quad (2.A8)$$

The macroscopic lattice strain, in turn, is

$$\varepsilon_a = 1 - H / H_0 = 1 - (H / L_{c,0}) (L_{c,0} / H_0) \quad (2.A9)$$

where $L_{c,0}$ is the initial length of the compressive strut and, from geometry, $L_{c,0} / H_0 = \csc \theta_0$,

$L_c / L_{c,0} = 1 - \varepsilon_c$, $L_t / L_{t,0} = 1 + \varepsilon_t$, and $L_{t,0} / 2L_{c,0} = \cos \theta_0$, with $L_{t,0}$ being the initial length of the

transverse strut, and with

$$H / L_{c,0} = \sqrt{(L_c / L_{c,0})^2 - (L_t / 2L_{c,0})^2} = \sqrt{(L_c / L_{c,0})^2 - (L_t / L_{t,0})^2 (L_{t,0} / 2L_{c,0})^2} \quad (2.A10)$$

Combining and making a small strain approximation yields an axial Young's modulus E of

$$\frac{E}{E_c} = \frac{2t_c \sin^3 \theta_0}{L_t (1 + t_c E_c \cos^3 \theta_0 / t_t E_t)} \quad (2.A11)$$

When $\theta_0 = 60^\circ$, $t_c = t_t = t$,

and the two materials are the same ($E_t = E_c \equiv E_s$), Eq. 2.A11 reduces to $E/E_s = 2t/\sqrt{3}L \approx 1.15t/L$ where $L = L_t = L_c$. The latter result is the same as that reported previously for this lattice geometry (Gibson and Ashby, 1997; Hunt, 1993).

Semi-infinite two-layer triangular lattice

Analysis of the *semi-infinite* two-layer bi-material lattice in Fig. 2.A1b proceeds in a similar manner. It differs from the preceding case only in that there are 3 transverse struts for a lattice with 2 layers (not one per layer as in the infinite lattice). The stress in each transverse strut ($\sigma_t = \sigma_a L_t \cot \theta_0 / 3t_t$) is 2/3 that in the infinite lattice while the stress in each inclined strut is the same as that in the infinite lattice (Eq. 2.A5). The resulting modulus is:

$$\frac{E}{E_c} = \frac{2t_c \sin^3 \theta_0}{L_t (1 + 2t_c E_c \cos^3 \theta_0 / 3t_t E_t)} \quad (2.A12)$$

Finite two-layer triangular lattice

For the *finite* lattice studied here (Fig. 2.A1c), the force acting on each of the 3 surface nodes in the central region of the lattice is $F_n = 3F_a/11 = 12\sigma_a L_t/11$ (higher by a factor of 12/11 relative to that in the infinite lattice) while the force on each of the outer surface nodes is $F_n = F_a/11 = 4\sigma_a L_t/11$. The stress in each inclined strut in the central region of the lattice is

$$\sigma_c = 3F_a \csc \theta_0 / 22t_c = 6\sigma_a L_t \csc \theta_0 / 11t_c \quad (2.A13)$$

while that in each inclined strut connected to the 4 outer surface nodes is

$$\sigma_c = F_a \csc \theta_0 / 11t_c = 4\sigma_a L_t \csc \theta_0 / 11t_c . \quad (2.A14)$$

The tensile stress in each transverse strut is

$$\sigma_t = F_a \cot \theta_0 / 11t_t = 4\sigma_a L_t \cot \theta_0 / 11t_t . \quad (2.A15)$$

The resulting lattice modulus is

$$\frac{E}{E_c} = \frac{2t_c \sin^3 \theta_0}{L_t (1 + 8t_c E_c \cos^3 \theta_0 / 11t_t E_t)} \quad (2.A16)$$

This result differs from that of the semi-infinite two-layer lattice (Eq. 2.A12) by a factor of $(11/12) \left[1 + 1 / \left(11 + 8t_c E_c \cos^3 \theta_0 / t_t E_t \right) \right]$.

For the parameter values used in the present experimental study, the modulus of the semi-infinite two-layer single-material lattice (with $E_t = E_c$) is predicted to be within about 0.4% of the value for the finite two-layer single-material lattice. Boundary effects are minimal in this case.

References

1. Zok, F. W. Integrating lattice materials science into the traditional processing-structure-properties paradigm. *MRS Commun.* 9, 1284–1291 (2019).
2. Deshpande, V. S., Ashby, M. F. & Fleck, N. A. Foam topology: Bending versus stretching dominated architectures. *Acta Mater.* 49, 1035–1040 (2001).
3. Ashby, M. . The properties of foams and lattices. *Philos. Trans. R. Soc. A Math. Phys. Eng. Sci.* 364, 15–30 (2005).
4. Gibson, L. J. & Ashby, M. F. *Cellular solids: structure and properties.* (Cambridge University Press, 1997).
5. Begley, M. R. & Zok, F. W. Optimal material properties for mitigating brain injury during head impact. *J. Appl. Mech. Trans. ASME* 81, (2014).
6. Hammetter, C. I., Rinaldi, R. G. & Zok, F. W. Pyramidal Lattice Structures for High Strength and Energy Absorption. *J. Appl. Mech.* 80, (2013).
7. Bernal Ostos, J. *et al.* Deformation stabilization of lattice structures via foam addition. *Acta Mater.* (2012). doi:10.1016/j.actamat.2012.07.053
8. Lakes, R. S., Lee, T., Bersie, A. & Wang, Y. C. Extreme damping in composite materials with negative-stiffness inclusions. *Nature* 410, 565–567 (2001).
9. Kochmann, D. M. & Bertoldi, K. Exploiting Microstructural Instabilities in Solids and Structures: From Metamaterials to Structural Transitions. *Applied Mechanics Reviews* 69, (2017).

10. Che, K., Yuan, C., Wu, J., Qi, H. J. & Meaud, J. Three-dimensional-printed multistable mechanical metamaterials with a deterministic deformation sequence. *J. Appl. Mech. Trans. ASME* 84, (2017).
11. Mullin, T., Deschanel, S., Bertoldi, K. & Boyce, M. C. Pattern transformation triggered by deformation. *Phys. Rev. Lett.* 99, 084301 (2007).
12. Shan, S. *et al.* Multistable Architected Materials for Trapping Elastic Strain Energy. *Adv. Mater.* 27, 4296–4301 (2015).
13. Wehmeyer, S. *et al.* Post-buckling and dynamic response of angled struts in elastic lattices. *J. Mech. Phys. Solids* 133, 103693 (2019).
14. Raney, J. R. *et al.* Stable propagation of mechanical signals in soft media using stored elastic energy. *Proc. Natl. Acad. Sci. U. S. A.* 113, 9722–9727 (2016).
15. Debeau, D. A., Seepersad, C. C. & Haberman, M. R. Impact behavior of negative stiffness honeycomb materials. *J. Mater. Res.* 33, 290–299 (2018).
16. Morris, C., Bekker, L., Spadaccini, C., Haberman, M. & Seepersad, C. Tunable Mechanical Metamaterial with Constrained Negative Stiffness for Improved Quasi-Static and Dynamic Energy Dissipation. *Adv. Eng. Mater.* 21, 1900163 (2019).
17. Meaud, J. & Che, K. Tuning elastic wave propagation in multistable architected materials. *Int. J. Solids Struct.* 122–123, 69–80 (2017).
18. Chen, Q., Zhang, X. & Zhu, B. Design of buckling-induced mechanical metamaterials for energy absorption using topology optimization. *Struct. Multidiscip. Optim.* 58, 1395–1410 (2018).

19. Correa, D. M. *et al.* Negative stiffness honeycombs for recoverable shock isolation. *Rapid Prototyp. J.* 21, 193–200 (2015).
20. Findeisen, C., Hohe, J., Kadic, M. & Gumbsch, P. Characteristics of mechanical metamaterials based on buckling elements. *J. Mech. Phys. Solids* 102, 151–164 (2017).
21. Florijn, B., Coulais, C. & Van Hecke, M. Programmable mechanical metamaterials. *Phys. Rev. Lett.* 113, 175503 (2014).
22. Frenzel, T., Findeisen, C., Kadic, M., Gumbsch, P. & Wegener, M. Tailored Buckling Microlattices as Reusable Light-Weight Shock Absorbers. *Adv. Mater.* (2016).
doi:10.1002/adma.201600610
23. Hu, N. & Burgueño, R. Buckling-induced smart applications: recent advances and trends. *SMAJ* 24, 063001 (2015).
24. Haghpanah, B., Shirazi, A., Salari-Sharif, L., Guell Izard, A. & Valdevit, L. Elastic architected materials with extreme damping capacity. *Extrem. Mech. Lett.* 17, 56–61 (2017).
25. Ha, C. S., Lakes, R. S. & Plesha, M. E. Design, fabrication, and analysis of lattice exhibiting energy absorption via snap-through behavior. *Mater. Des.* 141, 426–437 (2018).
26. Evans, A. G., Hutchinson, J. W., Fleck, N. A., Ashby, M. F. & Wadley, H. N. G. The topological design of multifunctional cellular metals. *Prog. Mater. Sci.* (2001).
doi:10.1016/S0079-6425(00)00016-5

27. Latture, R. M., Begley, M. R. & Zok, F. W. Defect Sensitivity of Truss Strength. *J. Mech. Phys. Solids* 124, 489–504 (2019).
28. Latture, R. M., Begley, M. R. & Zok, F. W. Design and mechanical properties of elastically isotropic trusses. *J. Mater. Res.* (2018). doi:10.1557/jmr.2018.2
29. R.E. Skelton, M.C. Oliveira. *Tensegrity Systems*. (Springer, 2009).
30. Lee, J., Kim, H. C., Choi, J. W. & Lee, I. H. A review on 3D printed smart devices for 4D printing. *International Journal of Precision Engineering and Manufacturing - Green Technology* 4, 373–383 (2017).
31. Pilkey, W. D. & Pilkey, D. F. Peterson's Stress Concentration Factors. *John Wiley & Sons* (2008).
32. Latture, R. M., Rodriguez, R. X., Holmes, L. R. & Zok, F. W. Effects of Nodal Fillets and External Boundaries on Compressive Response of an Octet Truss. *Acta Mater.* 149, 78–87 (2017).
33. Rajan, V. P., Rossol, M. N. & Zok, F. W. Optimization of Digital Image Correlation for High-Resolution Strain Mapping of Ceramic Composites. *Exp. Mech.* 52, 1407–1421 (2012).
34. Hunt, H. E. M. Mechanical strength of ceramic honeycomb monoliths as determined by simple experiments. *Chem. Eng. Res. Des.* (1993).

Table 2.1: Nomenclature

t	Strut thicknes	θ	Inclination angle
u	Transverse displacement	μ	Friction coefficient
v	Axial displacement	σ_a	Applied stress
E_l	Young's modulus of a lattice	σ_c	Compressive stress
E_s	Young's modulus of parent material	σ_t	Tensile stress
F_a	Applied force per unit depth	σ_y	Strut material yield stress
F_c	Compressive force per unit depth	ω	Rotation
F_l	Critical force for surface node sliding	Γ	Non-dimensional buckling parameter
F_n	Axial force on a node	Λ	Non-dimensional yielding parameter
F_t	Tensile force per unit depth	Σ_a	Normalized applied stress per unit depth
H	Primitive unit cell height	Σ_c	Normalized compressive stress per unit depth
K	Effective length factor	Φ_a	Normalized applied force
L	Strut length	Φ_c	Normalized compressive force
L^*	Pertinent strut length		
R_h	Node radius		Recurring subscripts:
U_e	Elastic strain energy	0	Initial value
U_w	Work	t	Tensile/transverse strut property
W	Primitive unit cell width	c	Compressive/inclined strut property
α	normalized effective strut length		Recurring superscripts:
γ_{xy}	shear strain	*	Critical value for strut rupture
ε_a	Nominal compressive strain	<i>buc</i>	Critical value for strut buckling
ε_a^{den}	Densification strain	<i>eff</i>	Effective property
ε_c	Compressive strain	max	Maximum value
ε_{eq}	von Mises equivalent strain	<i>yield</i>	Critical value for strut material yielding
ε_x	Strain in x-direction		
ε_y	Strain in y-direction		

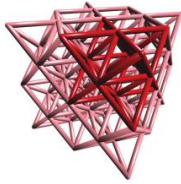
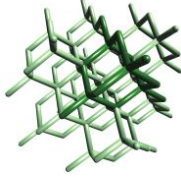
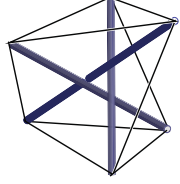
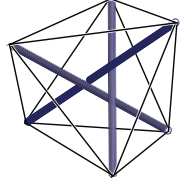
	Lattices		Tensegrities	
Prototypes				
	Stretch-dominated FCC lattice	Bend-dominated diamond cubic lattice	Minimal class 1 tensegrity	Non-minimal class 1 tensegrity
Physical characteristics	<ul style="list-style-type: none"> • One phase: strong, stiff material • Contiguous strut network • Rigid joints • No pre-stress 		<ul style="list-style-type: none"> • Two phases: one rigid, one extensible • Discrete struts, contiguous spring network • Pinned joints • Pre-stressed springs 	

Figure 2.1: Single-material lattices and tensegrities exhibit contrasting physical characteristics. *Minimal* tensegrities contain the fewest springs needed for stability; *non-minimal* tensegrities contain more. In class 1 tensegrities, compressive struts do not touch one another ²⁹.

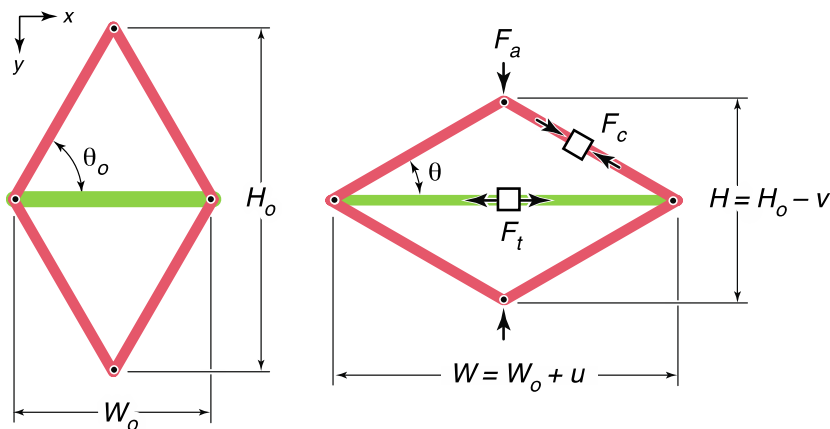


Figure 2.2: Compressive force applied to the primitive bi-material structural motif is distributed through compression of the inclined struts (orange) and tension of the transverse strut (green). Geometric changes are manifested in rotations of the inclined struts and stretching of the transverse strut.

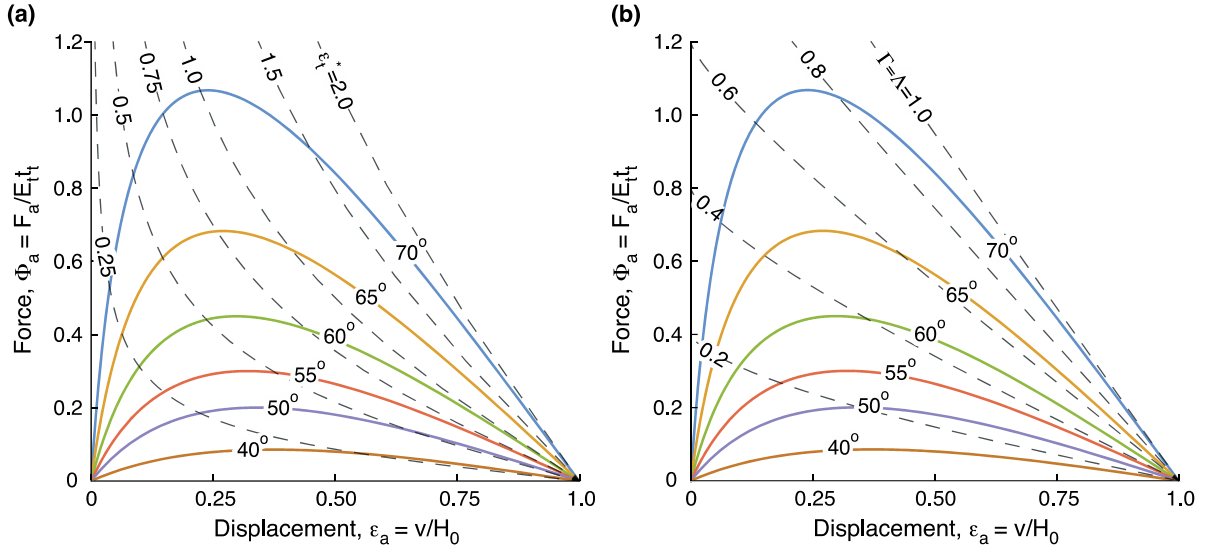


Figure 2.3: Compressive response of the primitive structural motif depends sensitively on the inclination angle of the inclined struts. Loci of (a) constant tensile failure strain ϵ_t^* and (b) constant buckling parameter Γ and constant yielding parameter Λ illustrate trade-offs between properties, geometry, and materials. (Here the contours for critical values of Γ and Λ are coincident with one another, as evidenced by Eqs. 2.5 and 2.6).

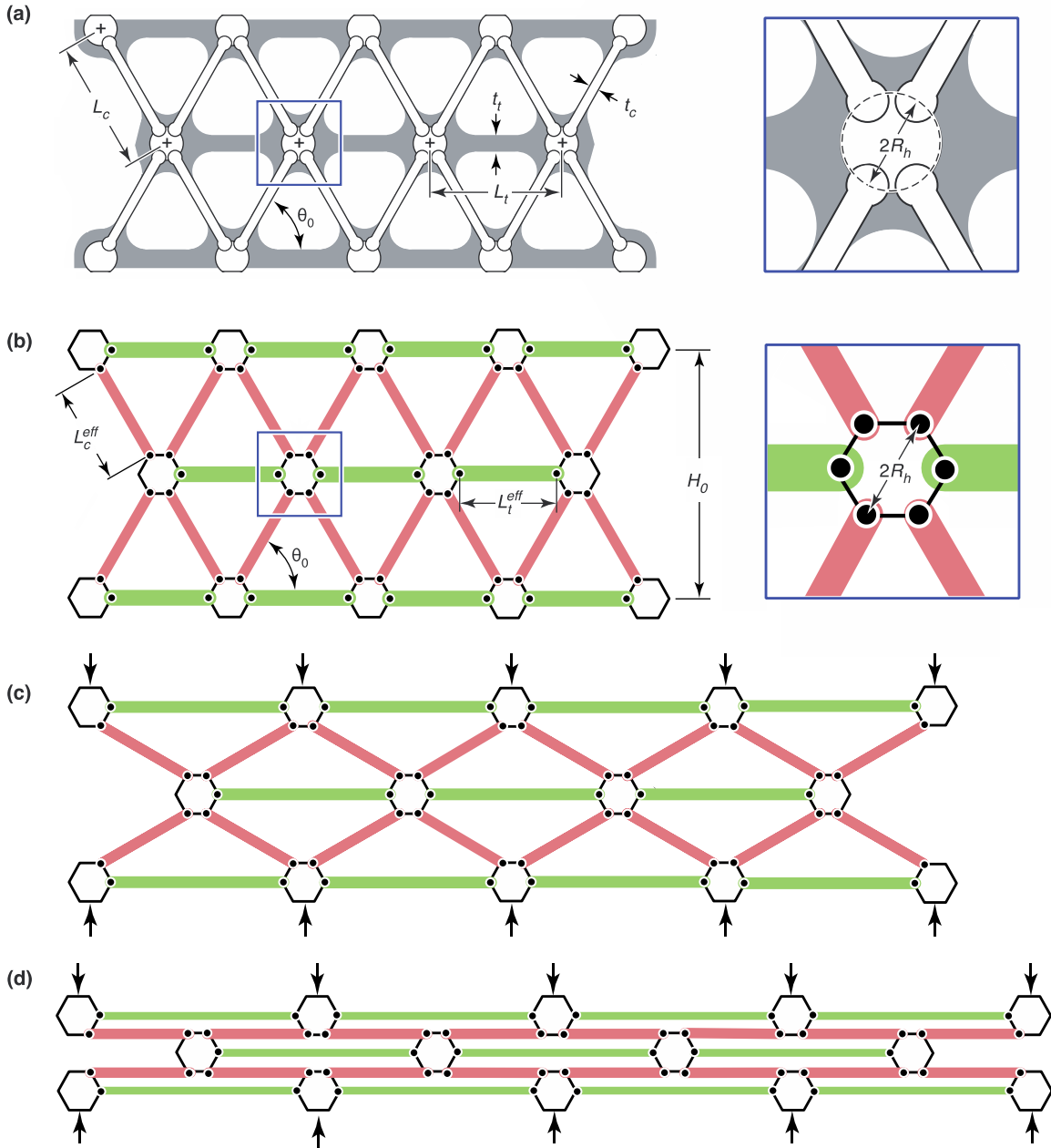


Figure 2.4: (a) The bi-material lattice design is based on the primitive structural motif. (b) The mechanics analyses assume that the struts are pinned to rigid hubs at the locations indicated. (c) Application of compressive force leads to stretching of the transverse struts and rotation of the inclined struts. (d) Densification is attained when the initially-inclined struts are horizontal. Pertinent dimensions of the test samples are: $H_0 = 46.8$ mm, $L_t = 27$ mm, $t_t = 4$ mm, $L_c = 27$ mm, $t_c = 2$ mm, $R_h = 3.5$ mm, $\theta_0 = 60^\circ$.

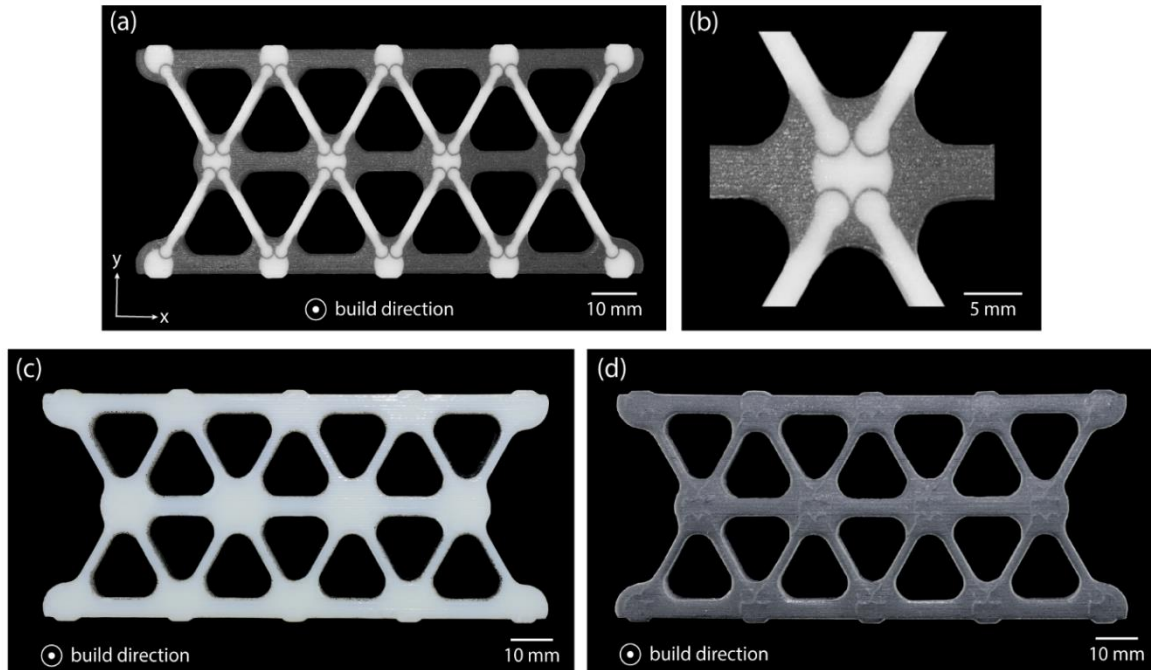


Figure 2.5: Photographs of a printed bi-material lattice showing (a) distributions of acrylic-like material (white) and elastomeric material (gray), and (b) node geometry, including the ball and socket joint with a thin intervening layer of elastomer, as well as single-material lattices of (c) acrylic-like material and (d) elastomeric material.

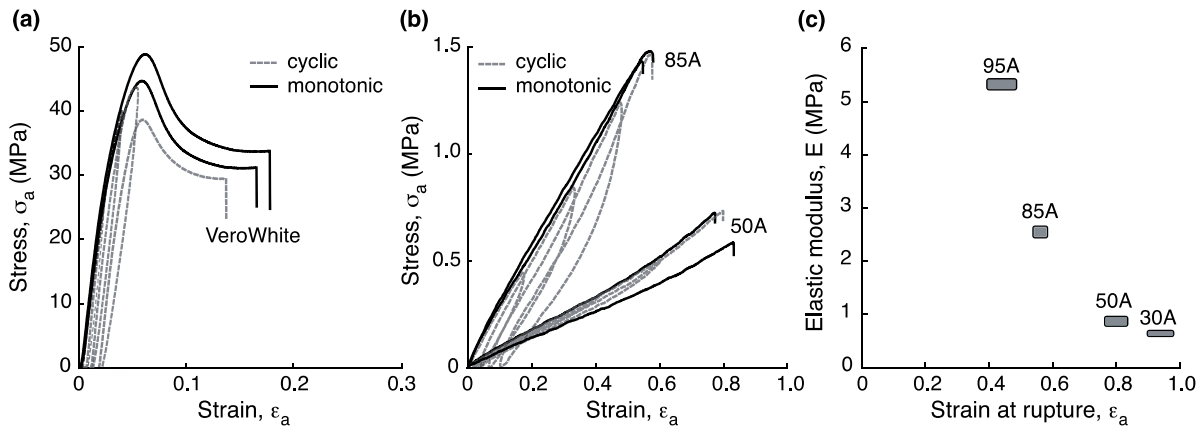


Figure 2.6: Tensile stress-strain curves of the acrylic-like material (VeroWhite) and two representative elastomers (Agilus 50A and 85A) demonstrate the vast differences in stiffness, strength, and ductility of the lattice constituents. While the VeroWhite exhibits a modulus of about 1.4 GPa and a tensile strength of about 40 MPa, the elastomers exhibit moduli that are about three orders of magnitude lower (several MPa) and strengths that are an order of magnitude smaller (also several MPa).

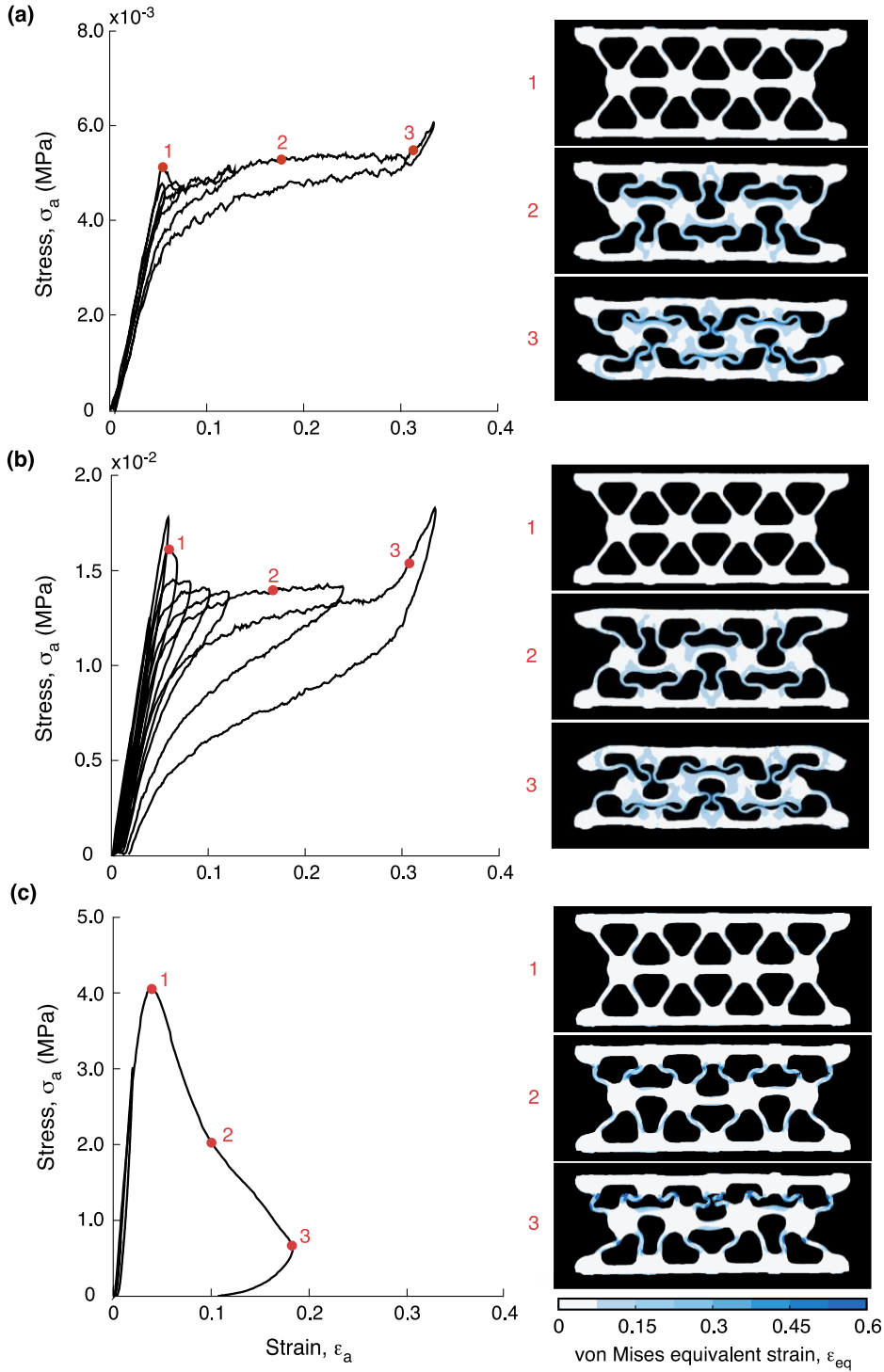


Figure 2.7: (a, b) Stress-strain curves of single-material elastomeric lattices and von Mises equivalent strain maps at select points reveal buckle initiation at the first stress peak and a subsequent nearly-constant crushing stress (characteristic of elastic buckling). (c) Corresponding results for VeroWhite show a much higher strength, dictated by elastic/plastic buckling, and subsequent strain softening due to collapse of the buckled struts. (Note the large differences in scales on the ordinates).

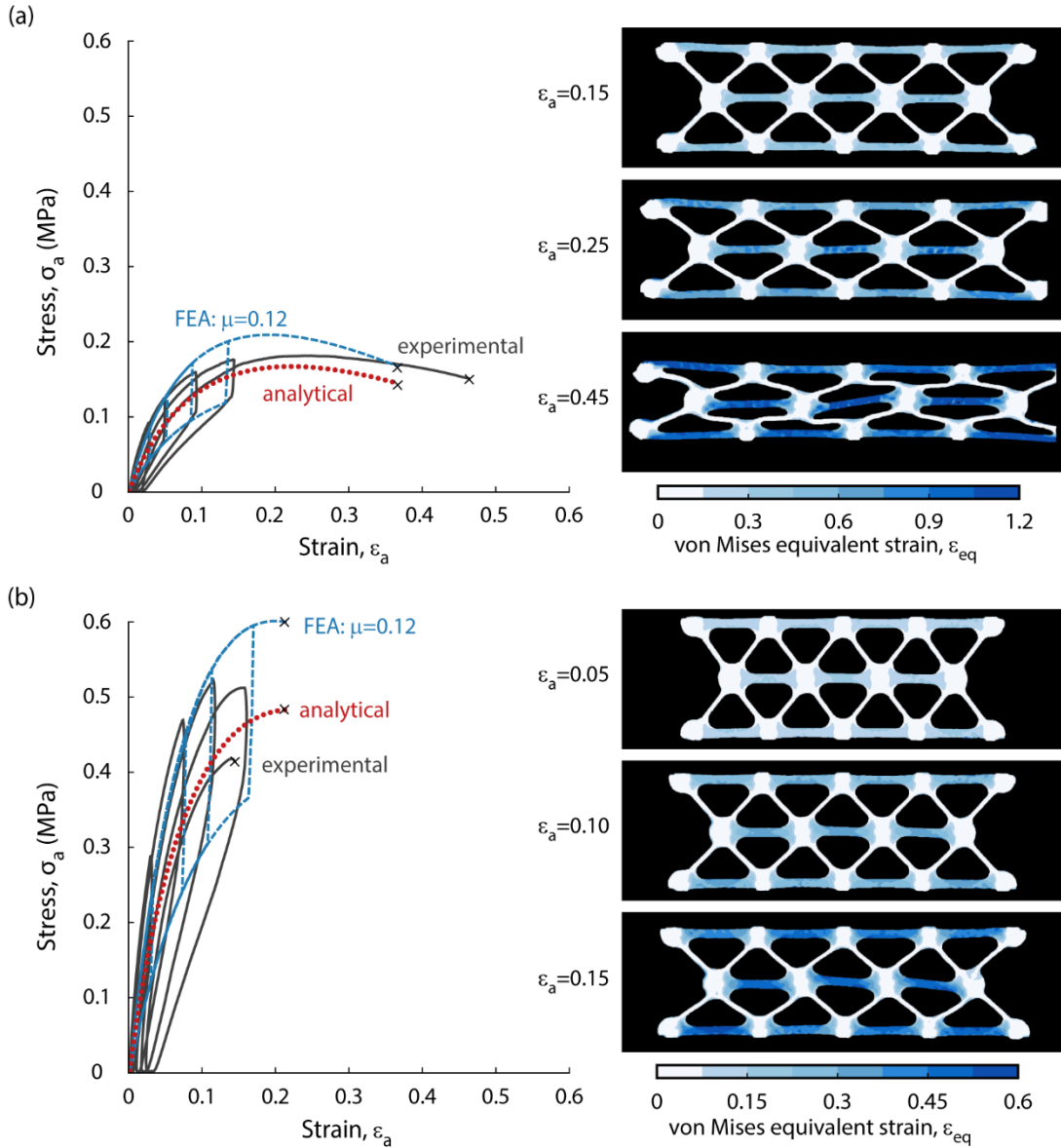


Figure 2.8: Compressive responses of bi-material lattices comprising VeroWhite and either (a) Agilus 50A or (b) 85A demonstrate the tradeoffs between stiffness and ductility of the constituent elastomers. Also shown are the results from the analytical model and the FEA simulations. Strain maps at select points during deformation show that macroscopic straining is accommodated by stretching of the transverse struts and rotation of the inclined struts. Most features here are captured by the FEA simulations. The role of damage is evidenced by the tests in (b). Here the strain attained in one cycle exceeded the strain at which strut rupture occurred on the next loading cycle.

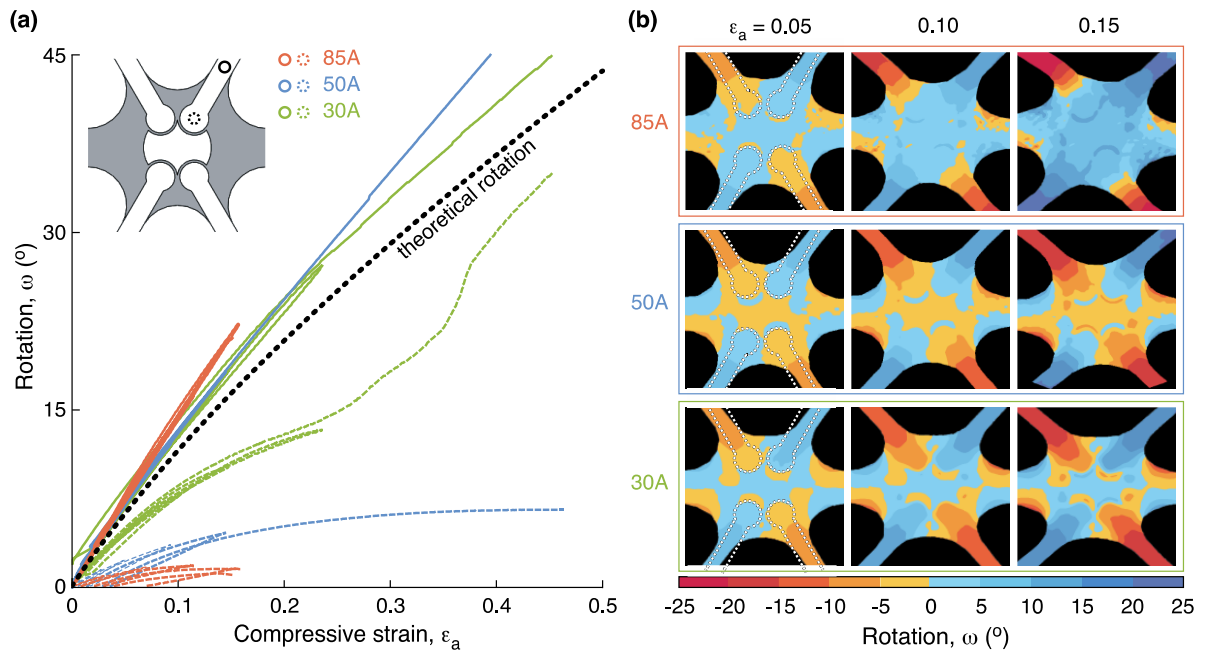


Figure 2.9: (a) Rotations measured at short distances from the ball centers match the values predicted from a geometric model assuming pinned joints. In contrast, rotations at the ball centers are considerably lower, falling well below predictions, and vary significantly with the stiffness of the elastomer. (b) Full field rotation maps of the central nodes show increasing uniformity within the struts as the modulus of the elastomer decreases (from top to bottom). Dashed lines in the first of each series of maps denote the boundaries of inclined struts in their original (unstrained) position.

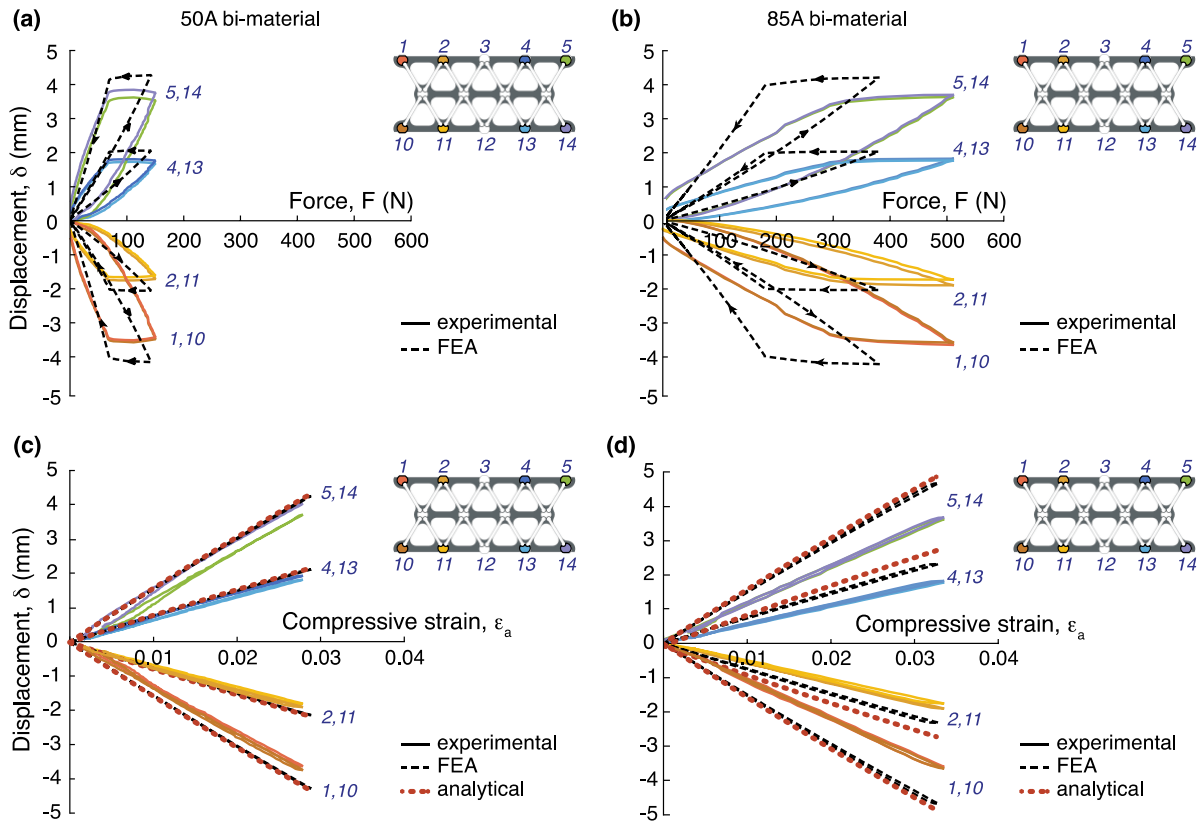


Figure 2.10: All surface nodes apart from the central ones begin to slide laterally essentially at the onset of loading. (a,b) Differences between predictions and measurements appear somewhat elevated when node displacements are plotted against load (rather than applied strain). (c,d) Predicted node displacements from FEA (dashed lines) and the analytical model (dotted lines) are broadly consistent with but of slightly higher magnitude than those measured in both 50A and 85A bi-material lattices (solid lines).

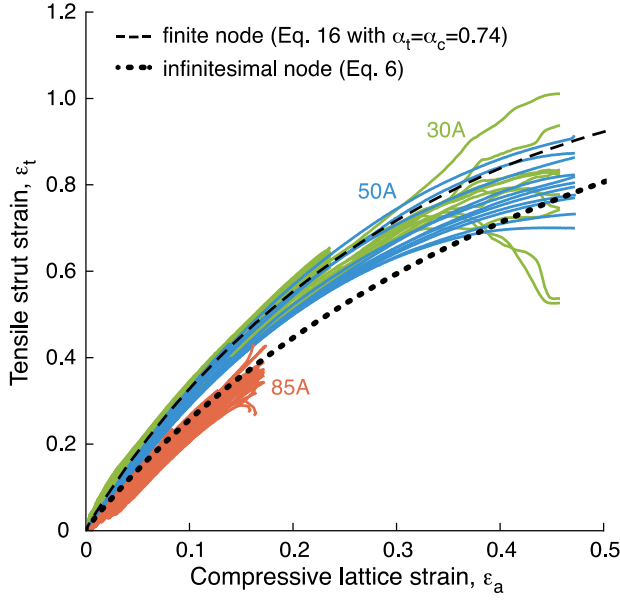


Figure 2.11: Tensile strains measured in the transverse struts of three bi-material lattices are more accurately predicted by an analytical model that accounts for the reduction in strut length due to finite node sizes.

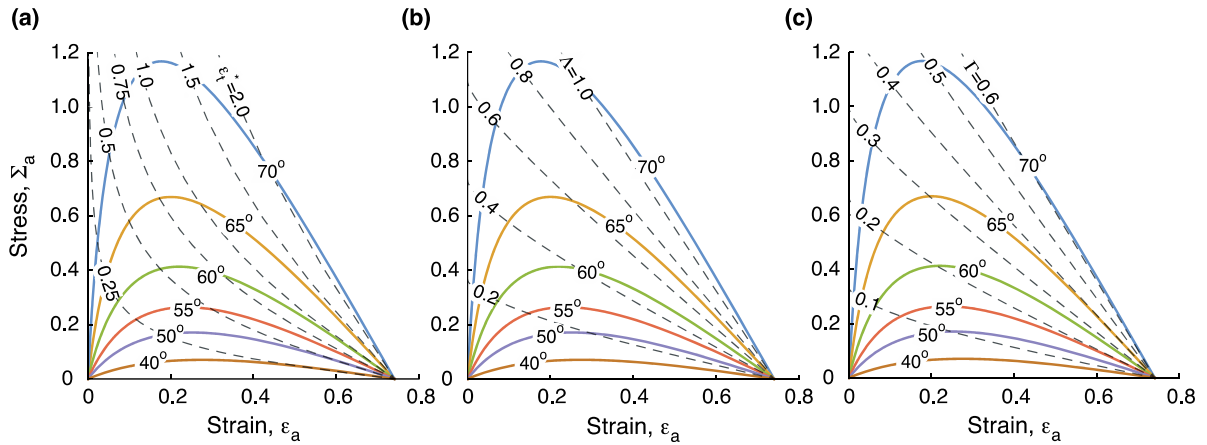


Figure 2.12: Predicted stress-strain curves and failure loci of bi-material lattices with finite node size and with edge effects are similar to those of the primitive structural motif (in Fig. 2.3). Failure loci correspond to (a) transverse strut failure, at a strut strain ε_t^* , (b) yielding of inclined struts, at a strut stress Λ , and (c) buckling of inclined struts, at a strut stress Γ .

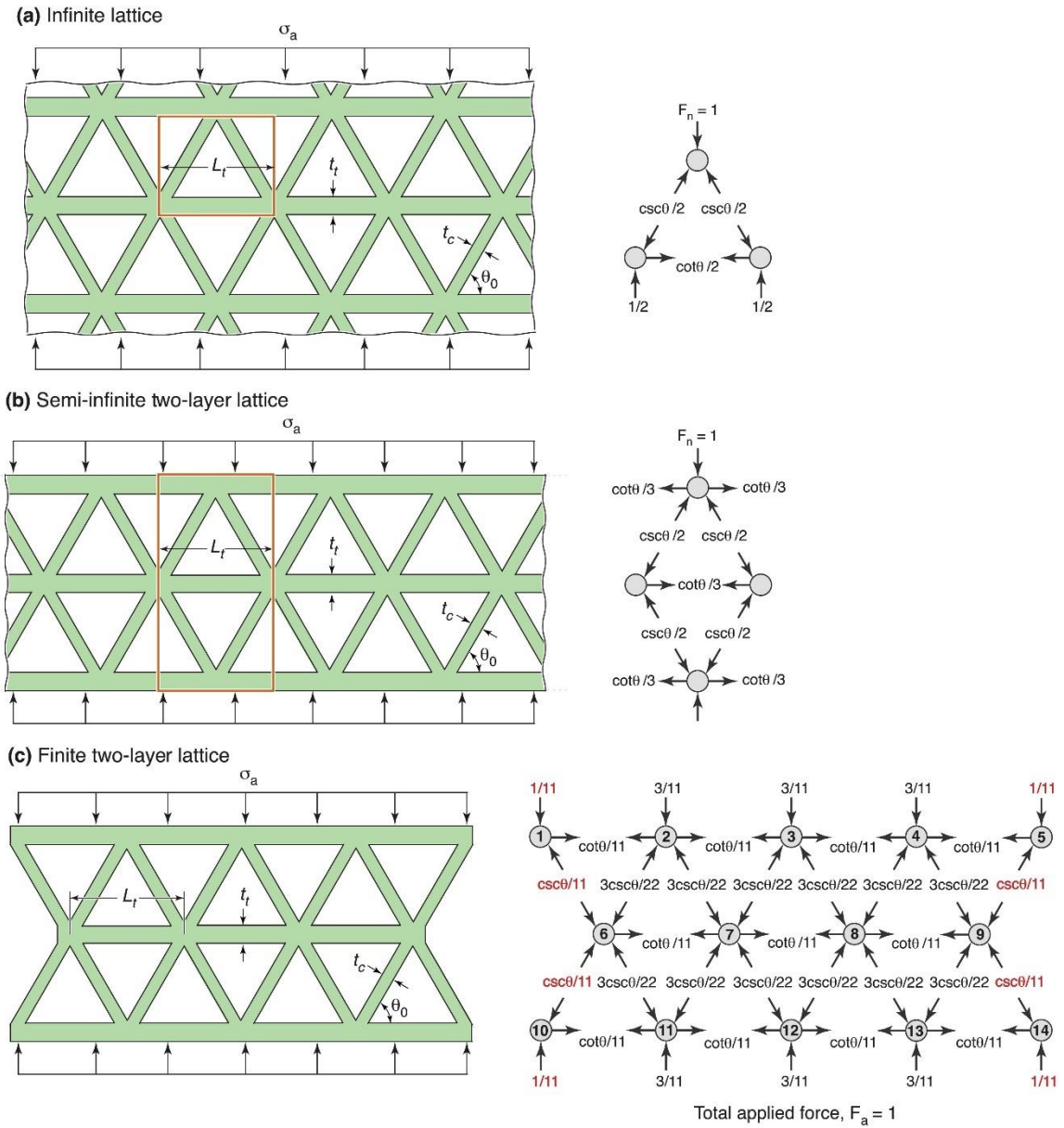


Figure 2.A1: Geometries of triangulated lattices and forces acting on nodes and constituent struts subject to macroscopic compressive loading. Effects of boundaries on nodal and strut forces in the finite two-layer lattice (in (c)) are indicated by red font.

Chapter 3

A 3D Bi-material Lattice Concept for Tailoring Compressive Properties

Abstract

²The current chapter explores 3D bi-material lattice concepts for tailoring compressive stress-strain response. The unit cells of the lattices consist of six stiff inclined struts that together form the edges of two stacked tetrahedra. The central plane (between the two tetrahedra) contains elastomeric elements that stretch when the lattice is compressed. The geometric configurations of the elastomers examined here include: (i) straight struts between each node pair within the central plane, (ii) multiple struts between each node pair, including one straight strut and one or more curved struts, and (iii) flat sheets, either uniform or graded in thickness, connected at the mid-plane nodes. Assessments of the concepts are made using analytical models, finite element simulations, and experiments on lattices fabricated by 3D printing. The experimental results affirm the understanding of mechanical response gleaned from the models and highlight the importance of joint design in attaining large straining capacity and strain reversibility. Measured responses from each structure demonstrate the benefit of implementing a sheet-based design over a strut-based design as the load bearing capacity nearly doubles. Sheet-based unit cell results also raise the prospects for computational design optimization for maximum efficiency in material use.

² The content of this chapter has previously appeared in *Materials and Design* (Ruschel, Amanda L., et al. "A 3D Bi-material Lattice Concept for Tailoring Compressive Properties." *Materials & Design* (2022): 111265.). Available at: <https://doi.org/10.1016/j.matdes.2022.111265>

3.1 Introduction

The advent of multi-material 3D printing has greatly expanded the design landscape for periodic lattice materials. For single-material lattices, the core features of that landscape include (Fig. 3.1): (i) network topology, describing the nodal connectivity of the constituent struts; (ii) network morphology, defined by the spatial relationships between node locations; (iii) properties of the constituent strut material; (iv) strut morphology, characterized by strut shape and dimensions; and (v) node (or joint) morphology, characterized by shape and dimensions ¹. Extending this to multi-material lattices introduces a plethora of additional design options, some of which are shown schematically in Fig. 3.1. The recent literature is replete with examples illustrating the rich diversity of possibilities ²⁻¹⁶.

In one case, a lattice with a core-shell strut structure was produced using a hard but brittle epoxy (for the shell) and a soft, ductile epoxy (for the core) (Mueller et al., 2018). With appropriate tailoring of the interface between the two epoxies the core-shell struts were shown to be twice as strong as and yet comparably ductile to struts made from the soft epoxy alone. Lattices made from the core-shell struts showed similar strength improvements without a significant debit in straining capacity. In another case, lattices were fabricated using two polymers with dissimilar glass transition temperatures ¹⁴. At ambient temperature the stiffnesses of the two polymers were the same as one another and thus the stiffness of the lattice was same as that of a single-material lattice. At elevated temperature – between the two glass transitions – the stiffness of one population of struts dropped by several orders of magnitude while that of the remaining struts remained almost unchanged. The lattice properties changed accordingly, though the process was fully reversible upon return to ambient temperature. Materials with disparate glass transition temperatures have also been used in lattices to control

deformation modes ¹⁶ and undergo reversible shape morphing ^{9,15}. Yet other studies have probed additional properties and materials design strategies, including: use of multi-material multi-layered struts for lattices with tailorable negative swelling ratios ⁴; struts comprising sandwich structures of materials with highly disparate damping characteristics for lattices with tailored dynamic damping properties ⁵; and macroscopic spatial distributions of stiff and compliant struts for tailoring stiffness and Poisson's ratio ⁷. In another case, a bi-material lattice was designed such that struts that were to carry compressive loads were made from a stiff, strong material while those to carry tension were made from a highly extensible material ⁶. The latter example sets the foundation for the current study.

The introduction of multiple materials into a single lattice structure highlights the importance of *joint design* (Fig. 3.1m). Viewed broadly, joint (or node) design for lattices – whether single-material or multi-material – remains a sparsely explored field, despite the recognition that joints are often the weak links in the structure ^{17–19}. When dissimilar materials are combined, the adhesive strength of interfaces between them is the primary concern ^{12,20}; stress concentrations associated with elastic property mismatch are also likely to strongly promote failure. Going beyond the intrinsic interface properties, joint design involves the geometric configurations of the two materials in the joining regions. Simple straight joints (e.g., butt or lap joints) are likely to be the least robust and probably undesirable in cases where the macroscopic lattice strains are large, and the joints undergo large local displacements. With the flexibility of modern multi-material printers, innovative solutions derived from related fields of engineering or biology can be used to design joints with the requisite mechanical characteristics. For example, in human joints, articular cartilage and synovial fluid reduce both friction and contact forces between bones ²¹. Analogous effects have been obtained using

compliant elastomer interlayers between hard contacting surfaces within articulating joints in lattice materials (Wang et al., 2015; Ruschel and Zok).

The objective of the current article is to present a concept for a 3D bi-material lattice with tunable compressive stiffness and strength combined with high straining capacity and strain reversibility. The concept builds and improves upon an analogous 2D version presented earlier ⁶. The resulting design is guided by three principles:

- (i) Where printing capabilities allow, material selection is guided by *local mechanical or functional requirements*. For example, materials for structural members that are to carry compressive loads should be stiff and strong, to inhibit buckling and yielding; maximum straining capacity (especially in tension) is a secondary consideration. In contrast, materials for members to be loaded in tension should have high straining capacity without instabilities (i.e., necking). The latter requirement combined with strain reversibility led to the selection of elastomers as the materials of choice.
- (ii) Joints between dissimilar materials must ensure effective load transfer *without excessive stress concentrations* and without undue constraints on strut deformation and rotation. That is, tensile members ideally should be loaded in uniaxial tension while compressive members should be loaded in uniaxial compression, even following large macroscopic deformation. These goals lead to the requirement that struts at joints articulate freely, avoiding rotational constraints that induce bending of adjoining members. In the 2D concept presented previously ⁶, limited articulation was facilitated by hinged joints containing thin compliant interlayers between hard contacting surfaces. While this approach was somewhat effective in allowing large macroscopic deformation without rupture, the constraints on articulation were excessive, as manifested in strut bending.

(iii) The intended deformation and rotation of constituent members should be attainable under *macroscopic 1D straining* (the condition most frequently encountered in energy absorbing systems). In this regard the previous 2D design was deficient; large macroscopic compressive strains led to large transverse tensile strains with a plastic Poisson's ratio near 1. These strains were accommodated by frictional sliding at the interfaces between the external lattice faces and the loading platens. Preferred lattice designs would accommodate all lateral deformation internally within the structure with a plastic Poisson's ratio near 0.³

The article is organized in the following way. A primitive structural motif of a 3D bi-material strut-based lattice with the desired characteristics (described above) is presented and analyzed in Section 3.2. Details of implementation and assessment of the concept are presented in Section 3.3. The assessment methods include analytical mechanics models, finite element simulations, and mechanical tests on structures made by 3D printing. Building on the results for lattices with straight struts, two design variants are explored: one based on the addition of *curved* struts to the straight struts connecting midplane nodes and another with triangular *sheets* in place of struts in the midplane. Both are described in Section 3.4. Key conclusions are summarized in Section 3.5.

³ The plastic Poisson's ratio is viewed with respect to the two face sheets enclosing the lattice. For the 2D structure cited, deformation internal to the lattice is accompanied by transverse straining of the face sheets; a finite (large) plastic Poisson's ratio is obtained. Consequently, uniaxial compression leads to frictional sliding at the external boundaries. A zero plastic Poisson's ratio is obtained when the internal lattice deformation does not lead to straining of the face sheets. In this case the structure as a whole does not experience transverse strains when loaded in uniaxial compression. In principle, this goal is achievable with the concepts described herein.

3.2 Bi-material Lattice Design

3.2.1 Primitive Motif and Mechanics Analysis

A primitive 3D structural motif that exhibits the desired behavior is illustrated in Fig. 3.2. It consists of six inclined struts and three transverse struts that together form the edges of two stacked tetrahedra. The struts are assumed to be connected by pinned joints. The inclined struts are made of a stiff, strong material and the transverse struts from a highly extensible material. Under macroscopic compression (along the y-direction), the load is distributed through axial compression of inclined struts and axial tension of the transverse struts. As the structure is compressed, inclined struts rotate to allow for transverse strut stretching. In principle this motif could be repeated in space, with due consideration for cell spacing and cell shape when the structure is compressed to the limit, thereby forming a large multi-cell structure with 1D straining capability.

At the simplest level, the compressive response of the structural motif is modelled assuming that inclined struts are rigid, strut thicknesses are infinitesimal, and transverse struts are elastomeric with linear engineering stress-strain response. (Details of the analysis are in Appendix 3.A1. All results were checked by finite element analysis.) The predicted macroscopic response is given by

$$\Phi_a \equiv \frac{F_a}{3E_t A_t} = \frac{\sqrt{3}}{2} (1 - \varepsilon_a) \left[\tan \theta_0 - \left(\csc^2 \theta_0 - (1 - \varepsilon_a)^2 \right)^{-1/2} \right] \quad (3.1)$$

where Φ_a is a normalized force; F_a is the applied force; E_t and A_t are the Young's modulus and the cross-sectional area of the transverse strut, respectively; θ_0 is the initial strut inclination angle; ε_a is the nominal compressive strain, defined by $\varepsilon_a = v/H_0$; v is axial displacement;

and H_0 is the initial height. (The factor 3 in the normalized force accounts for the presence of three transverse struts.) The results are plotted in Fig. 3.2b for several values of q_0 .

Absent tensile rupture of the transverse struts or buckling or yielding of compressive struts, the structural response, $\Phi_a(\varepsilon_a)$, exhibits: (i) a rising portion with an initial stiffness of $d\Phi_a/d\varepsilon_a = (\sqrt{3}/2)\tan^3\theta_0$; (ii) a maximum at a strain of $\varepsilon_a^{\max} = 1 - \csc\theta_0(1 - \cos^{2/3}\theta_0)^{1/2}$ and a force of $\Phi_a^{\max} = (\sqrt{3}/2)(\sec^{2/3}\theta_0 - 1)^{3/2}$; and (iii) a softening portion ending at $\Phi_a = 0$ when $\varepsilon_a = 1$. The shapes of the curves are the result of two competing mechanisms: hardening due to increasing transverse strut stretching and geometric softening due to decreasing inclination angle of the inclined struts.

Achieving this response without failure relies on judicious selection of strut materials, strut dimensions and cell geometry. Guidelines for designing lattices against the most ubiquitous failure modes (strut rupture, buckling, and yielding) are given in Appendix 3.A1. These guidelines serve as the basis for the following lattice designs and the selections of strut materials.

3.2.2 Concept Implementation

The design of a 3D bi-material structure based on the primitive motif is shown in Fig. 3.3a. Hinged knob-and-socket joints are used to facilitate strut rotations within a single plane without strut twisting. To this end, cylindrical knobs are integrated into the ends of the inclined struts. Each knob is mated and interlocked within a corresponding cylindrical socket in a hard knuckle. Each of the stationary knuckles, at the top and bottom of the structure, is designed to accept three struts. The interlocking design ensures that the knobs cannot be easily extracted

from the sockets. Each of the three central joints comprise a knuckle that accepts two inclined struts. The knuckle is partially encapsulated by the elastomeric material which then smoothly transitions into the transverse struts. These joints allow simultaneous rotation of inclined struts *and* stretching of transverse struts with minimal bending.

Multiple test specimens of the structure (Fig. 3.3b) were fabricated in a single print operation using a multi-material 3D printer (J750, Stratasys). Inclined struts were made of a stiff, acrylic-like material (Vero) and transverse struts were made of an elastomer (Agilus 30A). The ductility of the elastomer was high enough to prevent strut rupture when the lattice was fully compressed (i.e. $\varepsilon_t^* > 0.83$, calculated from Appendix 3.A2). A thin (ca. 250 μm) layer of fugitive support material was placed between the knob surface and the corresponding socket surface; its removal after printing (via immersion in a suitable solvent) produced a gap that prevents fusion of the knob to the socket (Fig 3.3a black boxes).

The mechanical properties of the constituent materials reported by the material manufacturer were augmented with results from independent tensile tests on dog-bone specimens printed in the same way. Elastomeric samples (Agilus 30A) were designed following ASTM D412 standards, and acrylic-like (Vero) samples were designed following ASTM D638 standards. Each sample was tested in uniaxial tension at a strain rate of 10^{-4} s^{-1} . Results from these tests are provided in Fig. 3.4.

3.3 Concept Assessment

3.3.1 Materials and Test Methods

The printed structures were tested in uniaxial compression at a nominal strain rate of 10^{-4} s^{-1} . Mechanical tests were accompanied by 3D digital image correlation (DIC) (VIC-3D, Correlated Solutions, Inc, Irmo, SC) to track displacements, strains, and rotations. Prior to

testing, test specimens had been coated with aerosol paint to create random speckle patterns. Specimen preparation and image analysis were done following the guidelines laid out previously^{22,23}. Specimens were imaged with a scale factor of 42 $\mu\text{m}/\text{px}$. Images were analyzed using incremental correlation with a subset size of 21 pixels (880 μm) and a step size of 2 pixels (84 μm). The macroscopic compressive strain was obtained from the DIC data using three virtual extensometers spanning the distance between the centers of top and bottom nodes. The force was obtained from a load cell. Several unload-reload cycles were performed to probe hysteresis effects.

3.3.2 Finite Element Simulations

Corresponding finite element simulations were performed using Abaqus/Standard (Version 2018, Dassault Systems, Providence, RI). The model geometry was based on the CAD file used for printing. To improve computational efficiency, only one-third of the cell was modeled, utilizing the threefold rotation symmetry about the y-axis. The model contained a total of >27,000 elements (with a density of about 14 elements/ mm^3). Acrylic-like material components were meshed using hexahedral elements (C3D8R) and elastomeric components were meshed with hybrid tetrahedral elements (C3D10H). Tetrahedral elements were used because of the complex geometry of the structure, and hybrid elements were used because the material was modeled as incompressible. A mesh convergence study indicated that the model resolution was sufficient to accurately capture the macroscopic load-displacement response.

The material for the inclined struts and the adjoining knuckles was treated as linear elastic with Young's modulus $E_c = 1.35 \text{ GPa}$ and Poisson's ratio 0.3 (Fig. 3.4a). The material for the transverse strut was modeled using the Arruda-Boyce incompressible hyperelastic constitutive law, calibrated to the measured stress-strain curves (Fig. 3.4b). Details of the

constitutive law and its calibration are given in Appendix 3.B. Contact interactions within the knuckle were described by a friction coefficient of $\mu = 0.5$; this value lies within the range of coefficients reported for acrylic surfaces²⁴. Cyclic compression was simulated by prescribing top-surface displacement profiles that follow those used in the experiments (three progressively larger cycles of loading and unloading) while the bottom was held fixed.

3.3.3 Analytical Model

The experimental measurements and FEA results were also compared with the predictions of an expanded version of the analytical model for the primitive structural motif. Specifically, the model leading to Eqn. 3.1 was modified to account for the finite dimensions of the printed structure (especially in and around joints). Here again the inclined struts are assumed to be much stiffer and stronger than the transverse struts and the joints are assumed to be hinged.

The main effect of finite joint size is to reduce the effective length of inclined and transverse struts, L_c^{eff} and L_t^{eff} , respectively (Fig. 3.5). Normalizing these by the respective distances between node centers, L_c and L_t , yields the non-dimensional strut lengths $\alpha_c \equiv L_c^{eff} / L_c$ and $\alpha_t \equiv L_t^{eff} / L_t$. Incorporating these effects in the mechanics analysis, the lattice response becomes:

$$\Phi \equiv \frac{F_a}{3E_t A_t} = \frac{\sqrt{3}}{2} \left(\frac{\alpha_c - \varepsilon_a}{\alpha_t} \right) \left[\tan \theta_0 - \left(\csc^2 \theta_0 - \left(1 - \frac{\varepsilon_a}{\alpha_c} \right)^2 \right)^{-1/2} \right] \quad (3.2)$$

Additional details of the analysis are in Appendix 3.A2. The analysis can be refined further to account for the hyperelastic constitutive law, as described in Appendix 3.B. While this refinement enables somewhat more accurate predictions of lattice response, it yields no additional insights into the mechanics of lattice deformation.

3.3.4 Experimental Measurements and Analytical Model Predictions

The measured response of the printed structure (Fig. 3.6) resembles the analytical model predictions. Upon loading, the stress rises nonlinearly and attains a peak at a strain of about 0.32. The accompanying strain maps in Fig. 3.6c illustrate the geometric changes and highlight the large strains in the transverse struts and negligible strains in the inclined struts. Cycling occurs without failure and the structure recovers to its initial state upon unloading.

Although the two responses are similar, they differ in two ways. First, the measured loading and unloading curves exhibit hysteresis, manifested as load changes at almost constant displacement during the initial stages of load reversal. The analytical model prediction, in contrast, is equivalent for both loading and unloading. Interestingly, the model prediction falls nearly midway between the measured loading and unloading curves. This behavior is a clear indication of internal friction. Second, at a strain of about $\varepsilon = 0.26$, the tangent modulus of the measured curve exhibits a sudden increase; the stress subsequently reaches a second peak, at a strain of 0.30-0.34, and then gradually diminishes. The predicted response lacks this feature. Both effects are addressed in the following section.

Additional insights are gleaned from the rotations. Rotations were measured from the DIC data at two points along each inclined strut and two points along the centerline of adjoining knuckles (along the midplane of the structure). Measurement locations are indicated by filled circles on Fig. 3.7c and the measurements plotted on Fig. 3.7a. The two struts rotate at similar rates, one clockwise and the other counterclockwise. Both coincide closely to the predicted rotations. However, while the model assumes that the knuckles joining the inclined struts to the transverse struts remain stationary (indicated by the dotted lines in Fig. 3.7), the

measurements show that, in fact, knuckle rotation initially proceeds similarly to one of the two adjoining struts. That is, rather than the two struts rotating past the knuckle in a symmetric fashion, one of the struts “sticks” to the knuckle for some period of loading. At a critical point, the knuckle becomes “unstuck” and begins to rotate in the opposite direction. The pattern is repeated at the same point during each unloading/reloading cycle. This, too, is addressed in the following section.

3.3.5 Finite Element Analysis

The FE model predictions are assessed by comparing them with the measured stress-strain curves, including the hysteresis upon loading/unloading and the rotations of the struts and knuckles at the joints. At low strains (to $\varepsilon = 0.03$), the stiffnesses from the measurements and the finite element simulations are within 10% of one another in the first loading cycle. Additionally, the sudden increase in stiffness at $\varepsilon = 0.26$ in the measured response is captured by the FE model, albeit at a slightly higher strain ($\varepsilon = 0.31$). The origin of this stiffening emerges from an examination of joint and strut rotations during deformation, plotted on Figs. 3.7a-b.

For both the experimental measurements and the FE simulations, the joints begin to rotate almost immediately after loading (at about $\varepsilon = 0.02$). Key points in the rotational response are illustrated by cross-sections through the joints and the struts from the FE model in Fig 3.7c. At the onset of loading, at the point labelled 1, the compressive force lines run through the two inclined struts and intersect along the centerline of the knuckle. Similarly, the tensile force line in the horizontal strut (indicated by the horizontal arrow) also passes through the knuckle centerline. The implication is that no bending moment is exerted on the knuckle. But, as the structure is compressed to a finite strain, asymmetric strut rotation occurs; at point

2, the bottom strut has rotated about 25% more than the top strut. Because of this asymmetry, the compressive force lines no longer intersect at the knuckle centerline and thus a bending moment is generated in the knuckle. This is an inherent instability in the design: for frictionless contacts, even an infinitesimal misalignment of the struts would lead to one strut beginning to rotate before the other. The knuckle and the top strut then remain stuck together and rotate in tandem. At the same time, an opposing moment is generated because of the resulting misalignment of the tensile force in the transverse strut (see point 3), but evidently this moment is insufficient to arrest continued knuckle rotation. At a critical strain, indicated by point 4, the external surface of the knuckle (near the start of the socket) makes contact with the strut at the base of the knob, causing the joint to temporarily “lock up”. This marks the onset of stiffening, at a strain of $\varepsilon = 0.31$. With additional applied force, the contact between the bottom strut and the inner knuckle creates a moment that rotates the knuckle in the opposite (clockwise) direction. This continues up to high strains until, near the point at which the entire structure locks up, the knuckle has rotated back to its original configuration. Upon unloading, rotation follows the same path as it did during loading, reversing direction at the same strain. This sequence continues through the subsequent loading/unloading cycles.

As noted, knuckle rotation is a result of an inherent mechanical instability. Performing the same FE simulations assuming frictionless contacting surfaces yields the same knuckle rotation history and similar macroscopic response, with stiffening occurring at the same strain. Whether this instability has substantive consequences in the structural response upon repeated loading and unloading remains to be ascertained.

Each load reversal is accompanied by a change in load with only a small change in macroscopic strain. This leads to the characteristic hysteresis loops shown in Fig 3.6. As noted

previously, the hysteresis is attributed to internal friction between the knobs at the ends of the inclined struts and the knuckle sockets. Incorporating friction into the finite element model and using a friction coefficient of $\mu = 0.5$ yields predictions that accurately capture the magnitude of the load drops ($\Delta\Phi_a \approx 0.08$) and the resulting hysteresis. These results highlight the importance of joint design in multi-material lattices.

3.4 Concept Variations

3.4.1 Preliminaries

Building on the preceding lattice design, two additional concepts were identified and assessed. The design modifications reflect the understanding that the stress-strain response of the current lattice is dictated largely by the elastomeric material and its geometric configuration. Accordingly, the new designs focus on the elastomeric components.

In one design, curved struts are added to the three straight struts in the existing design. The goal is to extend the hardening regime in the macroscopic response through structural elements that initially bear little load but progressively stiffen and begin to bear substantial load at large applied strains. In the second design, struts are replaced by a single sheet of elastomeric material. This design enables high energy absorbing capacity by exploiting the stiffer response of elastomers when loaded in biaxial tension relative to that in uniaxial tension.

3.4.2 Lattices with Curved Struts

The design of a lattice with curved struts is shown schematically in Fig. 3.8a. Its effectiveness was assessed using an extension of the analytical model presented in Section 3.3.3. Here the center-line of the curved strut is assumed to follow a trajectory defined by

$y = AL_t \sin^2(\pi x/L_t)$ where x and y are coordinates parallel and perpendicular to the line joining the two nodes, respectively, and A is a normalized amplitude, A/L_t . When the structure is initially compressed, only the straight struts stretch with a tensile force, F_{t1} ; the macroscopic response of the cell is then $F_a = (3\sqrt{3}/2)F_{t1} \tan \theta$. The curved struts are assumed to straighten without bearing load; only when straight do they begin to stretch and bear axial load. Once curved struts have straightened, the macroscopic applied force required to continue compressing the cell is augmented by the additional tensile force required to stretch the two initially-curved struts. The macroscopic applied force then becomes $F_a = 3\sqrt{3}/2(F_{t1} + 2F_{t2}) \tan \theta$ where F_{t2} is the tensile force required to stretch curved struts. The point at which curved struts are activated can be controlled by selecting the amplitude A ; when A is small, the struts straighten sooner and contribute to the macroscopic response at lower compressive strains. In principle the transition point could be tailored to coincide with the onset of geometric softening that would otherwise occur.

A rudimentary mechanics analysis demonstrates the potential of additional curved struts for tailoring the lattice stress-strain response. Analytical predictions of a structure having two curved struts between each node pair, with amplitude of $A=0.3$ or 0.5 , are plotted on Fig. 3.8b. (Details are in Appendix 3.C.) In both cases, the initial response (before straightening is complete) is the same as that of the baseline structure (with only straight struts). An abrupt jump in tangent modulus (once straightening is complete) occurs at strain of $\varepsilon = 0.08$ and 0.23 for $A=0.3$ and 0.5 , respectively. Hardening continues until a peak is attained, at strains

$\varepsilon = 0.28$ and 0.33 and stresses $\Phi_a = 0.46$ and 0.27 for $A = 0.3$ and 0.5 , respectively. By comparison, the critical values for the baseline structure are $\varepsilon = 0.24$ and $\Phi_a = 0.23$.

To further assess the curved-strut concept, test specimens with $\hat{A} = 0.3$ and $\hat{A} = 0.5$ were fabricated and tested, using materials and test methods described earlier (for the baseline lattice with only straight struts). Typical parts are pictured in Fig. 3.8c while the measured responses (upon loading) are in Fig. 3.8d for lattices both with and without curved struts. The full loading/unloading compression curves and strain maps are in Fig. 3.9.

Here the experimental stress-strain curves are in broad agreement with the analytical predictions with a few minor exceptions. With the addition of curved struts, the strain at peak stress increases somewhat while the peak stress increases by a significant amount. The peak stress ratios (relative to the original lattice) are approximately 1.9 and 1.2 for $\hat{A} = 0.3$ and $\hat{A} = 0.5$, respectively⁴. Upon closer inspection, the curves differ in a few subtle ways:

- (i) First, the initial stiffness is underestimated by the model, a consequence of neglecting the load carried by the curved struts as they straighten. The bending contributions are more apparent in the lattice with a small amplitude in the curved struts (Fig. 3.9a). The effects are also manifested in the measured strains in the curved struts as they straighten (Fig. 3.9c).
- (ii) Engagement of the curved struts occurs progressively and thus the tangent modulus does not exhibit an abrupt change at the point predicted by the model. Instead, the most apparent changes in tangent modulus are obtained at points where lock-up in the knuckle

⁴ As a cautionary note, interpretation of the stress elevations must take into consideration the fact that the volume of stretching material in the lattices with curved struts is more than 3 times that in the lattice with straight struts. More importantly, the intended goal of the curved strut design – to extend the hardening domain – is only moderately successful.

occurs during joint rotation. This is confirmed by rotation measurements plotted on Fig. 3.9e and 3.9f.

- (iii) The model predicts extensions of the hardening regime that are somewhat greater than those seen in the experiments. The differences are due to a combination of friction within the joints (which gives rise to an elevation in applied force during the forward loading cycle) and the lock-up of the joints at strains comparable to those near the predicted peak. While the lattice design and the corresponding model could be refined to account for the latter effects, the scope for such designs appears to be rather limited. Indeed, as we show next, a greater expansion of the design and property space is attainable using sheets in place of struts (straight or curved).

3.4.3 Preliminary Analysis of Sheet-based Designs

Elastomers are generally stiffer under biaxial tension than in uniaxial tension. The effects are illustrated in Fig. 3.10a. Here the responses of notional elastomers are computed using the Arruda-Boyce constitutive model²⁵. The key material parameter governing the biaxial/uniaxial stiffness is the limiting network stretch ratio, λ_L . The results on the figure cover the range $1 \leq \lambda_L \leq \infty$ (the latter representing Neo-Hookean behavior). Fig. 3.10a shows the stress-strain response while Fig. 3.10b shows the corresponding ratio of stress magnitudes. Elastomers with low values of λ_L show particularly large differences between biaxial and uniaxial tension. Fitting the tensile response of the elastomer used in this study yields a limiting stretch ratio, $\lambda_L = 1.6$. For this case the biaxial/uniaxial stress ratio ranges from 1.5 to 2.2 over the strain range of 0 to 1.

In the first sheet-based design, pictured in Fig. 3.11a, a triangular sheet with uniform thickness (2mm) is connected to the three midplane nodes. Intersections between the sheet and the nodes are filleted with a radius of 1mm. A preliminary assessment of the design was made using finite element simulations of the sheet and the three inner knuckles subject to equal in-plane displacements at the knuckle locations. For comparison, simulations were also performed on the strut-based design using the same volume of elastomeric material. Material properties and element types were the same as those described in Section 3.3.2. The model was meshed to yield an average element density of 14 elements/mm³ and 4-5 elements through the thickness of the sheet. The results shown in Fig. 3.12 are couched in terms of the local strain energy density \tilde{U} normalized by the Young's modulus E . The *magnitude* of \tilde{U}/E is used as a metric of the local efficacy of material use with respect to load-bearing capacity while the *distribution* of \tilde{U}/E addresses the efficacy of the overall design. Locations where \tilde{U}/E is particularly high are sites where failure might be expected to initiate. Results in Figs. 3.12a and b correspond to macroscopic compressive strains $\varepsilon = 0.25, 0.50, 0.75$. Histograms on the right side of the figure show the distributions of \tilde{U}/E at the last step ($\varepsilon = 0.75$).

In the strut design, \tilde{U}/E is mostly uniform within the struts, although some concentrations are evident near the nodes. In the sheet design, higher values of \tilde{U}/E are consistently localized near the nodes while lower values are located at the center of the sheet, indicating inefficient material use. On average \tilde{U}/E in the strut design (0.12) is lower than that in the sheet design (0.21), implying a softer response in the former. However, the distribution of \tilde{U}/E for the strut design is tighter with peak values about 60% lower than those in the sheet. This suggests that the strut design may be less prone to failure than the sheet design. While encouraging with respect to energy density and hence load-bearing capacity, the

analysis reveals weaknesses in the sheet design with respect to efficacy of material use and potential failure.

The deficiencies of the sheet design can be partly mitigated in two ways. The first is to add material to the node regions, to reduce the likelihood of failure there. The second is to move material within the sheet from regions of low \tilde{U}/E to regions of high \tilde{U}/E . To this end, in a second design iteration, the sheet thickness was graded from smallest at the center (1.4 mm) to largest at the nodes (3.4 mm) to improve the efficacy of material use and to mitigate failure initiation at the nodes. The volume of elastomeric material was kept constant. The results for the graded sheet design are plotted on Fig. 3.12c. In this case the graded design yields a tighter distribution of \tilde{U}/E and higher average value compared to those of the uniform sheet (0.23 vs 0.21). While modest, the improvements suggest that further design optimization is possible.

3.4.4 Implementation and Assessment of Sheet-based Designs

Lattices incorporating each of the two sheet designs were fabricated and tested in cyclic compression. In one set of tests the targeted strains in each loading cycle were 0.25, 0.50, and 0.75, and in a second set they were 0.25, 0.35 and 0.75. Pictures of the test specimens and results from both the compression tests and the FEA are presented in Fig. 3.11. To facilitate direct comparison with the strut-based lattice, loads are normalized by the volume of elastomeric material outside of the knuckles (i.e. material being stretched). Relative to the strut-based lattice, the sheet-based lattices exhibit a stiffer response at moderate strains and higher peak loads, by factors of 1.85 and 1.94 for lattices with uniform sheets and graded sheets, respectively. The ranking of the three on the basis of their respective peak loads is the

same as the ranking in their mean energy density at a macroscopic strain of 0.75: $\tilde{U} / E = 0.23$, 0.21, and 0.12 for the graded sheet, uniform sheet, and struts, respectively.

The behaviors of both sheet-based lattices differ qualitatively from those of the strut-based lattices in two respects. First, knuckle rotations in these cases are significantly lower, as evidenced by the results in Figs. 3.11e and f, and lock-up does not occur. Consequently, the abrupt rise in tangent modulus otherwise obtained following lock-up is absent. Evidently the higher loads transmitted through the sheets to the joints stabilize knuckle rotation and prevent lock-up from occurring.

Second, while the strut-based lattices were successfully loaded cyclically to densification (to a strain of about 0.70) and recovered to their original state upon unloading, the sheet-based lattices ruptured before the completion of loading. Rupture occurred in the uniform-sheet lattice either during unloading in the second cycle or upon loading in the third cycle; rupture of the graded-sheet lattice was delayed somewhat, in one case occurring during unloading from the third cycle. Rupture consistently initiated near one of the midplane nodes, either at the root of the fillet (in the uniform-sheet, Fig. 3.13c) or at the bi-material interface (in the graded-sheet, Fig. 3.13d). Initial tears quickly spread to the outer edges of the sheet separating the knuckle from the sheet.

The propensity for rupture in both strut-based and sheet-based lattices can be understood in terms of computed strain energy density distributions (Fig. 3.12). The tail of this distribution (at high values of \tilde{U} / E) extends furthest in the uniform-sheet lattice; it is somewhat shorter for the graded sheets and shorter yet for the strut-based lattice. The trends in these distributions (in the histograms) along with the evident locations of the “hot spots” (in the contour plots) are in accord with both the rankings in terms of ductility and the locations

of rupture initiation. The results suggest the possibility that design optimizations could be used to identify geometric configurations of the elastomeric material that produce a high mean value of \tilde{U}/E along with a narrow distribution in \tilde{U}/E , thereby yielding lattice designs with high strength and high ductility.

3.4.5 Tiling Concepts

In principle the bi-material lattice concepts can be expanded to larger multi-cell structures. This would entail tiling of unit cells (of the type used here) between pairs of face sheets. One potential design and its response are shown in the video in Supplementary Information. Here the cells are arranged on a periodic triangulated lattice that reflects the symmetry of the initial (triangular) cell shape. The cells are oriented so that the transverse struts of neighboring cells are parallel to one another and are spaced so that struts within one cell do not make contact with those in neighboring cells even at full densification. With this configuration the structure exhibits a plastic Poisson's ratio of zero. That is, uniaxial compressive stressing is accommodated entirely by uniaxial straining. With current multi-material additive manufacturing technologies, such structures could be made in a single print operation.

3.5 Conclusions

The current study has explored several 3D bi-material lattice concepts for tailoring compressive stress-strain response. Assessments have been made on the basis of analytical models, finite element simulations, and instrumented mechanical tests on fabricated lattices. The key conclusions follow.

1. Bi-material lattices with the baseline strut design exhibit stress-strain characteristics that are consistent with those predicted by the models, including hardening and stable softening domains. The two domains are manifestations of the competition between the progressive reduction in inclination angle of the compressive struts (leading to softening) and the increasing loads carried by the stretching struts (leading to hardening). Secondary effects of lock-up within the knuckles are manifested in somewhat abrupt but transient changes in both the tangent modulus and the direction of knuckle rotation. The strut-based lattices show strain reversibility even after compression to nearly-complete lattice densification.
2. The lattice response can be tailored by adding curved struts between node pairs. The loads carried by these struts are initially small (while the struts are straightening). Beyond a critical point, dictated by strut curvature, the curved struts begin to contribute significantly to the forces between node pairs. Elevations in peak stress and (to a lesser extent) strain at peak stress have been demonstrated.
3. Sheet-based designs provide an even more effective way to increase load-bearing capacity of bi-material lattices. The designs exploit the higher stiffness of elastomers in biaxial tension (by a factor of about 2) relative to that in uniaxial tension.
4. The graded sheet design produces a slightly higher peak stress relative to that with the uniform sheet while also yielding greater straining capacity prior to rupture. These trends are consistent with the computed strain energy density distributions. The results suggest that sheet-based lattices may be amenable to design optimization, with the ultimate goal of identifying the most efficient distribution of material to maximize stiffness and strength while also mitigating rupture.

3.A Appendix: Deformation and Failure Analysis of Lattices with Straight Struts

3.A1 Primitive Structural Motif

The following analysis of the structural response of the primitive motif is based on an energy method. When the structure is compressed, the work U_w done by the applied force F_a is equal to the elastic energy U_e in the transverse strut. The work done is $U_w = \int_0^v F_a(v') dv'$ where v is the axial displacement and the prime denotes a dummy variable. The height of the structure is reduced from H_0 to $H = H_0 - v$. The displacement v is accommodated by rotation of the inclined struts from an initial angle θ_0 to θ and elongation of the transverse struts from a length W_0 to $W = W_0 + u$. The elastic energy in the three transverse struts is

$$U_e = 3 \int_0^u F_t(u') du' = 3 \int_0^u \frac{2E_t A_t u' \tan \theta_0}{\sqrt{3} H_0} du' \quad (3.A1)$$

where F_t is the force in each transverse strut. Setting $U_e = U_w$, the force-displacement relation $F_a(v)$ is found to be

$$F_a(v) = \frac{6E_t A_t \tan \theta_0}{\sqrt{3} H_0} \frac{u(v)}{dv} \quad (3.A2)$$

From geometry,

$$u(v)/H_0 = \frac{\sqrt{3}}{2} \left[\left(\csc^2 \theta_0 - (1 - \varepsilon_a)^2 \right)^{1/2} - \cot \theta_0 \right] \quad (3.A3)$$

$$du(v)/dv = \frac{\sqrt{3}}{2} \left[(1 - \varepsilon_a) \left(\csc^2 \theta_0 - (1 - \varepsilon_a)^2 \right)^{-1/2} \right] \quad (3.A4)$$

where ε_a is the macroscopic applied strain defined by $\varepsilon_a = v/H_0$. Combining the preceding equations yields

$$\Phi_a \equiv \frac{F_a}{3E_t A_t} = \frac{\sqrt{3}}{2} (1 - \varepsilon_a) \left[\tan \theta_0 - \left(\csc^2 \theta_0 - (1 - \varepsilon_a)^2 \right)^{-1/2} \right] \quad (3.A5)$$

This is equivalent to Eqn. 3.1 in the text.

The corresponding tensile strain ε_t in the transverse struts is

$$\varepsilon_t = \tan \theta_0 \left[\csc^2 \theta_0 - (1 - \varepsilon_a)^2 \right]^{1/2} - 1 \quad (3.A6)$$

while the compressive force F_c within the inclined struts, expressed in the non-dimensional form $\Phi_c \equiv F_c / 3E_t A_t$, is:

$$\Phi_c = \frac{\sqrt{3}}{6} \left[\sec \theta_0 - \left(1 - \sin^2 \theta_0 (1 - \varepsilon_a)^2 \right)^{-1/2} \right] \quad (3.A7)$$

The maximum values of ε_t and Φ_c are obtained at $\varepsilon_a = 1$; they are $\varepsilon_t^{\max} = \sec \theta_0 - 1$ (from Eqn. 3.A6) and $\Phi_c^{\max} = \sqrt{3}(\sec \theta_0 - 1)/6$ (from Eqn. 3.A7). (Full densification, *i.e.* $\varepsilon_a = 1$, can be attained because of the assumed infinitesimal thicknesses of struts and nodes.)

Attaining full densification requires that the transverse strut material have sufficiently high tensile ductility: $\varepsilon_t^* > \varepsilon_t^{\max} = \sec \theta_0 - 1$ (from Eqn. 3.A6, with $\varepsilon_a = 1$). Tensile rupture is therefore avoided when the initial inclination angle is below a critical value, $\theta_0^* = \sec^{-1}(1 + \varepsilon_t^*)$. Otherwise, when $\theta_0 > \theta_0^*$, tensile rupture precedes densification and, from Eqn. 3.A6, occurs at an applied strain of

$$\varepsilon_a^* = 1 - \csc \theta_0 \left[1 - \cos^2 \theta_0 (1 + \varepsilon_t^*)^2 \right]^{1/2} \quad (3.A8)$$

Attaining full densification also requires that the inclined struts do not buckle or yield. The critical strut buckling force is $\Phi_c^{buc} \equiv F_c^{buc} / 3E_t A_t$ where $F_c^{buc} = \pi^2 E_c A_c t_c^2 / 12K^2 L_c^2$ (the Euler buckling force), E_c is the Young's modulus of the inclined strut, A_c , t_c and L_c are strut cross

sectional area, thickness and length, respectively, and K is the effective length parameter. Combining these results yields a buckling force of $\Phi_c^{buc} = \Gamma$ where Γ is a non-dimensional buckling parameter defined by $\Gamma \equiv \pi^2 E_c A_c t_c^2 / 36 E_t A_t L_c^2 K^2$. Buckling is avoided when $\Phi_c^{\max} < \Phi_c^{buc}$ or, equivalently, $\theta_0 < \theta_0^{buc} = \sec^{-1}(2\Gamma\sqrt{3}+1)$. Analogously, the critical strut yielding force is $\Phi_c^{yield} \equiv F_c^{yield} / 3E_t A_t$ where $F_c^{yield} = \sigma_y A_c$ and σ_y is the yield stress of the compressive strut material. Combining these results produces a yielding force of $\Phi_c^{yield} = \Lambda$ where Λ is a non-dimensional yielding parameter defined by $\Lambda \equiv \sigma_y A_c / 3E_t A_t$. Yielding is avoided when $\Phi_c^{\max} < \Phi_c^{yield}$ or, equivalently, when $\theta_0 < \theta_0^{yield} = \sec^{-1}(2\Lambda\sqrt{3}+1)$.

3.A2. FiniteLattice Structures

Incorporating finite node dimensions into the analysis, the predicted macroscopic response is given by

$$F_a(v) = \frac{6E_t A_t \tan \theta_0 u(v)}{\alpha_t \sqrt{3} H_0} \frac{du(v)}{dv} \quad (3.A9)$$

This differs from Eqn. 3.A2 with the addition of α_t , the non-dimensional transverse strut length: $\alpha_t \equiv L_t^{eff} / L_t$. From geometry, $u(v)/H_0$ and $du(v)/dv$ are modified to yield:

$$u(v)/H_0 = \frac{\alpha_c \sqrt{3}}{2} \left[\left(\csc^2 \theta_0 - \left(1 - \frac{\varepsilon_a}{\alpha_c} \right)^2 \right)^{1/2} - \cot \theta_0 \right] \quad (3.A10)$$

$$du(v)/dv = \frac{\sqrt{3}}{2} \left[\left(1 - \frac{\varepsilon_a}{\alpha_c} \right) \left(\csc^2 \theta_0 - \left(1 - \frac{\varepsilon_a}{\alpha_c} \right)^2 \right)^{-1/2} \right] \quad (3.A11)$$

where α_c is the non-dimensional inclined strut length $\alpha_c \equiv L_c^{eff} / L_c$. Substituting Eqs. 3.A10 and 3.A11 into 3.A9 yields Eqn. 3.2 in the text.

Here the inclination angle, the transverse strut strain, and the compressive stress in inclined struts are:

$$\theta = \sin^{-1} \left[\sin \theta_0 (1 - \varepsilon_a / \alpha_c) \right] \quad (3.A12)$$

$$\varepsilon_t = \frac{\alpha_c}{\alpha_t} \left[\tan \theta_0 \left(\csc^2 \theta_0 - (1 - \varepsilon_a / \alpha_c)^2 \right)^{1/2} - 1 \right] \quad (3.A13)$$

$$\Phi_c = \frac{\alpha_c \sqrt{3}}{6\alpha_t} \left[\sec \theta_0 - \left(1 - \sin^2 \theta_0 \left(1 - \frac{\varepsilon_a}{\alpha_c} \right)^2 \right)^{-1/2} \right] \quad (3.A14)$$

Densification is assumed to occur when the initially inclined struts are horizontal and thus the inclination angle is $\theta = 0^\circ$. The densification strain (from Eqn. 3.A12) is therefore $\varepsilon_a^{den} = \alpha_c$.

The maximum values of ε_t and Φ_c are obtained at $\varepsilon_a = \varepsilon_a^{den} = \alpha_c$ and are given by

$$\varepsilon_t^{\max} = \frac{\alpha_c (\sec \theta_0 - 1)}{\alpha_t} \quad (3.A15)$$

$$\Phi_c^{\max} = \frac{\alpha_c \sqrt{3} (\sec \theta_0 - 1)}{6\alpha_t} \quad (3.A16)$$

Tensile rupture is avoided when $\varepsilon_t^* > \varepsilon_t^{\max}$. This condition is satisfied when the initial inclination angle is below a critical value, $\theta_0^* = \sec^{-1} \left(1 + \varepsilon_t^* \alpha_t / \alpha_c \right)$ (from Eqn. 3.A13). Similarly, buckling is avoided when $\Phi_c^{\max} < \Phi_c^{buc} = F_a^{buc} / 3E_t A_t = \Gamma / \alpha_c^2$ or, equivalently,

$\theta_0 < \theta_0^{buc} \equiv \sec^{-1}\left(1 + 2\Gamma\alpha_t\sqrt{3}/\alpha_c^3\right)$ (from Eqn. 3.A12). Lastly, yielding is avoided when $\Sigma_c^{\max} < \Sigma_c^{yield} = F_a^{yield} / 3E_t A_t = \Lambda$ or, equivalently, $\theta_0 < \theta_0^{yield} \equiv \sec^{-1}\left(1 + 2\Lambda\sqrt{3}\alpha_t/\alpha_c\right)$.

3.B Appendix: Arruda-Boyce Hyperelastic Constitutive Law

Assuming incompressibility, the uniaxial tensile stress-strain response $\sigma_t(\varepsilon_t)$ from the Arruda-Boyce hyperelastic constitutive law is given by ²⁵:

$$\sigma_t = 2C_1 \left(1 + \varepsilon_t - \frac{1}{(1 + \varepsilon_t)^2}\right) \left[\sum_{i=1}^5 i\alpha_i \left(\frac{1}{\lambda_L^2}\right)^{i-1} I_1^{i-1} \right] \quad (3.B1)$$

where C_1 is a material constant, α_i is the i^{th} term in the inverse Langevin function, $a_i = \{1/2, 1/20, 11/1050, 19/7000, 519/673750\}$, λ_L is the limiting network stretch and I_1 is the first invariant of the right Cauchy-Green tensor ($I_1 = (1 + \varepsilon_t)^2 + 2/(1 + \varepsilon_t)$). The incompressibility assumption is supported by the transverse and longitudinal strains measured in the tensile tests (Fig. 3.4c). The shear modulus is $G = C_1\Omega$ where

$$\Omega = 1 + \frac{3}{5\lambda_L^2} + \frac{99}{175\lambda_L^4} + \frac{513}{875\lambda_L^6} + \frac{42039}{67375\lambda_L^8} \quad (3.B2)$$

Fitting the measured stress-strain curves to Eqn. 3.B1 yields the parameters $C_1 = 0.12$ MPa, $\lambda_L = 1.59$ and $G = 0.17$ MPa.

3.C Appendix: Analysis of Lattices with Curved Struts

3.C1 Primitive Structural Motif

The energy method described in Appendix 3.A is used to analyze the response of a unit cell having curved struts. This model accounts for finite node size and uses a linear elastic constitutive model. When the unit cell is compressed, the total energy stored in straight and curved struts is $U_e = 3U_{e1} + 6U_{e2}$ where U_{e1} is the elastic energy stored in the straight struts and U_{e2} is the energy stored in the curved struts. (The numerical coefficients capture the 3 straight struts and 6 curved struts in the design.) The first energy term is:

$$U_{e1} = \int_0^u F_t(u') du' = \int_0^u \frac{2E_t A_t u' \tan \theta_0}{\sqrt{3}H_0} du' \quad (3.C1)$$

Curved struts are assumed to carry zero load until they have fully straightened. The energy stored in these struts is given by:

$$U_{e2} = 0 \quad , u < u_{st}$$

$$U_{e2} = \int_0^u F_t(u') du' = \int_0^u \frac{2E_t A_t (u' - u_{st}) \tan \theta_{st}}{\sqrt{3}H_0} du' \quad , u \geq u_{st} \quad (3.C2)$$

where u_{st} is the lateral displacement between midplane nodal locations required for the curved struts to fully straighten. Eq. 3.C2 differs from Eq. 3.C1 in that the transverse displacement u is replaced by $u - u_{st}$ and the initial inclination angle, θ_0 , is replaced by the angle at which curved struts have fully straightened, θ_{st} . The transverse displacement and inclination angle at which curved struts straighten are given by:

$$u_{st} / H_0 = \frac{\sqrt{3} \cot \theta_0}{2} (S - 1) \quad (3.C3)$$

$$\theta_{st} = \sin^{-1} \left[\sqrt{1 - S^2 \cos^2 \theta_0^2} \right] \quad (3.C4)$$

where S is the normalized length of the curved strut (S/L_t) given by

$$S = \int_0^1 \sqrt{1 + (A\pi)^2 \sin^2(2\pi x)} dx = \frac{2}{\pi} \text{EllipticE} \left[-A^2 \pi^2 \right].$$

Setting the total elastic energy, U_e ,

equal to the work done, $U_w = \int_0^v F_a(v) dv$, the normalized response of a unit cell having curved

struts is

$$\begin{aligned} \frac{F_a(v)}{3E_t A_t} &= \frac{2}{\sqrt{3}} \left(\tan \theta_0 \frac{u(v)}{H_0} \frac{du(v)}{dv} \right) \quad , u < u_{st} \\ \frac{F_a(v)}{3E_t A_t} &= \frac{2}{\sqrt{3}} \left(\tan \theta_0 \frac{u(v)}{H_0} + \tan \theta_{st} \frac{2(u(v) - u_{st})}{H_0} \right) \frac{du(v)}{dv} \quad , u \geq u_{st} \end{aligned} \quad (3.C5)$$

where $\frac{u(v)}{H_0}$ and $\frac{du(v)}{dv}$ are given by Eqns. 3.A3 and 3.A4.

3.C2. Finite Lattice Structures

Incorporating finite node dimensions into the analysis, the macroscopic response becomes:

$$\begin{aligned} \frac{F_a(v)}{3E_t A_t} &= \frac{2}{\alpha_t \sqrt{3}} \left(\tan \theta_0 \frac{u(v)}{H_0} \frac{du(v)}{dv} \right) \quad , u < u_{st} \\ \frac{F_a(v)}{3E_t A_t} &= \frac{2}{\alpha_t \sqrt{3}} \left(\tan \theta_0 \frac{u(v)}{H_0} + \tan \theta_{st} \frac{2(u(v) - u_{st})}{H_0} \right) \frac{du(v)}{dv} \quad , u \geq u_{st} \end{aligned} \quad (3.C6)$$

Here, $\frac{u(v)}{H_0}$ and $\frac{du(v)}{dv}$ are given by Eqns. 3.A10 and 3.A11. The transverse displacement and

inclination angle at which curved struts straighten are modified accordingly:

$$u_{st} / H_0 = \frac{\alpha_t \sqrt{3} \cot \theta_0}{2} (S - 1) \quad (3.C7)$$

$$\theta_{st} = \sin^{-1} \left[\sqrt{1 - \left(1 + \frac{\alpha_t}{\alpha_c} S - \frac{1}{\alpha_c} \right)^2 \cos^2 \theta_0} \right] \quad (3.C8)$$

References

1. Zok, F. W. Integrating lattice materials science into the traditional processing-structure-properties paradigm. *MRS Commun.* 9, 1284–1291 (2019).
2. Chen, D. & Zheng, X. Multi-material Additive Manufacturing of Metamaterials with Giant, Tailorable Negative Poisson's Ratios. *Sci. Rep.* 8, 1–8 (2018).
3. Janbaz, S., Bobbert, F. S. L., Mirzaali, M. J. & Zadpoor, A. A. Ultra-programmable buckling-driven soft cellular mechanisms. *Mater. Horizons* 6, 1138–1147 (2019).
4. Zhang, H., Guo, X., Wu, J., Fang, D. & Zhang, Y. Soft mechanical metamaterials with unusual swelling behavior and tunable stress-strain curves. 4, (2018).
5. Wehmeyer, S. C., Compton, B. G., Pro, J. W., Zok, F. W. & Begley, M. R. Damping in cellular structures made from composite struts and walls with elastic and viscoelastic phases. *J. Mech. Phys. Solids J. homepage* 145, 104106 (2020).
6. Ruschel, A. L. & Zok, F. W. A bi-material concept for periodic dissipative lattices. *J. Mech. Phys. Solids* 145, 104144 (2020).
7. Mirzaali, M. J., Caracciolo, A. & Pahlavani, H. Multi-material 3D printed mechanical metamaterials: Rational design of elastic properties through spatial distribution of hard and soft phases. *Appl. Phys. Lett* 113, 241903 (2018).
8. Wang, K., Chang, Y. H., Chen, Y. W., Zhang, C. & Wang, B. Designable dual-material auxetic metamaterials using three-dimensional printing. *Mater. Des.* 67, 159–164 (2015).
9. Lumpe, T. S. & Shea, K. Computational design of 3D-printed active lattice structures

- for reversible shape morphing. *J. Mater. Res.* 2021 36, 3642–3655 (2021).
10. Kazemi, H., Vaziri, A. & Norato, J. A. Multi-material topology optimization of lattice structures using geometry projection. *Comput. Methods Appl. Mech. Eng.* 363, (2020).
 11. Stankovic, T., Mueller, J., Egan, P. & Shea, K. A Generalized Optimality Criteria Method for Optimization of Additively Manufactured Multimaterial Lattice Structures. *J. Mech. Des.* 137, (2015).
 12. Yavas, D., Liu, Q., Zhang, Z. & Wu, D. Design and fabrication of architected multi-material lattices with tunable stiffness, strength, and energy absorption. *Mater. Des.* 217, 110613 (2022).
 13. Mueller, J., Raney, J. R., Shea, K. & Lewis, J. A. Architected Lattices with High Stiffness and Toughness via Multicore–Shell 3D Printing. *Adv. Mater.* 30, 1705001 (2018).
 14. Mueller, J., Lewis, J. A. & Bertoldi, K. Architected Multimaterial Lattices with Thermally Programmable Mechanical Response. *Adv. Funct. Mater.* 32, 2105128 (2021).
 15. Yuan, C. *et al.* Thermomechanically Triggered Two-Stage Pattern Switching of 2D Lattices for Adaptive Structures. *Adv. Funct. Mater.* 28, 1705727 (2018).
 16. Zhao, Z. *et al.* Three-Dimensionally Printed Mechanical Metamaterials with Thermally Tunable Auxetic Behavior. *Phys. Rev. Appl.* 11, 044074 (2019).
 17. Hammett, C. I., Rinaldi, R. G. & Zok, F. W. Pyramidal Lattice Structures for High Strength and Energy Absorption. *J. Appl. Mech.* 80, (2013).

18. Latture, R. M., Rodriguez, R. X., Holmes, L. R. & Zok, F. W. Effects of Nodal Fillets and External Boundaries on Compressive Response of an Octet Truss. *Acta Mater.* 149, 78–87 (2017).
19. Meza, L. R. *et al.* Reexamining the mechanical property space of three-dimensional lattice architectures. *Acta Mater.* 140, 424–432 (2017).
20. Zorzetto, L. *et al.* Properties and role of interfaces in multimaterial 3D printed composites. *Sci. Rep.* 10, 1–17 (2020).
21. Sophia Fox, A. J., Bedi, A. & Rodeo, S. A. The basic science of articular cartilage: Structure, composition, and function. *Sports Health* 1, 461–468 (2009).
22. Rajan, V. P., Rossol, M. N. & Zok, F. W. Optimization of Digital Image Correlation for High-Resolution Strain Mapping of Ceramic Composites. *Exp. Mech.* 52, 1407–1421 (2012).
23. Reu, P. All about Speckles: Aliasing. *Exp. Tech.* 38, 1–3 (2014).
24. Shooter, K. V. & Tabor, D. The Frictional Properties of Plastics. *Proc. Phys. Soc.* 65, Section B, 661 (1952).
25. Arruda, E. M. & Boyce, M. C. A three-dimensional constitutive model for the large stretch behavior of rubber elastic materials. *J. Mech. Phys. Solids* 41, 389–412 (1993).

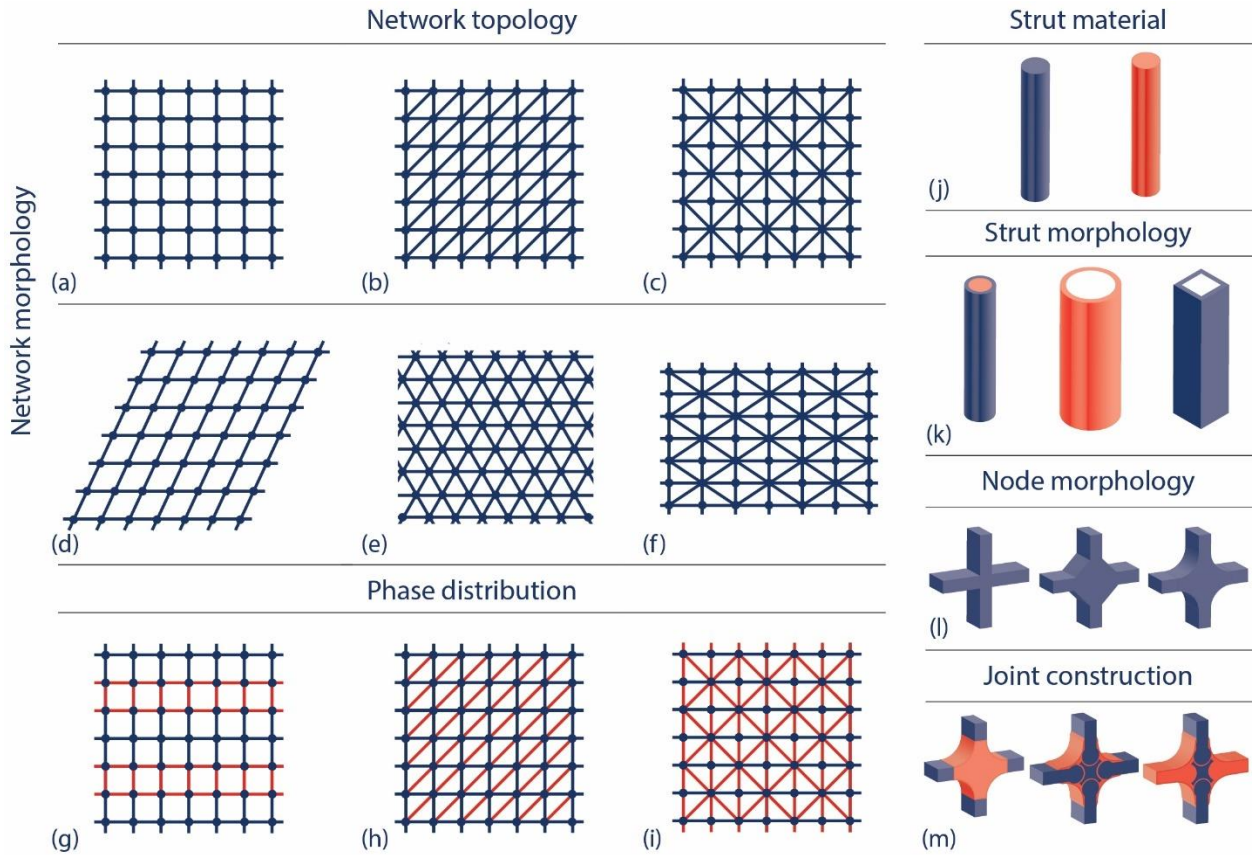


Figure 3.1: Incorporating multiple materials into lattice design extends lattice characteristics beyond those applicable to single-material designs (a-f and l) to include new definitions of characteristics (j and k) as well as new characteristics (g-i and m).

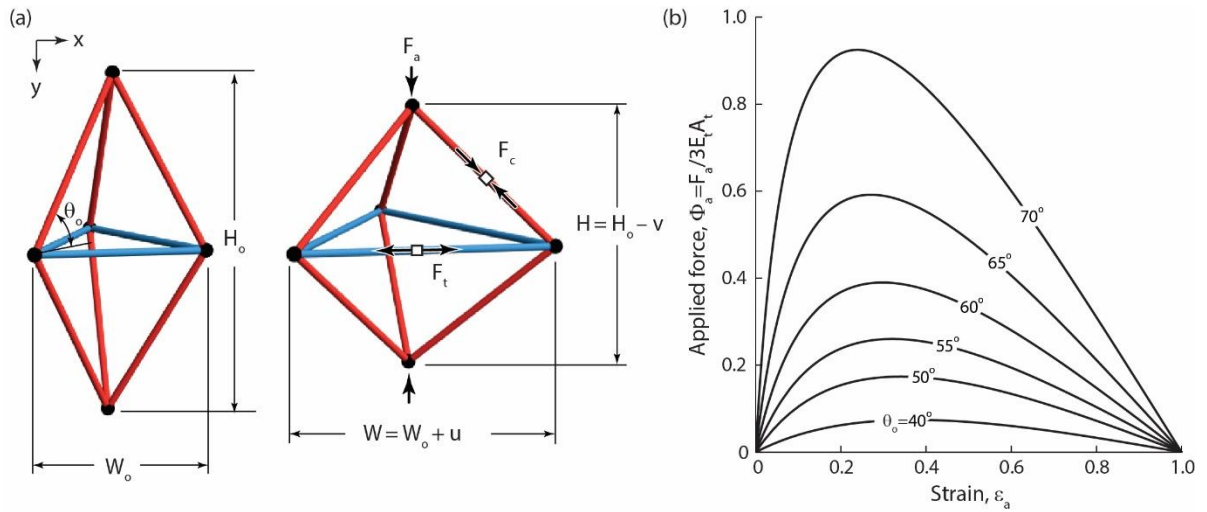


Figure 3.2: (a) The primitive bi-material structural motif is composed of stiff struts (red) and compliant, extensible struts (blue) connected by pin joints. When the cell is compressed, inclined struts rotate to accommodate stretching of transverse struts. (b) The compressive response of the primitive motif is strongly influenced by the initial strut inclination angle.

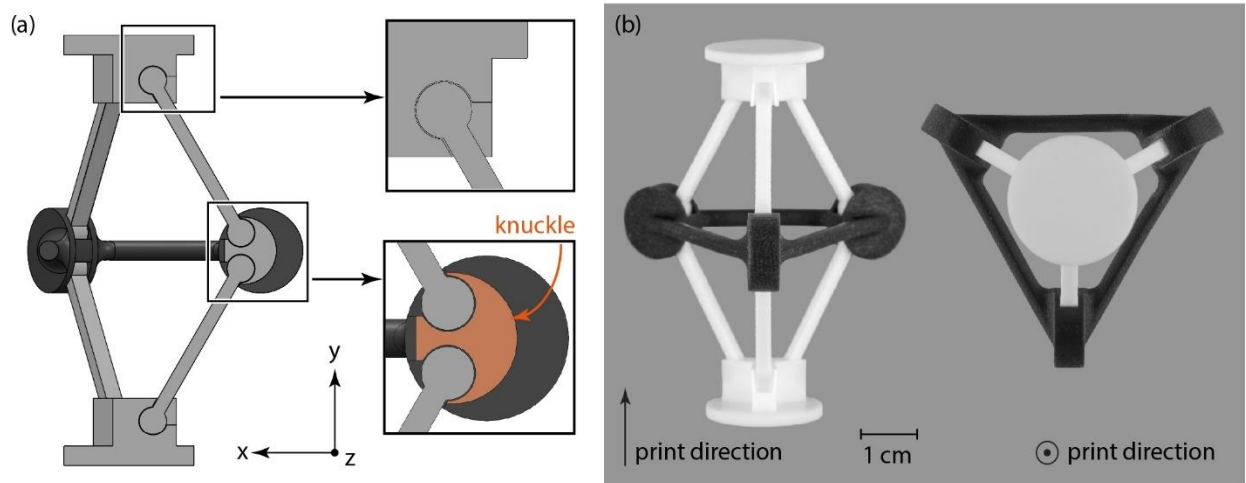


Figure 3.3: Concept implementation: (a) A cutaway shows one third of the structure as well as the knob-and-socket joint design. (b) The entire structure, including the interlocked parts in the joint, are made in a single print operation.

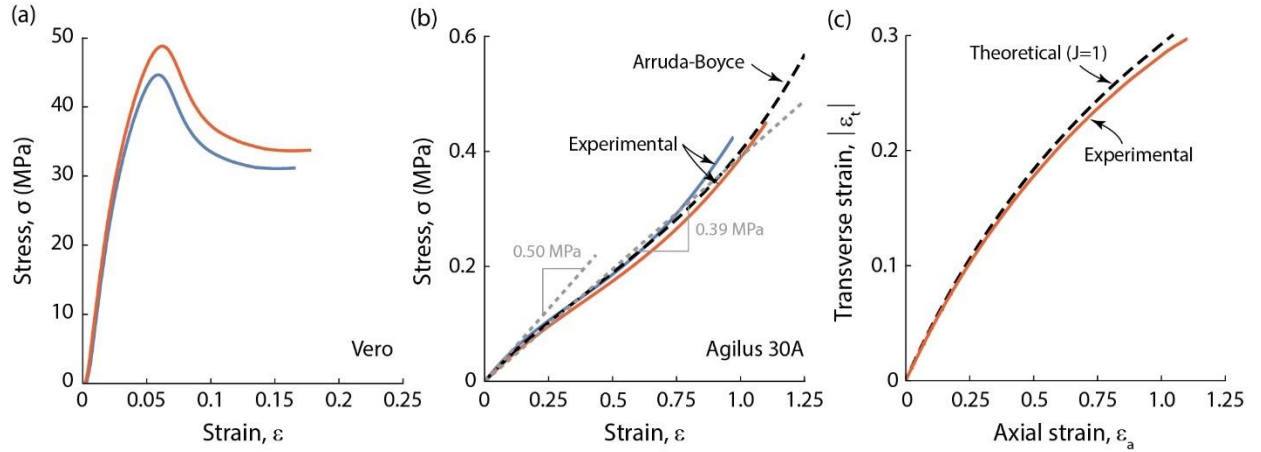


Figure 3.4: Stress-strain curves of (a) acrylic-like material and (b) elastomeric material obtained from tensile tests. The results in (b) were used to calibrate the hyperelastic constitutive law. The grey dashed lines in (b) indicate the true (small-strain) elastic modulus and an effective modulus over the strain range 0 to 1. The latter is the pertinent modulus for use with the analytical model. (c) Measurements of in-plane strains in the elastomer support the incompressibility assumption.

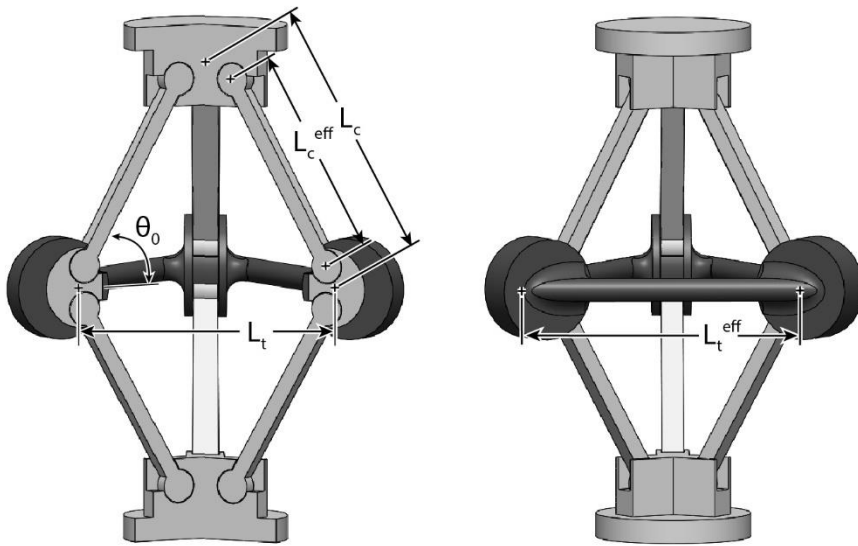


Figure 3.5: Finite node sizes in the bi-material structure reduce the effective strut lengths, from L_t to L_t^{eff} and L_c to L_c^{eff} . (Pertinent dimensions are: $L_t = 32.6\text{mm}$, $L_t^{eff} = 32.3\text{mm}$, $L_c = 33.8\text{mm}$, $L_c^{eff} = 27\text{mm}$, and $\theta_0 = 60^\circ$.)

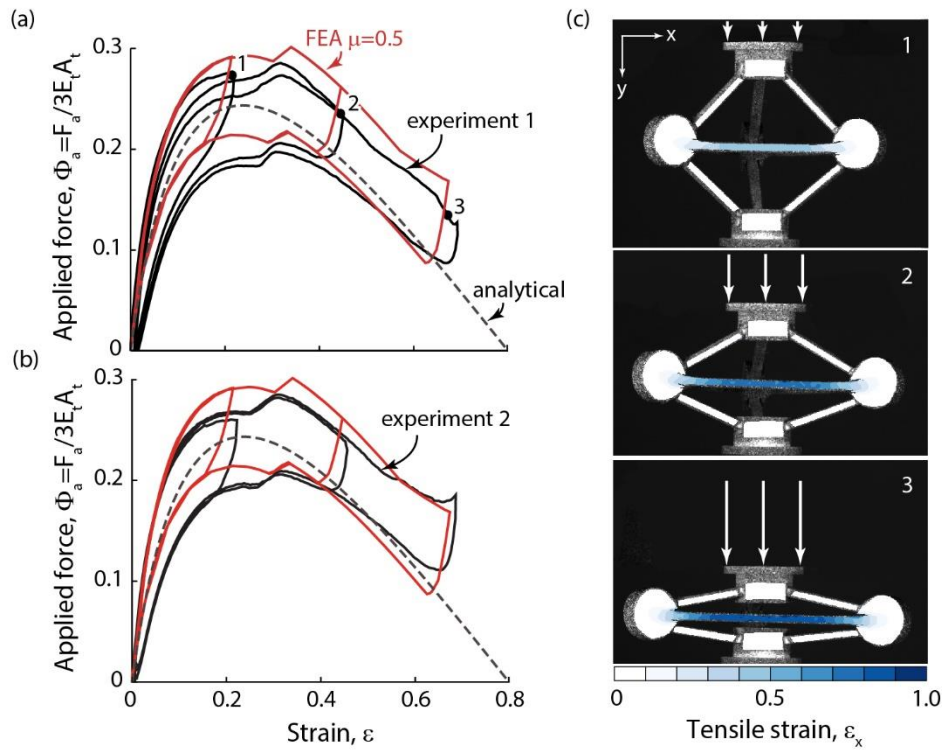


Figure 3.6: (a, b) Stable and reversible compressive response of the bi-material lattice. Also shown are the results from the analytical model and the FE simulations. Since the analytical model is based on a modulus that represents the response of the elastomer over the entire strain range of interest (roughly 0 to 1) – *not* the true small-strain modulus – the results for the analytical model are normalized accordingly, *i.e.* scaled by the ratio of the effective modulus to the real modulus (indicated by the grey lines in Fig. 3.4(b)). The scaling factor is about 0.78. The same normalizations are employed in the analytical model predictions in Figs. 3.8 (b) and 3.9 (a, b). (c) Strain maps at select points during compressive loading show that macroscopic straining is accommodated by stretching of the transverse struts and rotation of the inclined struts.

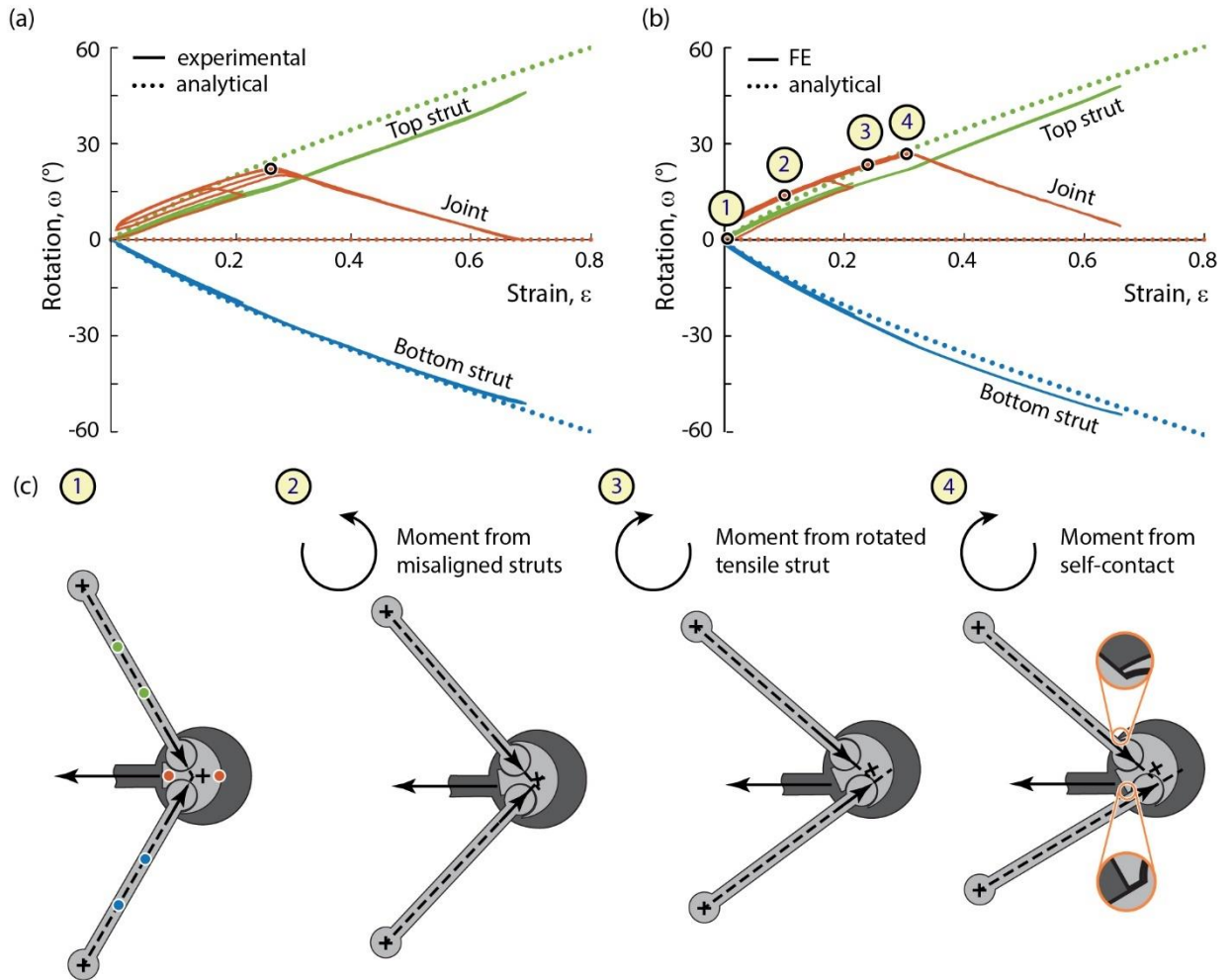


Figure 3.7: (a) Measured rotations of inclined struts (solid orange and blue lines) are represented well by the analytical model (dotted orange and blue lines). In contrast, measured joint rotations (solid green lines) differ from the predictions (dotted horizontal green line). (b) The FEA simulations capture both the strut and the joint rotations. (c) Schematics show changes in geometry and forces that lead to the moments which in turn cause joint rotation. The direction of rotation reverses once contact is made between the edges of the knuckle and the strut surfaces (at point 4).

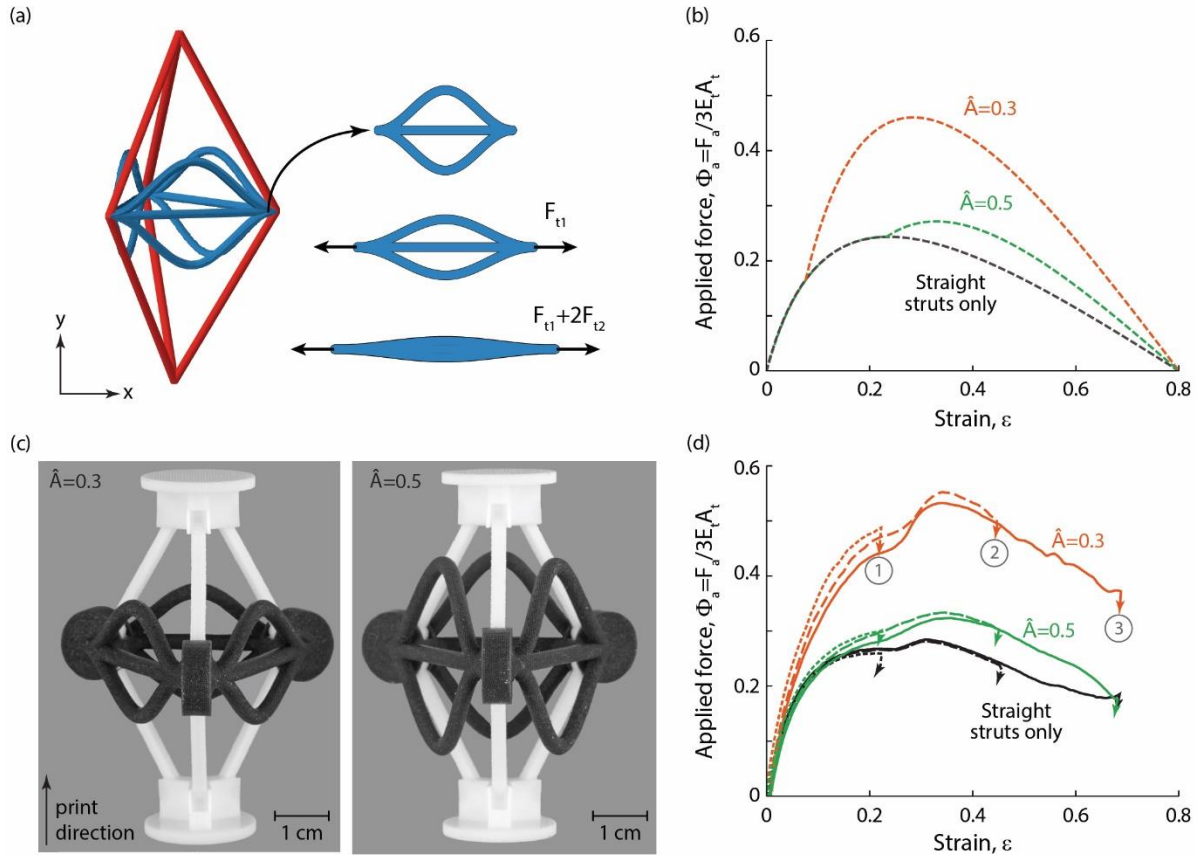


Figure 3.8: (a) The bi-material lattice is modified to include curved struts that initially straighten before stretching. (b) Analytical model predictions show effects of amplitude of curved struts in the post-straightening domain. (c) Two types of bi-material lattices were printed, distinguished by amplitude of curved struts. (d) Compressive responses of lattices with and without curved struts. For clarity the unloading loops (presented in Fig. 3.9a,b) have been removed. Circled numbers denote cycle numbers.

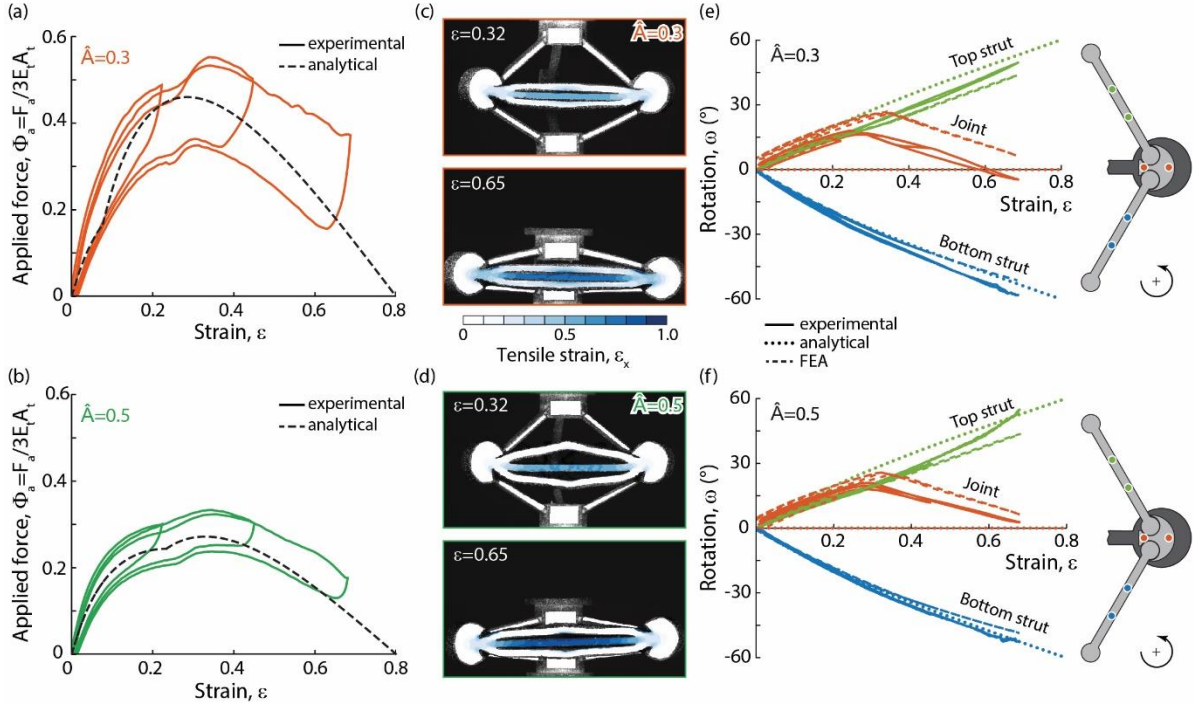


Figure 3.9: (a, b) Macroscopic responses of bi-material lattices having curved struts are compared to analytical predictions. (c, d) Strain maps at select points during deformation show that macroscopic straining is accommodated by stretching of the straight struts from the outset as well as straightening and subsequent stretching of the curved struts. (e, f) Pairs of compressive (inclined) struts rotate symmetrically about the central plane, as predicted by the analytical model and the FEA. Joint rotation, on the other hand, follows a more complex trajectory, including a critical point at which the direction of rotation reverses.

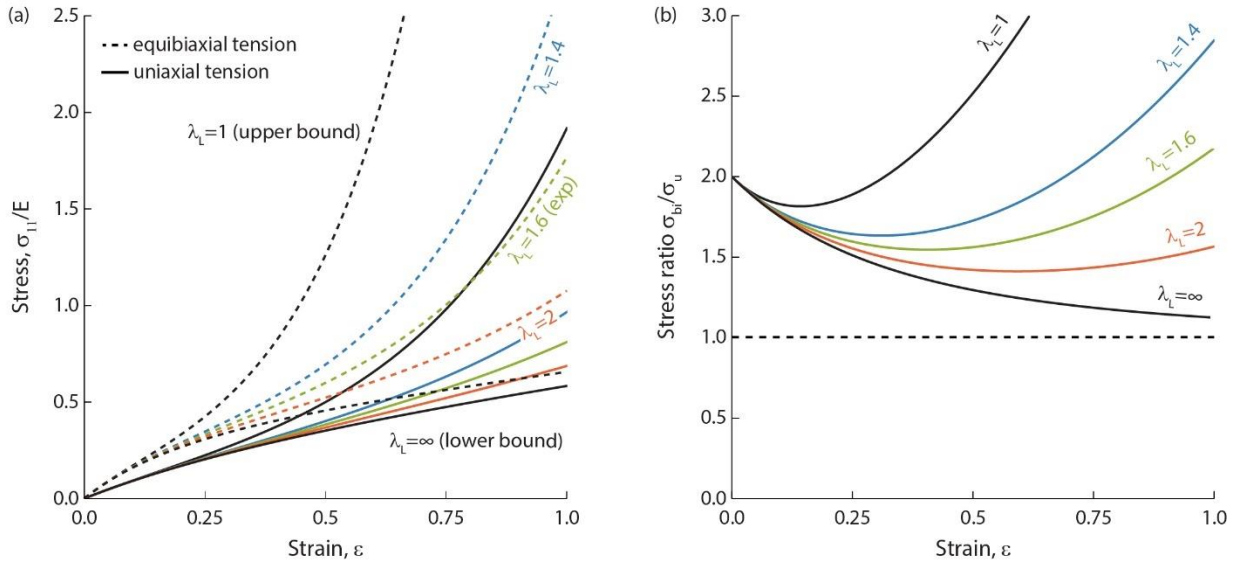


Figure 3.10: (a) Stress-strain responses of Arruda-Boyce elastomers (having different limiting stretches) show the potential increases in stress that can be attained when loading an elastomer in uniaxial and equibiaxial tension. (b) Elastomers having low limiting stretches have the most drastic stress increases in stress when loaded in equibiaxial tension vs uniaxial tension.

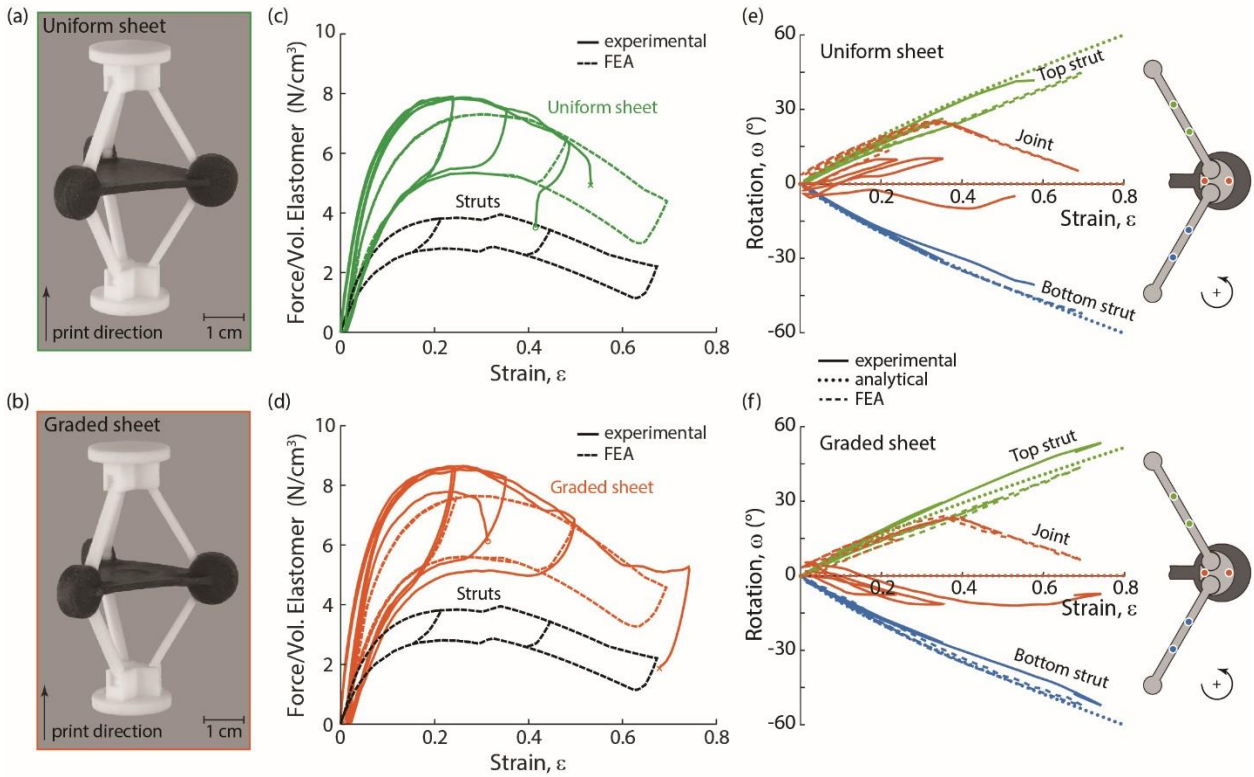


Figure 3.11: (a, b) Photographs of lattices with the two different sheet designs. Experimental and FE results of (c, d) stress-strain response and (e, f) strut and joint rotations. Sheet rupture in (c, d) is indicated by an “o” or an “x”. Results are shown for two tests on each lattice design.

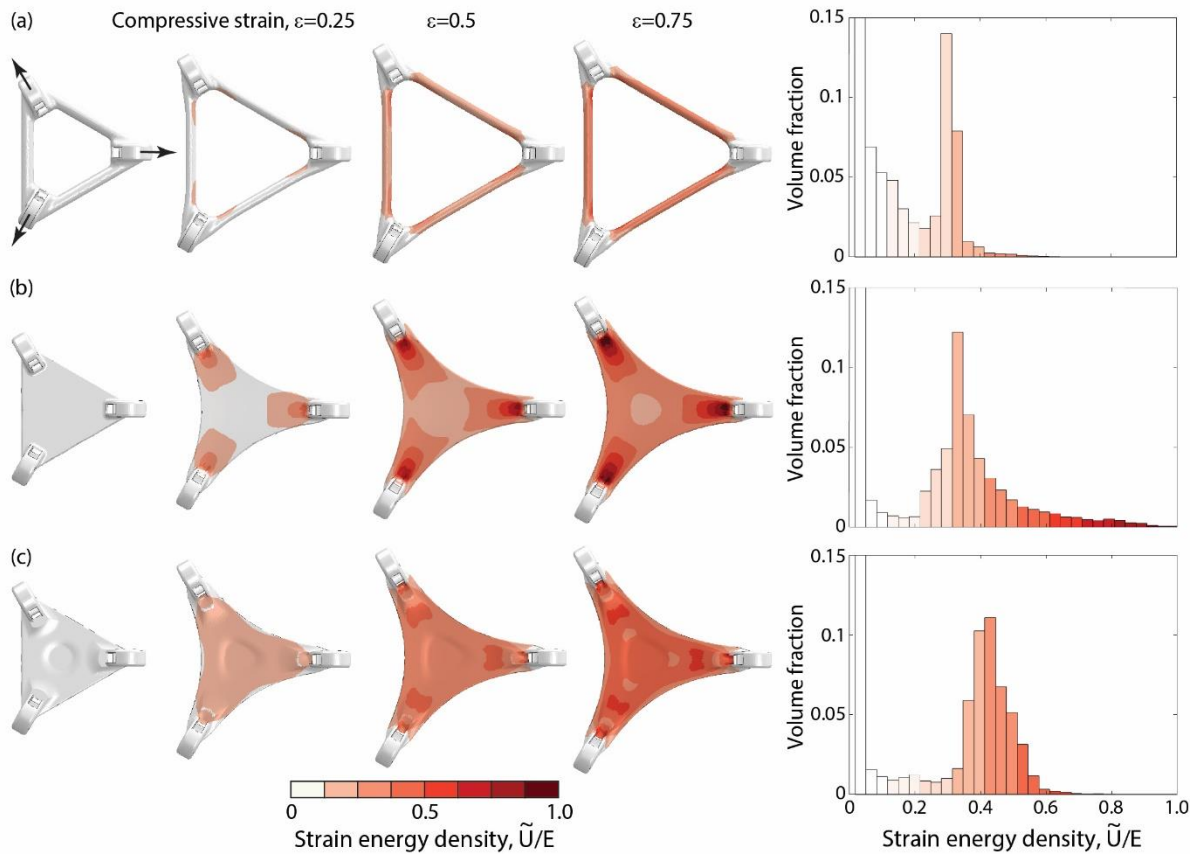


Figure 3.12: Energy density maps for tensile members composed of (a) straight struts, (b) uniform sheet, and (c) graded sheet are shown at progressively increasing macroscopic compressive strains. Accompanying histograms show strain energy density distributions at the largest compressive strain ($\varepsilon = 0.75$).

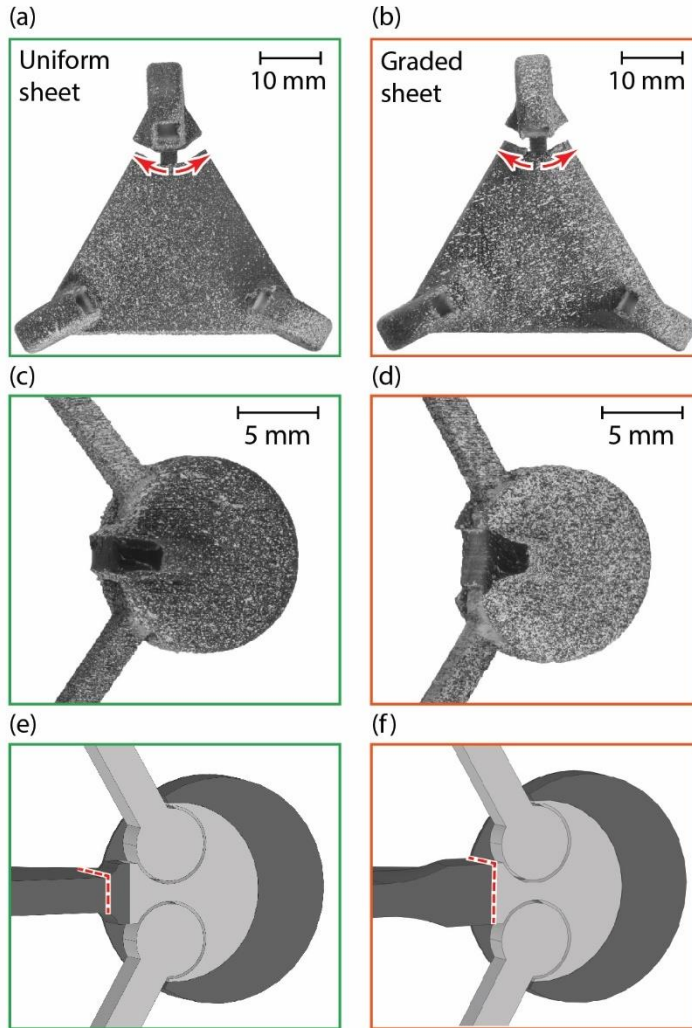


Figure 3.13: Photographs of (a) uniform sheet and (b) modified sheet show rupture initiating in the fillet region and spreading to the edges of the sheet (indicated by red arrows). (c-f) Viewed from a different perspective, images show one of two rupture paths (indicated by dashed red lines). Part of the white inner knuckle is visible in (d).

Chapter 4

Effects of Microstructure on the Deformation and Mechanical Response of Elastomeric Foams

Abstract

The current chapter investigates the effects of microstructural regularity, number of cells across a part or specimen, and boundary conditions on the compressive response of elastomeric foams. Various foam microstructures are generated using both a Voronoi tessellation method with a prescribed regularity parameter and a novel bubble growth algorithm. Microstructures of real foams and model foams are compared on the basis of cell size, cell interior angles, and number of struts per cell. Distributions of these features are represented using multivariate plots. A computationally efficient finite element method is then used to simulate the compressive response of the model foams. Results indicate that polydispersity in cell size affects the strain energy distribution across cells and in turn affects the compressive response. Specifically, foams with tight distributions in cell size exhibit stronger responses than those with wider distributions due to more uniformly distributed strain energy.

4.1 Introduction

Flexible elastomeric foams with stochastic microstructures are widely utilized to mitigate impact forces during human/solid interactions, notably in shoes, helmets and athletic mats¹⁻³. While structured foams with periodic cell arrangements offer exciting opportunities for improved performance⁴⁻⁶, manufacturing at scale remains a persistent challenge. As such, a detailed understanding of structure-property relationships in stochastic foams continues to play a critical role in tailoring materials to enhance performance.

While the broad scaling relationships of stochastic foams are well-known^{7,8}, the range and complexity of dynamic human/solid impact imply that the details of stress-strain response play a critical role in performance. Running shoes provide an excellent illustrative example; flexible polyurethanes widely used in soles often exhibit softening that can be characterized by a tangent modulus E_t that is a relatively small fraction of the initial modulus E_0 ⁹⁻¹¹. The softening reflected by the tangent modulus plays a critical role in foot strike forces prior to foam densification; though foot strike forces are complicated and involve many physiological factors, the magnitude of deceleration and duration of foot strike strongly impact comfort and stability of running.

In this context, the implications of tangent modulus can be illustrated with a simple model involving a fixed mass impacting a foam with a prescribed initial velocity. For simplicity, consider a bilinear foam response that neglects the role of densification. The initial stiffness of the foam sets the initial rise of the deceleration-time response of the impact; the tangent modulus limits deceleration and extends the duration of the foot-strike. For decreasing tangent modulus, the average deceleration of the foot-strike decreases, while the maximum compression of the foam increases.

For a range of impact energies, the trade-off in average acceleration and foam compression can be as high as a factor of five as the tangent modulus varies from zero to values equivalent to the initial modulus of the foam. That is, the average acceleration can decrease by a factor of four when switching from a purely linear material to one with an elastic-perfectly plastic response, while the compressive stress increases by a factor of six. In light of this and the diversity of foot-strike characteristics that stems from both physiology and application (i.e.,

prolonged walking vs. competitive running), controlling tangent modulus through variations in stochastic microstructure is of central interest for material and processing development.

Simply put, the shape of the “knee” in the compressive stress-strain curve of a foam (over 0~25% strain) plays an important role in determining the foot strike dynamics. Figure 4.1 provides a schematic of typical stress-strain curves and parameters used to characterize the “knee”. While the shape of the curve can be characterized in many ways, the simplest approach is to define an initial modulus (at zero strain) E_0 , a tangent modulus at a prescribed strain of interest E_t , and a characteristic stress σ_c . As illustrated in Figure 4.1, the characteristic stress is found from the intersection of lines tracing the small-strain response and the tangent modulus at the prescribed higher strain. Clearly, the characteristic stress will be somewhat sensitive to the prescribed strain used in the construction, and the sharpness of the softening transition is not fully captured by the initial modulus and the characteristic stress. In the absence of a rigorous methodology to characterize the traits, we use initial modulus, tangent modulus, and characteristic stress to characterize stochastic foams and discuss the implications of foam microstructure on these parameters.

In contrast to fully dense materials, for which 3D characterization has been elevated to encompass exquisite, quantitative details of grain size and shape, experimental characterization of foam microstructure has been sparse and limited to 2D sectioning. Only few high resolution CT scans are available¹²⁻¹⁴; to date, these have not yielded large datasets that have been segmented to establish statistical distributions of cell size, cell interior angles, or number of cell sides. As a result, the majority of previous studies have attempted to connect microstructure to mechanical response have relied on synthetic foam microstructures constructed using some variant on the Voronoi tessellation technique with some prescribed

“regularity”^{15–23}. Connections between synthetic microstructures and real microstructures are tenuous; while Voronoi foams “look like” real foams and regularized Voronoi foams “look more like” real foams, connections between foam “regularity” and foam compressive response have proven to yield conflicting conclusions regarding properties (see Table 4.1). Connections between specific microstructural features and compressive response have not been fully elucidated.

One goal of this work is to compare statistical distributions obtained from micrographs of real foams, regularized Voronoi foams, and a new ‘bubble growth’ algorithm inspired by the geometry of void coalescence. We illustrate that a narrow range of regularity parameters yields results that are consistent with a broad range of foams fabricated using gas-expansion and that the bubble growth algorithm produces statistical distributions of cell size, interior angles and cell sides that are comparable to real foams. While only a narrow range of regularity parameters are suitable for capturing the microstructure of real foams, using the full range of regularity values (from 0 to 1) creates an attractive opportunity to easily transition from purely stochastic foams to regular honeycombs, as will be illustrated.

It should be noted that the present study is limited to two-dimensional foams. Previous studies of 2D and fully 3D foams illustrate that there is strong similarity in the response, provided suitable scaling relationships are employed to adjust cell size by relative density^{7,15,16,24}. While this is naturally a first step towards understanding the roles of statistical distributions of cell size, future work will be needed to ensure the structure-property relationships illustrated here will translate to both open-cell and closed-cell 3D structures.

Comparisons of foams with various statistical distributions in cell size, interior angles and number of cell sides provide insight into several fundamental questions regarding the effect

of microstructure on mechanical response. (These have been touched upon in previous studies^{16–23,25,26}, but are significantly expanded upon by the present calculations.) For example, what is the difference between a ‘geometrical’ representative volume element (RVE) and the ‘mechanical’ RVE? The former addresses the number of cells needed to reproduce microstructural characteristics that are representative of a much larger sample; the latter addresses the number of cells needed to reproduce mechanical behaviors that are characteristic of a larger sample. Previous studies have not yielded a consensus on what constitutes an appropriate mechanical RVE and have not characterized microstructural features of samples with differing size or established protocols for determining a geometric RVE (Table 4.1).

The current chapter is organized as follows. A study of real foams and computationally generated foams (obtained with different generation algorithms) is outlined in Section 4.2. Strategies to process micrographs and to develop computer-generated foam microstructures are described. Methods used to predict the mechanical response of these foams are described in Section 4.3. In Section 4.4, statistical descriptions of foam microstructure are presented and discussed in terms of their similarities and differences. Section 4.4 illustrates the impact of microstructure on mechanical response and the impact of local cell collapse on macroscopic behavior. Section 4.5 provides a summary and conclusions.

4.2 Foam Microstructures

Three metrics are used to characterize stochastic foam microstructures: cell area, interior angles between cell walls, and the number of cell walls. Statistical distributions of these metrics are computed for three types of foam microstructures: (i) those measured of real foams, (ii) those generated via regularized Voronoi algorithms, and (iii) those generated using a new ‘bubble growth’ algorithm inspired by void coalescence (introduced in Section 4.2.3). In this

section, we first outline the methods used to characterize real foams and introduce multivariate density plots to illustrate the relationships between the three metrics. We then outline the algorithms to generate artificial foams; a comparison of the statistical distributions from real and artificial foams is presented in Section 4.4.

4.2.1 Real Foam Microstructures

Microstructural characteristics for real foams were obtained by processing images published elsewhere, using the following procedure. Figure 4.2a shows the cross section of a polyurethane foam from Brondi et al.²⁷; ImageJ was used to binarize the image (Fig. 4.2b). The resulting image was manually edited to ensure traces of cell walls produced closed loops. Centroids of each cell were then found using the function “regionprops” in Python (Fig. 4.2c). The centroid coordinates were used to generate a Voronoi mesh, which yields a reasonable representation of microstructure (Fig. 4.2d). Distributions in cell size, cell interior angles and number of sides (or struts) were then extracted from the Voronoi mesh. This process was repeated for a different closed-cell polymer foam²⁷ and a closed-cell metal foam²⁸. Since the distributions of cell characteristics for these three foam images proved to be similar (cell size coefficient of variation (CV) ranged from 0.32-0.42 and cell interior angle CV ranged from 0.15-0.19), the datasets were merged to increase the number of cells and establish representative distributions for gas-expansion foams. Individual datasets are presented in Appendix 4.A.

Cell areas, interior angles, and number of struts per cell were extracted from the segmented images; cells that intersect with the boundary of the images were ignored. Figure 4.3 illustrates resulting distributions of these characteristics, in the form of a bivariate

scatterplot with cell areas and interior angles as the two axes. Marginal plots outside of the scatterplot show the fitted probability density functions of each characteristic.

To illustrate coupling between the three cell characteristics, the number of struts per cell is indicated using conditional colors (Fig. 4.3b). Orange, blue, and green points correspond to cells having 3-4, 5-7, and 8+ struts per cell respectively. As illustrated in Figure 4.3, smaller cells are more likely to have low interior angles and low number of struts per cell (3-4 struts). Larger-than-average cells are more likely to have 8+ struts and are linked to higher interior angles.

To show the prevalence of different combinations of cell characteristics, namely cell size, cell interior angles, and number of struts per cell, Figure 4.3c shows the full plot of cell characteristics, while Figure 4.3d shows a separate plot for cells with 3-4 and 8+ struts with a magnified view of the marginal plots. The exact fractions of each group are also included. These plots illustrate that real foams generally do not have many cells with fewer than 4 struts or with interior angles $\theta \leq 90^\circ$. The average normalized cell size is 1 (naturally) with a coefficient of variation (CV) of 0.36. The average cell interior angle is 120° with a CV of 0.17. These results are subsequently used to assess the suitability of computationally generated foam microstructures, as discussed in Section 4.4.

4.2.2 Regularized Voronoi Foams

Both foam generation methods used in this work are grounded in the Voronoi tessellation technique. This method has been used extensively to create foams with irregular microstructures^{16,17,21,23,29,30}. To begin, N_{seed} points are assigned randomly to a square of dimensions $W_0 \times W_0$. The perpendicular bisectors to lines connecting each pair of adjacent points are generated, and each bisector is truncated at the two closest intersection points. Each

bisector represents a wall in the foam. The resulting average cell area is $\langle A_{cell} \rangle = W_0^2 / N_{seed}$, the average area-equivalent cell diameter is:

$$\lambda = 2\sqrt{\frac{\langle A_{cell} \rangle}{\pi}} = 2\sqrt{\frac{W_0^2}{\pi N_{seed}}} \quad (4.1)$$

and the average number of cells that span the width of a foam is W_0 / λ . To remove mesh-generated edge effects in the Voronoi tessellation, the foam edges are trimmed to produce a smaller foam with dimensions $W \times H$.

The structure resulting from random seeds and Voronoi tessellation can be made more regular using the method introduced by Zhu et al ¹⁵. First, define d_0 as the distance between any two adjacent seed points for purely identical hexagonal cells, constructed with the same number of seed points in the square area W_0^2 . This is given by:

$$d_0 = \sqrt{\frac{2W_0^2}{N_{seed}\sqrt{3}}} \quad (4.2)$$

Then, a regularity parameter, α , is defined as $\alpha = \delta / d_0$, where δ is the minimum allowable distance between the seed points. As seed points are generated sequentially, they are either accepted or rejected based on the minimum allowable distance, as defined through the regularity parameter. For a completely random Voronoi foam, $\alpha = 0$; any random seed is accepted regardless of how close it is to existing points. When $\alpha = 1$, all points not corresponding to hexagonal packing are rejected, resulting in a regular hexagonal honeycomb.

4.2.3. Bubble Growth Algorithm

The bubble growth algorithm is an alternative method to generate more ordered foam microstructures. This new method is based on the growth and coalescence of randomly placed

bubble ‘seeds’. At present, the bubble growth algorithm is purely geometric; bubble growth rates are arbitrary, and coalescence occurs when two circular bubbles intersect. One can envision future embellishments to capture the physics of gas-expansion and necking of cell walls for impinging voids.

The growth algorithm is shown schematically in Figure 4.4 To begin, N_{seed} points are randomly assigned within a $W_0 \times W_0$ square. Here, the seed points represent centroids of circular bubbles with a given size. Bubble radii are then increased incrementally; when two bubbles overlap to within some small tolerance (e.g., 1% of the average bubble size), they are replaced with a single bubble. The size of the new bubble is dictated by the total area of the two bubbles that have coalesced. The centroid (x_n, y_n) of the new bubble is a weighted average of the centroids of the original two bubbles, described by:

$$(x_n, y_n) = \frac{A_1}{A_n}(x_1, y_1) + \frac{A_2}{A_n}(x_2, y_2) \quad (4.3)$$

where A_1 and A_2 are the areas of the two respective bubbles and A_n is the sum of the two areas.

A foam can be defined by the Voronoi tessellation of the bubble centroids after any step in the growth algorithm.

Foams were generated using this algorithm as follows. For regular seeding, the maximum amount of growth from a seed is the area-equivalent diameter, λ . The growth rate (increase in the bubble radius per step) was fixed to be $G = \lambda / 2n_{\text{total}}$, where n_{total} is a prescribed number of steps, taken here to be 40. As the algorithm progresses and bubbles coalesce, the distribution in bubble sizes is recorded and used to examine the evolution of foam characteristics. Representative results that illustrate the outcome of this process are illustrated in Figure 4.5, which shows coefficients of variation of cell size, struts per cell, and fraction of

small interior angles as functions of growth steps. The results indicate that the foam collapses into just a few cells in n_{total} steps, as one would expect from the prescribed growth rate. Interestingly, the most regular foams (i.e., those with the lowest coefficients of variation) are consistently obtained at 60-70% of the number of steps needed to collapse the foam. This result is obtained regardless of whether more steps (i.e., slower growth rates) are used; subsequent ‘bubble growth foam’ microstructures correspond to this point in the growth process, i.e., when variations in bubble size, the struts per cell and fraction of low interior angles are at their minimum.

4.3 Scope of the Study and Numerical Approach

Having defined a microstructure, the mechanical response of the foam is simulated as follows. The simulation framework models cell walls using one-dimensional beam elements of uniform thickness t ; it assumes small strains but allows for large rotations. That is, deformation of cell walls and cell wall intersections is sufficiently small to ignore changes in mechanical response arising from large *material* deformations, while large *structural* deformations are fully captured. The formulation ignores shear deformation in the cell walls and utilizes Bernoulli-Euler beam kinematics; this is appropriate for cell wall aspect ratios (thickness to length) that are less than roughly 0.2, which corresponds to relative densities that are less than about 30%. The cell wall material was modeled as linear elastic. The element size was selected to be 1/3 the average length of a strut. A mesh convergence study indicated that this element size was sufficient to accurately capture the macroscopic load-displacement response. Results of the mesh convergence study are presented in Appendix 4.B. Simulations are terminated at macroscopic strains of 20%, which roughly corresponds to the onset of cell wall contact, i.e., at the *onset* of densification.

(It should be noted that densification typically manifests at much larger strains, when the volume density of cell wall contacts is dramatically higher at about 50% strain. As such, the present results can likely be extrapolated to somewhat higher macroscopic strains, although the extent of such extrapolations is undoubtedly dependent on microstructure and as such are not considered here.)

The mechanical response reported here corresponds to uniaxial compression of square specimens between rigid platens, with no sliding along the platens and no rotations of elements whose ends contact the platens. The rationale for this approach is that many foams have high coefficients of friction with metals and/or have dense ‘skins’ along their surface resulting from the foaming process. For sufficiently large foams (i.e., those larger than the mechanical RVE), the response is independent of the boundary conditions. It should be noted that the response of foams whose width is much larger than the length in the compression direction may be different; in these instances, lateral constraints imposed by the specimen aspect ratio may significantly alter the response. Essentially, the present calculations are plane stress, while relevant stress states for ‘foam strips’ may be closer to plane strain. This is briefly discussed in Section 4.4.

Finite element simulations were conducted using our in-house code (details included in Appendix 4.B). The upshot of the numerical formulation is that the present framework produces identical results to *Abaqus* for a given structure, with computational speeds that are 10^2 - 10^3 faster. For reasons we have not fully identified, the adopted co-rotational formulation provides a more robust convergence. That is, the fraction of simulations that run to completion (before errors associated with Newton-Raphson iteration terminate the algorithm) is close to 90%. This greatly facilitates the study of stochastic microstructures, which requires numerous

simulations of different structures with the same global characteristics. The present results discard simulations that crash prior to macroscopic strains of 20%, with additional calculations to ensure that at least 10 microstructures drawn from the same distribution are used to illustrate mechanical response.

Foam models with 100, 225, 400, and 900 cells per unit area were generated using the various foam generation techniques outlined in Section 4.2. These are referred to as 10x10, 15x15, 20x20, and 30x30 cell foams. Images of each foam type are pictured in Appendix 4.B. Three relative densities were selected for this study: $\bar{\rho} = 0.05$ ($\bar{\rho}_{true} = 0.049$), 0.15 (0.144), and 0.25 (0.235). Relative density is calculated as

$$\bar{\rho} = (1/WH) \sum_{i=1}^N l_i t \quad (4.4)$$

where t is the thickness of all struts, W and H are the width and height of the foam, N is the total number of struts in the foam, and l_i is the length of the i^{th} strut in a foam. True relative density, indicated in parenthesis after each relative density, is calculated by accounting for the overlap of material at the nodes:

$$\bar{\rho} = 1/WH \left[\left(\sum_{i=1}^N l_i t - t^2 \right) + M t^2 \right] \quad (4.5)$$

Here, M is the total number of nodes in the foam and t^2 is the area of overlapping strut material (initially subtracted from all struts and added back in for the total number of nodes).

A second finite element study was conducted to probe effects of microstructure, foam aspect ratio, and boundary conditions on the compressive response. Foam models were generated using the same techniques mentioned above but with dimensions that yielded aspect

ratios of 1:1, 2:1, and 4:1. Foam models are pictured in Appendix 4.B. This set of foams had a relative density of 15% (14.4%).

4.4 Results and Discussion

4.4.1 A Comparison of Cell Geometry Distributions of Different Foam Types

Figure 4.6 provides a comparison of regularized Voronoi and bubble growth foam characteristics, presented in the same format as the results for real foams shown in Figure 3. Results are shown for foam sections that measure roughly 30 cells per side. It is clear from these results that the bubble growth algorithm (Fig. 4.6f) produces similar results to the regularized Voronoi foams with $\alpha = 0.5$ (Fig. 4.6c). Both of these synthetically-generated foam microstructures produce cell characteristics that are close to those of real foams. Focusing on bubble growth foams, the coefficient of variation (CV) for cell areas is 0.31 (CV=0.36 for real foams), and the CV for cell interior angles is 0.19 (CV=0.17 for real foams). Fractions of cells with 3-4, 5-7, and 8+ struts (5.7%, 86.4%, 7.9% respectively) are also very similar to those measured in real foams (5.9%, 87.9%, and 6.2%). In contrast, foams generated with lower regularity parameters exhibit a larger area fraction of outsized and oddly-shaped cells and, as a result, contain ‘sharp’ cells with much lower interior angles. (Note that physical foams have minimum interior angles of more than 60° .) Similarly, regularized foams with regularity parameters above $\alpha = 0.5$ have a relatively small fraction of cells with number of sides outside the range 5-7. A key implication is that results for pure Voronoi foams (with $\alpha = 0$) have feature distributions that are quite unlike real foams.

The ability to generate synthetic foam microstructures provide an opportunity to identify a ‘geometric representative volume element (RVE)’, by comparing the distributions of foam ‘samples’ with different numbers of cells. Interestingly, Figure 4.7 illustrates that only

approx. 100 cells are needed to get representative distributions of cell characteristics. While changes in the distributions of cell characteristics are observable for specimens with 100 and 400 cells (10x10 and 20x20 cells on the sides), they are rather modest. For bubble growth foams, the CV for cell size decreases from 0.32 to 0.31 as the number of cells increases while the CV for cell interior angles stays the same (0.19). For Voronoi foams, the CV for cell size decreases from 0.53 to 0.51 as the number of cells increases, and the CV for cell interior angles stays the same (0.25). This has the critical implication that micrographs of real foams such as those used to generate Figure 4.3 are more than likely sufficient to identify meaningful distributions of geometric properties. Naturally, this conclusion may not strictly hold for stochastic anisotropic foams, but it is likely a useful guideline regarding the requisite number of cells along the edges.

4.4.2 Mechanical Response of Different Foam Types

A comparison of the compressive mechanical response of various types of foams are shown in Figure 4.8. The stress-strain curves represent the average of 10 simulations with standard error bars included. The foam stress is normalized by $E_s \bar{\rho}^{-3}$, the theoretical result that eliminates the role of the relative density and the modulus of the constituent material for bending-dominated structures. For comparison, the responses of regular hexagonal honeycombs are shown for two different cell orientations. The impact of specimen size (number of cells along the edges) is illustrated using different color shading.

The results in Figure 4.8 clearly illustrate that the *mechanical* RVE for realistic stochastic foams is distinct from the geometric RVE. That is, while a specimen with 10x10 cells produces relatively accurate distributions of cell geometries, it exhibits a softer response than a larger sample (30x30) with cell property distributions that are comparable. The root

cause of this difference is the constraint introduced by the top and bottom boundary conditions on the macroscopic sample, i.e., the use of fixed platens. Additional calculations (included in Appendix 4.B) with frictionless platens exhibit a weaker dependence on cell density, although the impact of boundary conditions still persist to a sample size of 30x30 cells. Across a variety of boundary conditions for square specimens, a minimum of 30x30 cells produces results that are independent of the specimen size. This result is consistent with previous studies²⁴. For *unrealistic* microstructures, i.e., those produced via Voronoi tessellation of random points, the mechanical response is relatively insensitive to the number of cells, such that geometric and mechanical RVEs appear to coincide. The response is likely softer than real foams, however, due to the presence of undersized and oversized cells and anomalously low cell angles.

It appears from the comparisons in Figure 4.8 that the upper bound on ordered cells (i.e., disordered foams with a high degree of regularity) approaches that of the 90° honeycomb, which has struts oriented 90° to the loading direction. Honeycombs with no struts that are perpendicular to the loading direction produce slightly stiffer responses and a lower tangent modulus associated with a distinct ‘collapse’ stress. Although the analysis of honeycombs is outside of the scope of this work, additional details on honeycomb responses are provided in Appendix 4.C.

In Figure 4.9a, stress-strain results for 30x30 cell foams generated using different regularity parameters ($\alpha = 0.25, 0.5, \text{ and } 0.75$) are compared to results from Fig. 4.8b. It is interesting to note that the stresses for fixed strain rise nearly linearly with the regularity parameter, from the softest response of purely random Voronoi foams to the hardest response associated with 90° hexagonal honeycombs. As with the statistical distributions of geometric metrics, the mechanical response of a bubble growth foam is virtually identical to a regularized

Voronoi foam with $\alpha = 0.5$. Simply put, bubble growth foams and regularized foams with $\alpha = 0.5$ are the same with respect to geometry and mechanical response. Figure 4.9b compares two sets of results for regularized foams: 10x10 and 30x30 cell foams. These results demonstrate that differences in response increase monotonically with increasing regularity (a trend also seen when comparing 10x10 and 30x30 cell Voronoi foams to results of bubble growth foams).

The scaling of elastic modulus and characteristic stress with relative density is shown in Figure 4.10 for 10x10 cell and 30x30 cell foams. The characteristic stress is defined by the intersection of the elastic modulus tangent and the instantaneous tangent modulus at $\varepsilon = 0.2$. Results are shown for small specimens – arguably the minimum specimen size with a geometric RVE – and large specimens whose mechanical response is independent of the number of cells. In all cases, the scaling of stiffness and characteristic stress follows the $\bar{\rho}^3$ scaling characteristic of bend-dominated foams. However, the geometric RVE samples (10x10 cells) are noticeably stiffer than those with more cells associated with the mechanical RVE. The influence of foam microstructure is perhaps surprising. Realistic foams (i.e., bubble growth foams and regularized Voronoi foams with $\alpha = 0.5$) exhibit 20% higher stiffness and 35% higher characteristic stress than purely random Voronoi foams. In light of the importance of the ‘knee’ in the stress-strain curve for some applications, these differences may be important.

Differences associated with each foam model are further illustrated in Figure 4.11. Here the instantaneous tangent modulus is plotted against compressive strain at strain increments of $\varepsilon = 0.02$. The curves reflect the range in values obtained from 10x10 to 30x30 cell foams for each foam type. Open and closed circles, plotted at increments of $\varepsilon = 0.05$, show

measurements for 10x10 and 30x30 cell foams. The range of observed tangent moduli for each foam type is significant, pointing to the importance of features in the microstructure that have an outsized impact on response. (This is the focus of the following section). As one might expect, the perfect regular hexagonal honeycombs exhibit higher tangent moduli at all strain levels. The difference in tangent moduli at 5-10% strain exhibited by purely random Voronoi foams and realistic ‘bubble growth’ foams can be substantial. This speaks to the importance of microstructure in the response near the ‘knee’ of the stress-strain curve. For example, the average tangent modulus of the bubble growth foam at 5% strain is twice that of the Voronoi foam. Notably, the tangent moduli at 20% strain are apparently independent of foam microstructure (excluding the ordered hexagonal foam); however, the stress levels at these strains can differ by as much as 50%, as indicated by the results in Figure 4.8. The origin of these differences is of central interest, as discussed in the next section.

4.4.3 Microstructural Features that Impact Foam Response

The microstructural origins of the differences highlighted in the previous section appear to stem from outlier cells, i.e. ones with extremes in interior cell angles, cell size or the number of cell walls⁵. To gain insight into the role of these ‘outlier’ cells, the mechanical response of the foams was analyzed as follows. The energy contribution of an interior cell—a cell not containing any struts at the edges of the foam—was computed as $U_{cell} = \frac{1}{2} \sum_{i=1}^N U_i$ where U_i is the strain energy of the i^{th} element of a cell, and N is the number of elements in the cell. (The coefficient $\frac{1}{2}$ is used because all interior cells share a strut with one other cell, so the energy is

⁵ It was also confirmed that differences in response did not arise from differences in energy partitioning (bending vs stretching). These results are included in Appendix 4.D.

split between the two.) The total strain energy contribution of a cell at a foam edge is computed

as $U_{cell} = \frac{1}{2} \sum_{i=1}^N U_i + \sum_{i=1}^M U_i$ where the first half of the equation sums up strain energies from N

total elements that are shared with neighboring cells, and the second half of the equation sums strain energies from M elements of the cell that are located at the edge and not shared with other cells. Strain energies were computed for three compressive strains: $\varepsilon = 0.05$, 0.10 , and 0.15 .

To determine how efficiently individual cells contribute to the macroscopic response, the strain energy of each cell, U_{cell} , is normalized by a nominal cellular strain energy, $U_{nom} = f_{cell} U_{tot}$ where f_{cell} is the volume fraction of a cell and U_{tot} is the total strain energy measured in the foam at a given compressive strain. The nominal strain energy is the energy that a cell would theoretically contribute if all cells uniformly deformed during compression. Ideally, normalized cell energies would be equal to 1, indicating that each cell contributed equally to the macroscopic mechanical response. Values less than 1 indicate that a cell contributes less strain energy for its size while values greater than 1 indicate the opposite. The average normalized cell energy in a foam, $\sum_{cell=1}^N (U_{cell} / f_{cell} U_{total}) / N$, indicates how close the deformation of cells in a foam is to the ideal case of uniform deformation. Here, N is the total number of cells in the foam.

Contributions of individual cells are plotted in Figure 4.12a, with fitted probability density functions. Figures 4.12b-4.12d show the evolution of cellular strain energy within each foam (representative foams are chosen for Voronoi and bubble growth cases). At each of the three compressive strains, the PDF for Voronoi foams is skewed right indicating that a large fraction of cells contribute minimally to the total strain energy. Cells with very low strain

energies, $U_{cell} / U_{nom} \leq 0.3$, appear as white cells in Figure 4.12b. These cells make up 28-36% of total cells at each compressive strain. The large fraction of minimally contributing cells results in the lowest mean normalized cell energy of each foam type, $\phi = \langle U_{cell} / U_{nom} \rangle = 0.62$. The inefficient energy contributions from individual cells explain why this type of foam exhibits the weakest stress-strain response. The PDF for bubble growth foams is still skewed right, but fewer cells (21-25%) have very low normalized cell strain energies, and a higher fraction of cells have normalized energies close to the ideal value of 1. This results in a mean normalized cell energy of $\phi = \langle U_{cell} / U_{nom} \rangle = 0.71$. The more efficient energy contributions of cells result in a stronger stress-strain response compared to random Voronoi foams. The probability density curve for the honeycomb is significantly different from those of bubble growth and Voronoi foams. This curve has a peak around $U_{cell} / U_{nom} = 1$ and has fewer low energy cells than the other foam types (only 5-10%). Additionally, the average normalized cell energy is $\phi = \langle U_{cell} / U_{nom} \rangle = 0.82$. More uniform and hence more efficient distributions of cell energies lead to a stronger stress-strain response.

Analyzing the energy maps in Fig 4.12b-d helps to identify the specific microstructural features causing differences in energy distributions. Cell energies mapped onto the Voronoi foam (Fig. 4.12b) show distinctive clusters of very low normalized cell energies (white) and very high energies (dark red). As the foam is compressed, most deformation is accommodated by a few clusters of cells that deform significantly more than other cells while many cells remain nearly undeformed (especially at top and bottom boundaries). The cells contributing significantly more energy than expected ($U_{cell} / U_{nom} \geq 1.5$) have an average cell size of $A_{cell} / \langle A_{cell} \rangle = 1.22$ while very low energy cells ($U_{cell} / U_{nom} \leq 0.3$) have an average size of

$A_{cell} / \langle A_{cell} \rangle = 0.83$. For the Voronoi foam, a wide distribution in cell sizes leads to larger than average cells accommodating compressive strain while smaller cells contribute less. Figure 4.13 shows the relationship between cell size and normalized cell energy for 30x30 cell Voronoi foams at three compressive strains ($\varepsilon = 0.05, 0.1, \text{ and } 0.15$). For these plots, energies of cells at the top and bottom boundaries were not counted. At each compressive strain, cell size and cell energy are positively correlated, and the strength of correlation increases with compressive strain. It was also found that across each compressive strain, about 73% of smaller-than-average cells ($A_{cell} / \langle A_{cell} \rangle < 1.0$) with higher-than-average normalized energies ($U_{cell} / U_{nom} > 1$) have at least one large-cell neighbor ($A_{cell} / \langle A_{cell} \rangle \geq 1.5$). Collectively, these results indicate that the distribution of cell size is an important feature of a foam.

Cell energy maps for other foams reinforce the impact of polydispersity in cell size. From the foam analysis in Fig. 4.7, bubble growth foams have a tighter distribution of cell sizes. As a result, a larger fraction of cells efficiently contributes to the total strain energy in the foam (Fig. 4.12c). Groupings of high energy cells exist, but there are fewer low energy cells and more moderate energy cells present during deformation. The honeycomb has uniform cell sizes and, as a result, significantly more cells efficiently contribute to the response. Note that low energy cells near the top and bottom edges are seen in all three of the foams. This is due to prescribed boundary conditions where displacement and rotation of edge nodes are fixed.

Differences in energy distributions fade for specimens with fewer cells. Cellular strain energy measurements taken for cells in 10x10 cell foams are given in Figure 4.14. Probability density functions at the top of the figure show that peaks shift to the left for all foams but are more drastic for bubble growth and honeycomb foams. Compared to results for 30x30 cell

foams, average normalized cell energies, $\phi = \langle U_{cell} / U_{nom} \rangle$, decrease by 2% for 10x10 cell Voronoi foams, 11% for bubble growth foams, and 21% for the honeycomb. In these cases, boundary conditions significantly affect the response and indicate the greater sensitivity of more regular foams (having tight distributions in cell size) to the number of cells spanning a dimension.

4.4.4 Impact of Foam Aspect Ratio on Response

Results of the second FE study highlight the combined effects of microstructure, finite foam size, and boundary conditions. Stress-strain responses of 1:1, 2:1, and 4:1 aspect ratio foams with the same number of cells per unit length are plotted in Figure 4.15. General trends in response align with findings of the previous study: foams with tighter distribution in cell size have stronger stress-strain responses. However, features of the response are also affected to varying extents by the foam aspect ratio. In the linear elastic regime, Young's modulus values for 4:1 foams are significantly higher than those in equivalent 1:1 aspect ratio foams. As aspect ratio increases, the lateral constraint from top and bottom boundary conditions puts the foams in increasing states of biaxial stress. Foams in biaxial compression have higher Young's modulus values than those in uniaxial compression because bending is constrained, and axial extension/compression of struts becomes more significant.

In the nonlinear regime, changing the foam aspect ratios leads to various collapse behaviors. For honeycomb 90 foams, elastic collapse does not occur in the 1:1 aspect ratio case. However, as aspect ratio increases, elastic collapse occurs at approximately 10% strain for the 2:1 foam and at 2.5% strain for the 4:1 foam. The stress at which collapse occurs also decreases with increasing aspect ratio. The progression of deformation in each of these three cases (Fig. 4.16) illustrates the source of differences in response. For the 1:1 aspect ratio foam,

deformation at each compressive strain is accommodated by strut bending with some strut buckling at the foam edges. This causes gradual softening in response. Deformation in the 2:1 aspect ratio foam is initially dominated by strut bending with minimal buckling at edge struts. At higher compressive strains, mode II buckling occurs due to the increased biaxial stress. As aspect ratio increases to the 4:1 foam case, so does lateral compressive stress, reducing the applied stress needed to cause buckling⁷. This explains why mode II buckling occurs at a lower compressive stress and strain than in the 2:1 aspect ratio foam (illustrated in Fig. 4.16).

In other foams, results indicate that increasing the aspect ratio causes elastic collapse to occur more abruptly at lower compressive strains. This is most evident in the Honeycomb 0 foam. In the 1:1 aspect ratio case, deformation is initially accommodated by strut bending and buckling at the edges (Fig. 4.17a) causing a gradual reduction in tangent modulus. At higher compressive strains, mode I buckling begins to dominate in the foam and causes the response to transition to a plateau stress. For the 2:1 aspect ratio foam, strut bending is the dominant deformation mode at low strains, and strut buckling occurs only at the corners of the foam. The smaller fraction of buckled struts results in less softening of the response. Due to the increased biaxial stress state at higher aspect ratios, the compressive stress required to cause buckling is reduced, and elastic collapse occurs at lower strains. In the 4:1 aspect ratio foam, mode I buckling occurs at even lower compressive stresses and strains, truncating the gradual softening seen in the response of lower aspect ratio foams. (Fig. 17c highlights mode I buckling occurring in the foam.) From these results, increasing the foam aspect ratio, and biaxial stress state, reduces the gradual softening and causes large scale elastic collapse within the foam at lower compressive strains. Additional results for bubble growth and Voronoi foams are given in Figures 4.18 and 4.19 respectively.

4.5. Conclusions

The present study of stochastic foams provides the following insights regarding the role of microstructure on the shape of the stress-strain response near the ‘knee’ associated with a decrease in tangent modulus:

1. Foam microstructures associated with a purely random Voronoi structure do not reproduce characteristics of physical foams, exhibiting a broader range of cell sizes, number of struts per cell, and cell interior angles. In contrast, regularized Voronoi structures with a regularity parameter of $\alpha = 0.5$, or a novel ‘bubble growth’ algorithm produce geometric features in close agreement with physical foams.
2. The physical sample size (in terms of the number of cells along an edge) required to accurately represent statistical distributions in geometric features is roughly ten cells, irrespective of the method used to obtain realistic features. This implies that micrographs with ~ 10 cells along an edge are capable of producing distributions of cell characteristics that can be used to evaluate synthetic (algorithmic) foams with realistic microstructure.
3. The physical sample size required to accurately predict mechanical response (without artificial invocations of periodicity) is approximately 30 cells along an edge. While smaller samples are acceptable for pure Voronoi foams (with $\alpha = 0$), the resulting foam microstructures contain features inconsistent with physical foams.
4. Stochastic foams with feature distributions consistent with physical foams are significantly stiffer (by about $\sim 20\%$) and exhibit higher stresses (by about $\sim 35\%$) at moderate strains than purely random Voronoi foams (with $\alpha = 0$). One possible explanation is that outlier cells play an important role in governing the transition from

the initial modulus to the tangent modulus, an important consideration for foams designed for moderate strains.

5. The importance of outlier cells suggests that ‘tailoring’ of stochastic foams will require controlling foaming processes to control the distribution of undersized or oversized cells. In general terms, softer responses (lower tangent moduli) are likely obtained with broader distributions in cell characteristics, while harder responses (higher tangent moduli) will require the elimination of outliers. The novel ‘bubble growth’ algorithm presented here for generating stochastic microstructures is one potential approach to identifying suitable process strategies, e.g. by controlling the distribution of void seeding and growth rates to achieve novel foam microstructures, including anisotropy.
6. Nuanced changes in the sensitivity of response to cell size polydispersity arise for foams with high aspect ratios. For foams with uniform cell size, e.g., honeycombs, increasing the foams aspect ratio from 1:1 to 4:1 leads to a more abrupt transition from the linear domain to the stress plateau. This type of transition may not be ideal for impact scenarios such as those obtained during running. Here, the more gradual transition obtained in foams with moderate distributions in cell size may be preferable.

References

1. Lyn, G. & Mills, N. J. Design of foam crash mats for head impact protection. *Sport. Eng.* 4, (2001).
2. Mills, N. J., Fitzgerald, C., Gilchrist, A. & Verdejo, R. Polymer foams for personal protection: Cushions, shoes and helmets. *Compos. Sci. Technol.* 63, 2389–2400 (2003).
3. Arton Tomin, M. & Kmetty, A. Polymer foams as advanced energy absorbing materials for sports applications-A review. (2021). doi:10.1002/app.51714
4. Jafferson, J. M. & Pattanashetti, S. Use of 3D printing in production of personal protective equipment (PPE) - A review. in *Materials Today: Proceedings* 46, (2021).
5. Clough, E. C. *et al.* Elastomeric Microlattice Impact Attenuators. *Matter* 1, (2019).
6. Duncan, O. *et al.* Review of auxetic materials for sports applications: Expanding options in comfort and protection. *Applied Sciences (Switzerland)* 8, (2018).
7. Gibson, L. J. & Ashby, M. F. *Cellular solids: structure and properties*. (Cambridge University Press, 1997).
8. Ashby, M. F. Cellular Solids – Scaling of Properties. in *Cellular Ceramics* (2006). doi:10.1002/3527606696.ch1a
9. Verdejo, R. & Mills, N. J. Heel-shoe interactions and the durability of EVA foam running-shoe midsoles. *J. Biomech.* 37, (2004).
10. Shariatmadari, M. R., English, R. & Rothwell, G. Effects of temperature on the material characteristics of midsole and insole footwear foams subject to quasi-static

- compressive and shear force loading. *Mater. Des.* 37, (2012).
11. Jenkins, M. & Mills, N. J. Running shoe materials. in *Materials in sports equipment*. 65–100 (Woodhead Publishing, 2003).
 12. Karimipour-Fard, P., Naeem, I., Mohany, A., Pop-Iliev, R. & Rizvi, G. Enhancing the accuracy and efficiency of characterizing polymeric cellular structures using 3D-based computed tomography. *J. Cell. Plast.* 57, (2021).
 13. Pérez-Tamarit, S., Solórzano, E., Hilger, A., Manke, I. & Rodríguez-Pérez, M. A. Multi-scale tomographic analysis of polymeric foams: A detailed study of the cellular structure. *Eur. Polym. J.* 109, (2018).
 14. De Pascalis, F., Nacucchi, M., Scatto, M. & Albertoni, R. Quantitative characterisation of low-density, high performance polymeric foams using high resolution X-ray computed tomography and laser confocal microscopy. *NDT E Int.* 83, (2016).
 15. Zhu, H. X., Hobdell, J. R. & Windle, A. H. Effects of cell irregularity on the elastic properties of 2D Voronoi honeycombs. *J. Mech. Phys. Solids* 49, 857–870 (2001).
 16. Sotomayor, O. E. & Tippur, H. V. Role of cell regularity and relative density on elasto-plastic compression response of random honeycombs generated using Voronoi diagrams. *Int. J. Solids Struct.* 51, 3776–3786 (2014).
 17. Alkhader, M. & Vural, M. Mechanical response of cellular solids: Role of cellular topology and microstructural irregularity. *Int. J. Eng. Sci.* 46, 1035–1051 (2008).
 18. Zhu, H. X. & Windle, A. H. Effects of cell irregularity on the high strain compression of open-cell foams. *Acta Mater.* 50, 1041–1052 (2000).

19. Alsayednoor, J., Harrison, P. & Guo, Z. Large strain compressive response of 2-D periodic representative volume element for random foam microstructures. *Mech. Mater.* 66, 7–20 (2013).
20. Luxner, M. H., Stampfl, J. & Pettermann, H. E. Numerical simulations of 3D open cell structures - influence of structural irregularities on elasto-plasticity and deformation localization. *Int. J. Solids Struct.* 44, 2990–3003 (2007).
21. Zhu, H. X., Thorpe, S. M. & Windle, A. H. The effect of cell irregularity on the high strain compression of 2D Voronoi honeycombs. *Int. J. Solids Struct.* 43, 1061–1078 (2006).
22. Sotomayor, O. E. & Tippur, H. V. Role of cell regularity and relative density on elastoplastic compression response of 3-D open-cell foam core sandwich structure generated using Voronoi diagrams. *Acta Mater.* 78, (2014).
23. Zhu, H. X., Hobdell, J. R. & Windle, A. H. Effects of cell irregularity on the elastic properties of open-cell foams. *Acta Mater.* 48, 4893–4900 (2000).
24. Tekoğlu, C., Gibson, L. J., Pardoan, T. & Onck, P. R. Size effects in foams: Experiments and modeling. *Progress in Materials Science* 56, (2011).
25. Duan, Y. *et al.* The cell regularity effects on the compressive responses of additively manufactured Voronoi foams. *Int. J. Mech. Sci.* 164, 105151 (2019).
26. Li, K., Gao, X. L. & Subhash, G. Effects of cell shape and strut cross-sectional area variations on the elastic properties of three-dimensional open-cell foams. *J. Mech. Phys. Solids* (2006). doi:10.1016/j.jmps.2005.10.007

27. Brondi, C., Santiago-Calvo, M., Di Maio, E. & Rodríguez-Perez, M. Á. Role of Air Bubble Inclusion on Polyurethane Reaction Kinetics. *Mater.* 2022, Vol. 15, Page 3135 15, 3135 (2022).
28. Bastawros, A. F., Bart-Smith, H. & Evans, A. G. Experimental analysis of deformation mechanisms in a closed-cell aluminum alloy foam. *J. Mech. Phys. Solids* 48, 301–322 (2000).
29. Shulmeister, V., Van Der Burg, M. W. D., Van Der Giessen, E. & Marissen, R. A numerical study of large deformations of low-density elastomeric open-cell foams. *Mech. Mater.* 30, (1998).
30. Li, K., Gao, X. L. & Wang, J. Dynamic crushing behavior of honeycomb structures with irregular cell shapes and non-uniform cell wall thickness. *Int. J. Solids Struct.* 44, 5003–5026 (2007).
31. Andrews, E. W., Gioux, G., Onck, P. & Gibson, L. J. Size effects in ductile cellular solids. Part II: experimental results. *Int. J. Mech. Sci.* 43, 701–713 (2001).
32. Babaei, S., Jahromi, B. H., Ajdari, A., Nayeb-Hashemi, H. & Vaziri, A. Mechanical properties of open-cell rhombic dodecahedron cellular structures. *Acta Mater.* 60, (2012).
33. Shi, X., Liu, S., Nie, H., Lu, G. & Li, Y. Study of cell irregularity effects on the compression of closed-cell foams. *Int. J. Mech. Sci.* 135, (2018).

Appendix 4.A: Microstructure Analysis of Real Foams

Multivariate plots for three separate real foams are given in Figure 4.A1. In all three cases, the majority of cells have 5-7 struts, and few cells have 3-4 or 8+ struts. Additionally, most cells do not have sharp interior angles. The distribution of cell area, however, varies between foam samples.

Appendix 4.B: Finite Element Simulations Supplementary Material

While the numerical formulation utilized here for handling large rotations is broadly consistent with that embedded in commercial codes such as *Abaqus*, our in-house code adopts an algorithm that is designed to increase simulation speed. The core concept of the algorithm is that the linear, small-deformation stiffness matrix for the beam elements is hard-coded (avoiding numerical integration), and large rotations are accounted for by transforming this matrix using a co-rotational formation. That is, the stiffness matrix in the deformed state is computed using *average* element rotation defined by the current nodal rotations. This implies that the instantaneous tangent stiffness matrix of the entire system (used to find define the Jacobian used in a Newton-Raphson iterative scheme for nodal equilibrium) can be computed from a series of matrix multiplications that can be easily hard-coded and hence fast. Full details of the mathematical implementation are presented elsewhere [*].

Foam models used in finite element studies are given in Figure 4.B1 and 4.B2. Results of the mesh convergence study are given in Figure 4.B3.

The majority of finite element simulations on foams were conducted using rigid boundary conditions (fixed platens). Additional simulations on Voronoi and bubble growth foams with

frictionless platens are given in Figure 4.B4 and compared to simulations using fixed platens. The responses of foams with frictionless platens exhibit a weaker dependence on cell density, although the impact of boundary conditions still persist to a sample size of 30x30 cells.

Appendix 4.C: Deformation and Response of Honeycombs

Honeycombs with cells in two orientations were simulated in uniaxial compression. Results from Figure 4.C1 show two distinct types of behavior indicated in the stress strain plot for 30x30 cell foams. This is due to two different deformation mechanisms. In Honeycomb 0 foams, struts initially deform via bending of most struts and buckling of vertical edge struts in the strain range $\varepsilon = 0.01 - 0.10$. Beyond strains of 10%, elastic collapse occurs within the honeycomb causing the plateau stress pictured (blue curve). In Honeycomb 90 foams, struts deform via bending at each compressive strain. Strut buckling in vertical struts at the foam's edges also occurs, but these struts account for a small fraction of the total. This is pictured in the top row of the figure. As a result of this deformation mode, the stress doesn't exhibit a plateau, and the tangent modulus only gradually decreases at each compressive strain.

Appendix 4.D: Bending and Stretching Energy Partitioning for Each Foam Type

One hypothesis for stress-strain differences between foam types was that each foam partitioned strain energy differently during deformation. When a foam is compressed, the total strain energy stored in the foam is made up of bending and stretching components. If honeycomb and bubble growth foams had a larger fraction of stretching strain energy compared to random Voronoi foams during deformation, this would explain their stronger responses.

To investigate this hypothesis, the strain energy in each strut was partitioned into bending and stretching components and summed to yield total energies, U_b and U_s . Each strain energy component was then differentiated by compressive displacement (resulting in bending and stretching forces) and then divided by the width and unit depth of the foam to yield total bending and stretching stress contributions from all struts in the foam. Results from energy and stress partitioning are plotted in Figure 4.D1 for 30x30 cell foams. 30x30 cell foams were selected because significant differences in response were most evident between foams at this cell density. Clear differences in energy partitioning should be seen if the hypothesis is correct. However, the plots show that for each foam type and across each relative density, energy is partitioned similarly; one foam type does not have a significantly higher stretching contribution across the full strain range. In fact, stretching contributions are small compared to bending especially at lower relative densities. These results show that foams with more ordered microstructures have higher bending (effectively total) stresses than foams with irregular microstructures.

Table 4.1: Summary of previous studies of foams shows (i) if the study conducted a convergence study to find a mechanical representative volume element, (ii) if a geometric representative volume element was found, and (iii) how the elastic modulus and collapse stress vary with increasing regularity of foam microstructure. The relative densities investigated by each study are also included.

	2D	3D	
Elastic Foams		Open-cell	Closed-cell
Mechanical RVE convergence	17x17 ¹⁵ - ¹⁹ 8x8 ²¹	N=27 cells ¹⁸ N=125 cells ²³	
Geometric RVE			
Young's modulus, E_0	Increase $\bar{\rho} = 5\%$ ¹⁹ Decrease $\bar{\rho} = 1-8\%$ ^{15,21}	Decrease $\bar{\rho} = 1-8\%$ ^{18,23}	
Collapse stress, σ_c	Increase ^{15,19,21}	Increase ¹⁸	

	2D	3D	
Elastic Foams		Open-cell	Closed-cell
Mechanical RVE convergence	32x32 ²⁴ 15x15 ¹⁷ 16x16 ¹⁶	6x6x6 ²² cited exp. Results from Andrews et al. 2001 ³¹ - ²⁰ - ³²	6x6x6 ³³ and 5x5x5 ²⁵ cited exp. Results from Andrews et al. 2001 ³¹
Geometric RVE			
Young's modulus, E_0	Decrease $\bar{\rho} = 3-9\%$ ¹⁶ Insensitive $\bar{\rho} = 15\%$ ¹⁷	Increase $\bar{\rho} = 3-9\%$ ²² Increase $\bar{\rho} = 12.5\%$ ²⁰ Decrease $\bar{\rho} = 1-10\%$ ³²	Decrease ³³ Increase ²⁵
Collapse stress, σ_c	Increase ^{16,17}	Increase ^{20,22,32}	Increase ^{25,33}

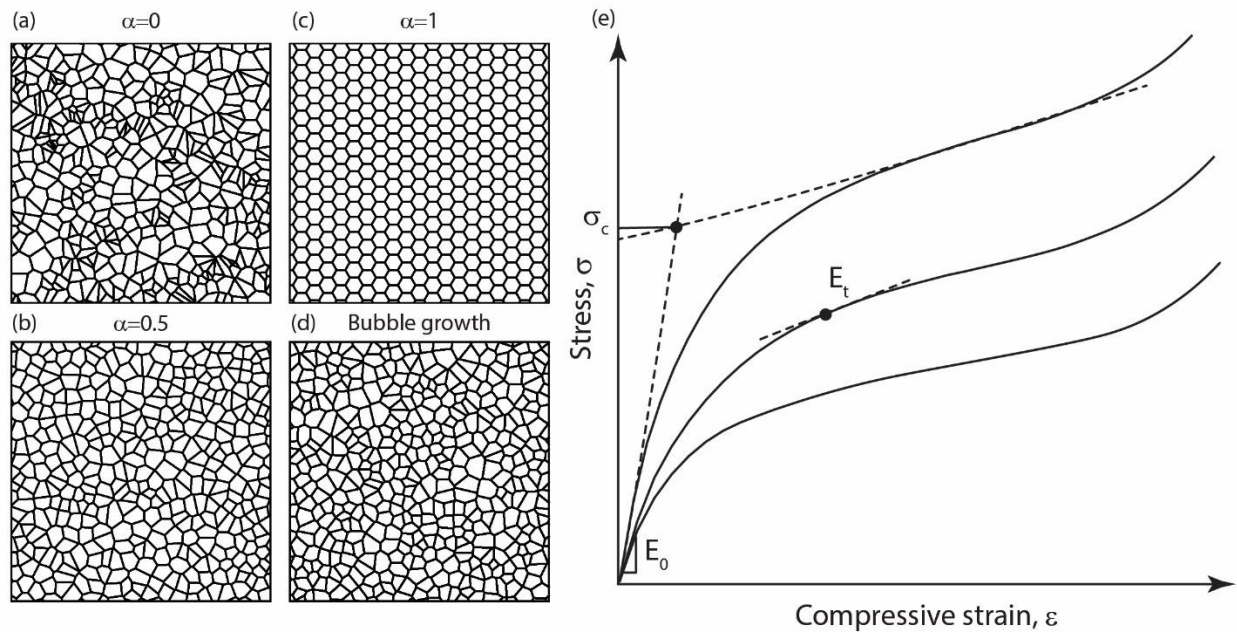


Figure 4.1: Illustrations of foam microstructures: (a) Voronoi tessellation of random points, (b) regularized Voronoi tessellation with regularity parameter $\alpha = 0.5$, (c) a perfect hexagonal honeycomb corresponding to a regularity parameter $\alpha = 1$, and (d) result of the bubble growth algorithm. (e) Typical stress-strain curves of an elastomeric foam, showing (i) the initial Young's modulus E_0 , (ii) the instantaneous tangent modulus E_t , and (iii) the characteristic stress σ_c as defined by the backwards projection of the tangent modulus at a fixed strain interval.

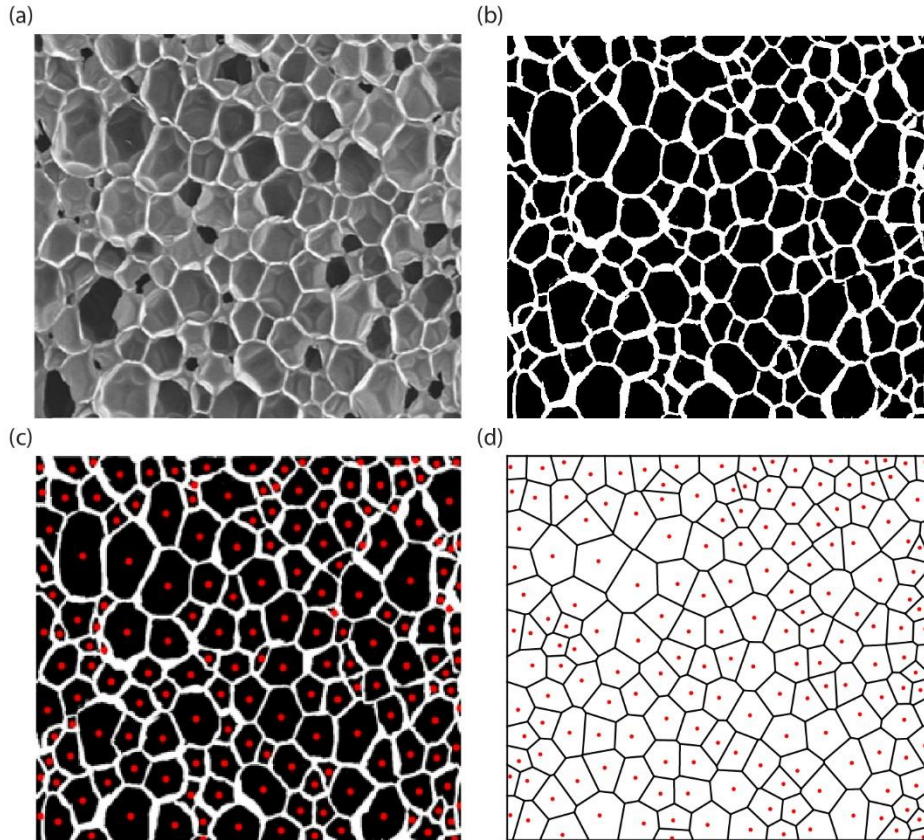


Figure 4.2: (a) Microstructure image of a polyurethane closed-cell foam from Brondi et al.³⁸. (b) Image after threshold editing using ImageJ. (c) Centroids are found for each cell from the segmented image. (d) A Voronoi mesh is generated using the centroids as the seed points.

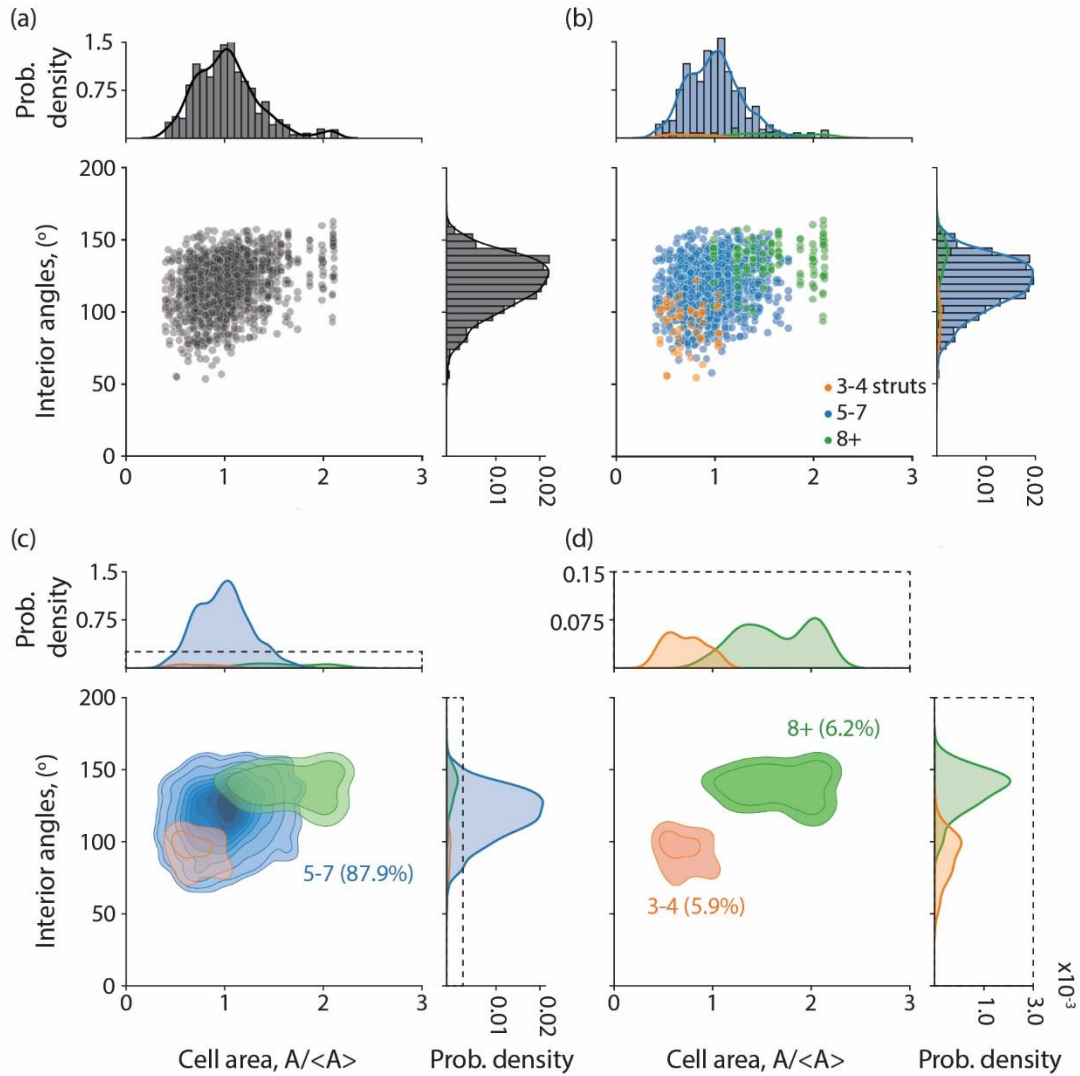


Figure 4.3: (a) A bivariate scatterplot with cell area and interior angles as axes, made from analyzing images of gas-expansion polymer and metal foams. Plots on the edges show fitted probability density functions of each characteristic. (b) Datapoints in the scatterplot are colored orange, blue, and green for cells having 3-4, 5-7, and 8+ struts. Normalized probability density functions in the marginal plots are also updated to show the distributions of cell characteristics for each of the three color groups. (c) A density plot of the joint probability distributions shows regions where the datapoints are concentrated for each of the three groups. The joint density plot is separated to show (d) a magnified view of the marginal plots for 3-4 and 8+ sided cells. Percentages of each category are included in the plots.

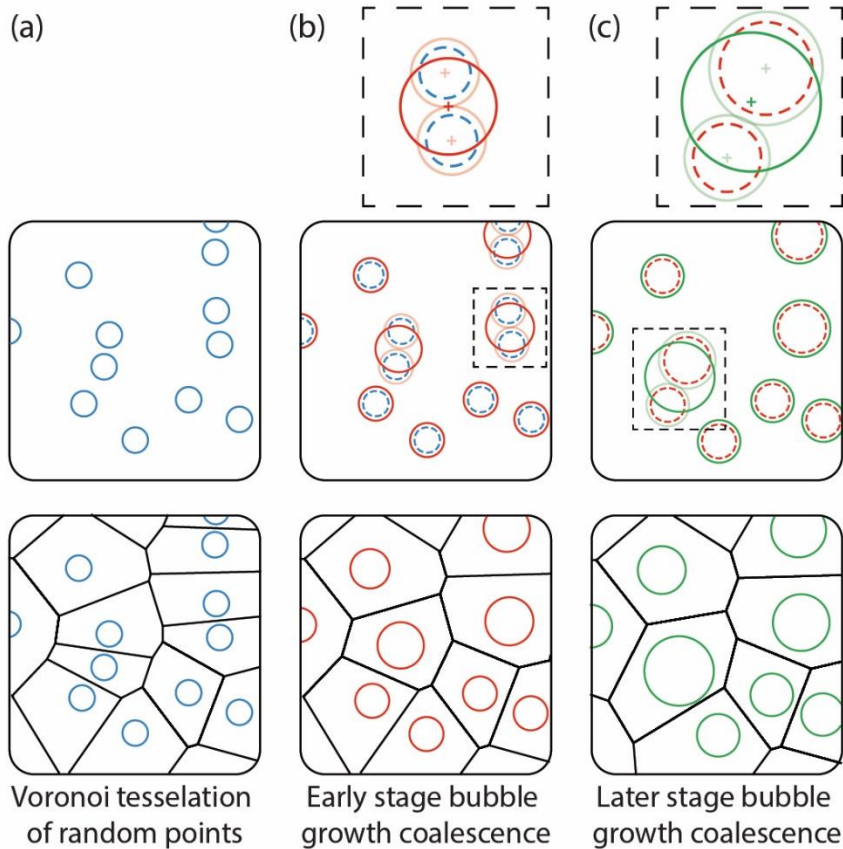


Figure 4.4: Illustrations of the bubble growth algorithm show bubbles growing at three growth steps and resultant foam structure (bottom panes). (a) Centroids of bubbles are used to generate Voronoi meshes. (b) As bubbles grow (dashed blue to red) some bubbles merge when the distance between edges is smaller than a specified tolerance. (c) In a later growth step (dashed red to green), some bubbles with dissimilar areas merge and the new centroid is weighted by the two bubble areas.

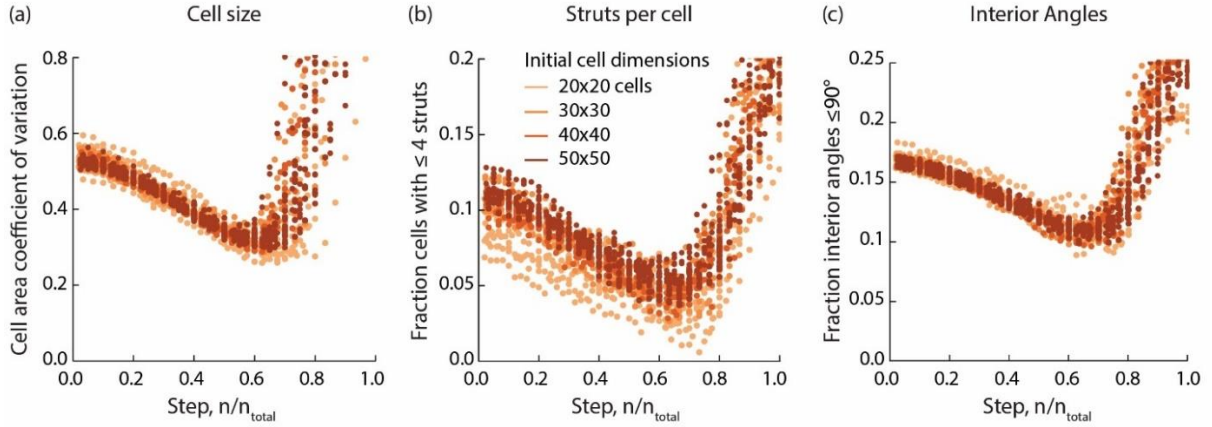


Figure 4.5: Three characteristics of foam microstructure are tracked for foams with different initial cell dimensions at each growth step: (a) cell area coefficient of variation, (b) fraction of cells with ≤ 4 struts, fraction of cells with interior angles $\leq 90^\circ$. In each plot, the lightest red points track microstructural features in 15 foams with 400 initial cells (20x20) and the darkest red points track features in 15 foams with 2,500 cells (50x50). At moderately high growth steps, $n / n_{total} = 0.6 - 0.7$, variation between cell areas and unrealistic cell characteristics reach a minimum.

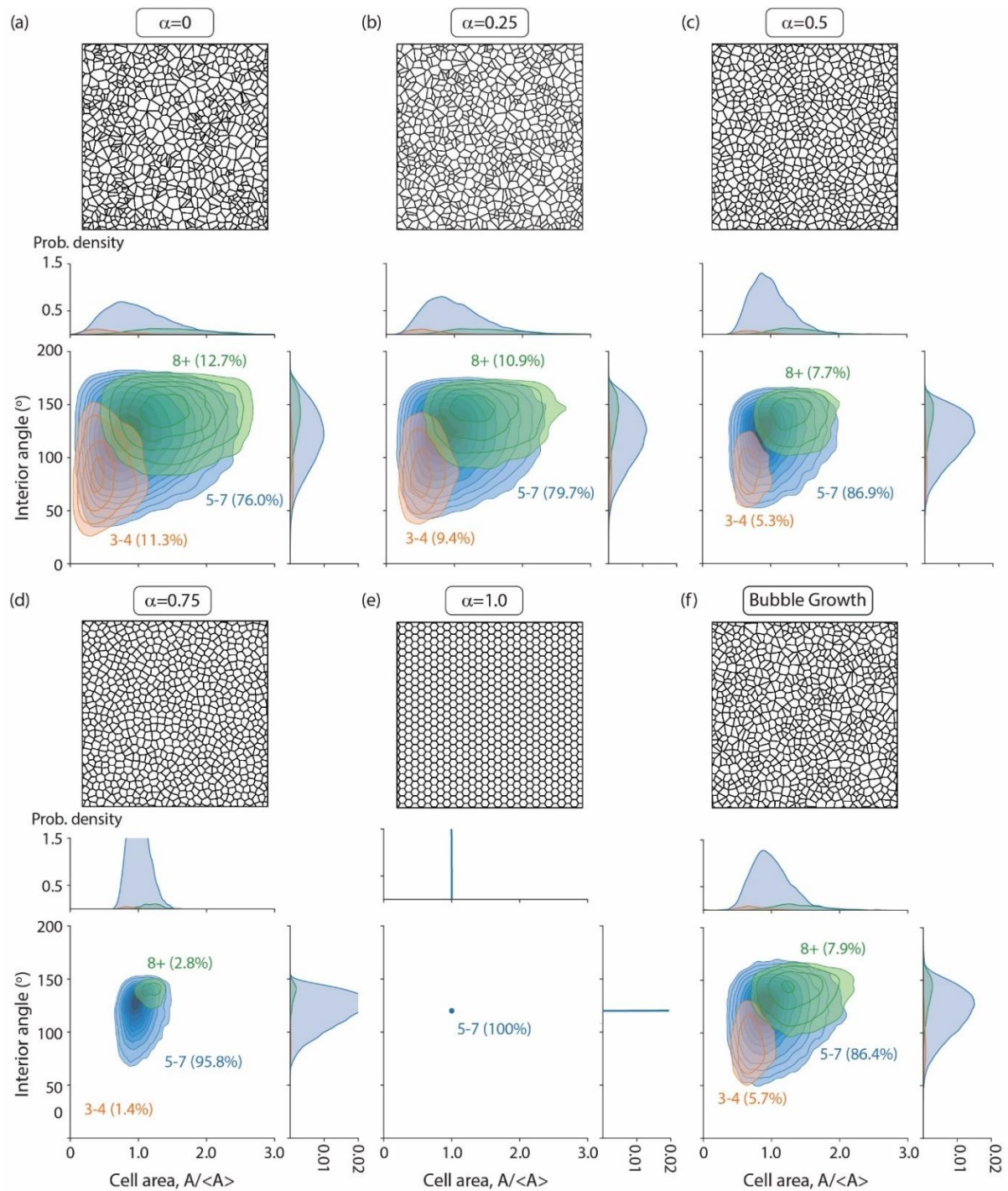


Figure 4.6: Multivariate density plots are used to illustrate distributions in microstructural features of foam ranging in regularity parameter: (a) $\alpha = 0$, (b) $\alpha = 0.25$, (c) $\alpha = 0.5$, and (d) $\alpha = 0.75$, (e) $\alpha = 1$. (f) results from foams generated using the bubble growth algorithm is plotted for comparison. Each plot shows the results of 10 generated foams. Examples of each analyzed foam are illustrated above the plots.

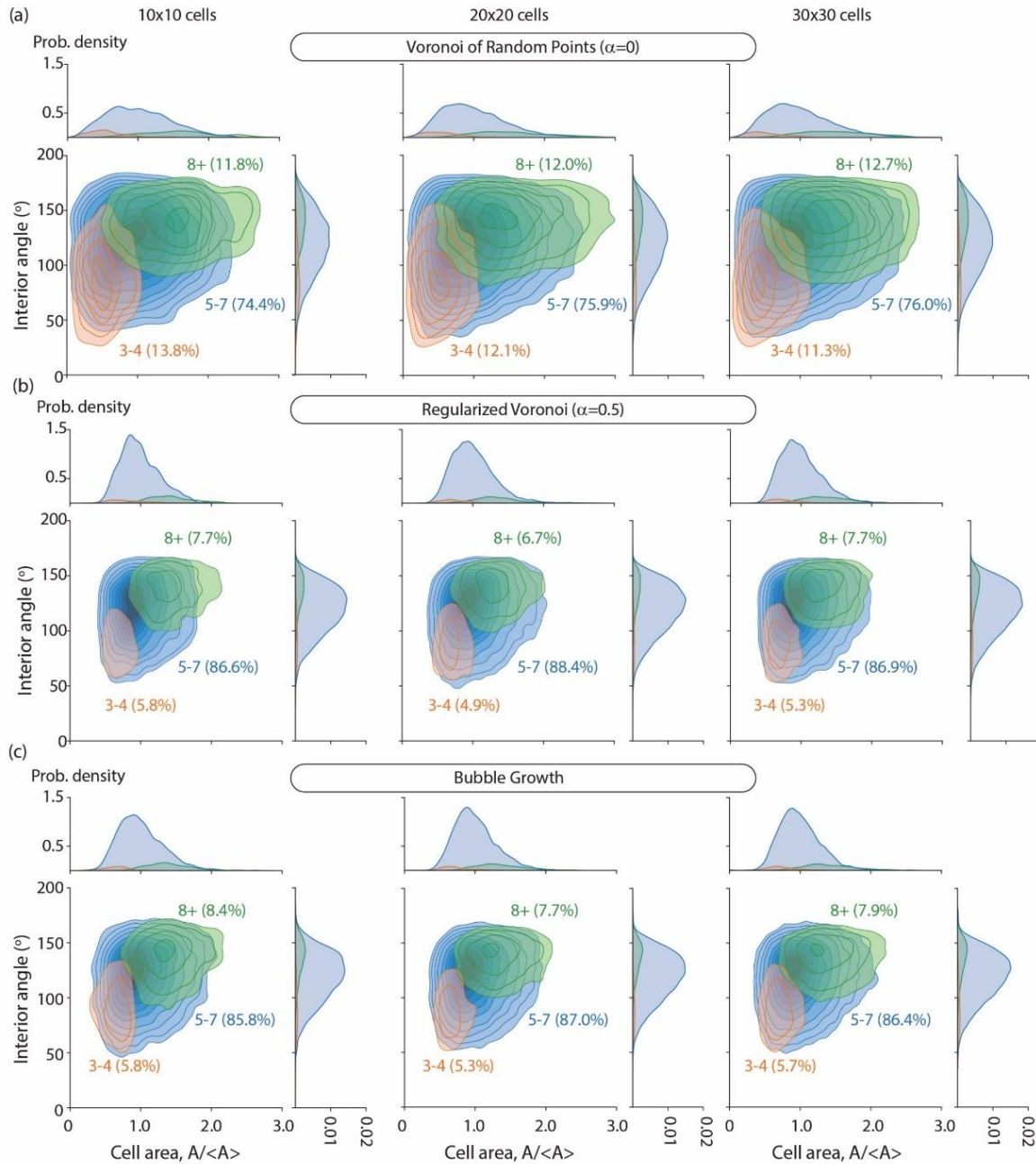


Figure 4.7: Multivariate density plots for (a) Voronoi tessellated foams and (b) regularity parameter foams ($\alpha=0.5$), and (c) bubble growth generated foams with different cell densities. Distributions in microstructural features are consistent across 10x10, 20x20, and 30x30 cell foams. Orange, blue, and green data shows cells with 3-4, 5-7, and 8+ struts respectively.

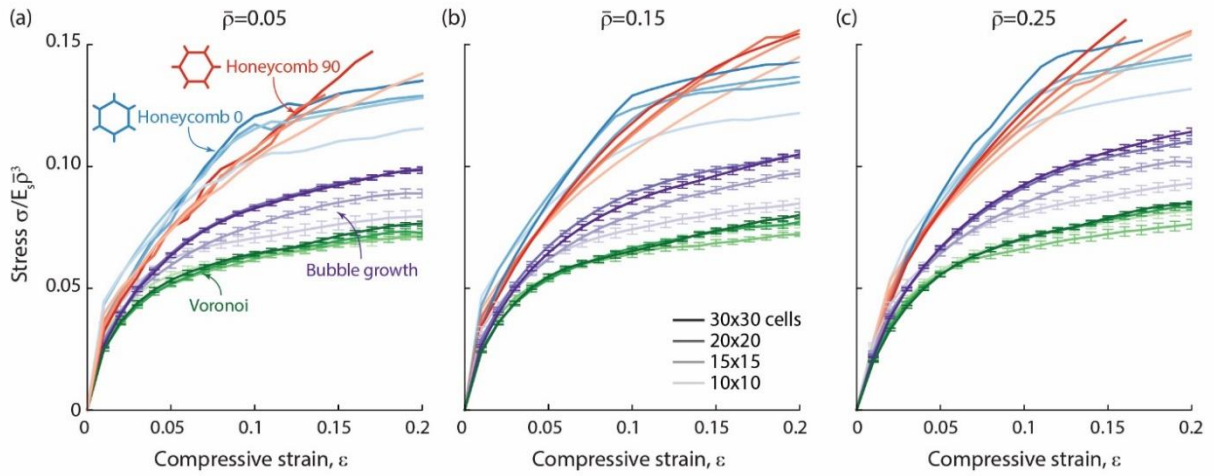


Figure 4.8: Normalized stress-strain results are plotted at for honeycombs in two orientations (red and blue), bubble growth foams (purple) and Voronoi-tessellated foams (green) at three relative densities: (a) 0.05, (b) 0.15, and (c) 0.25. The darkest shade of each color corresponds to 30x30 cell foams. As colors get lighter, the cell density in the foam decreases to 20x20, 15x15, and 10x10 cells. Standard error bars are included for each response.

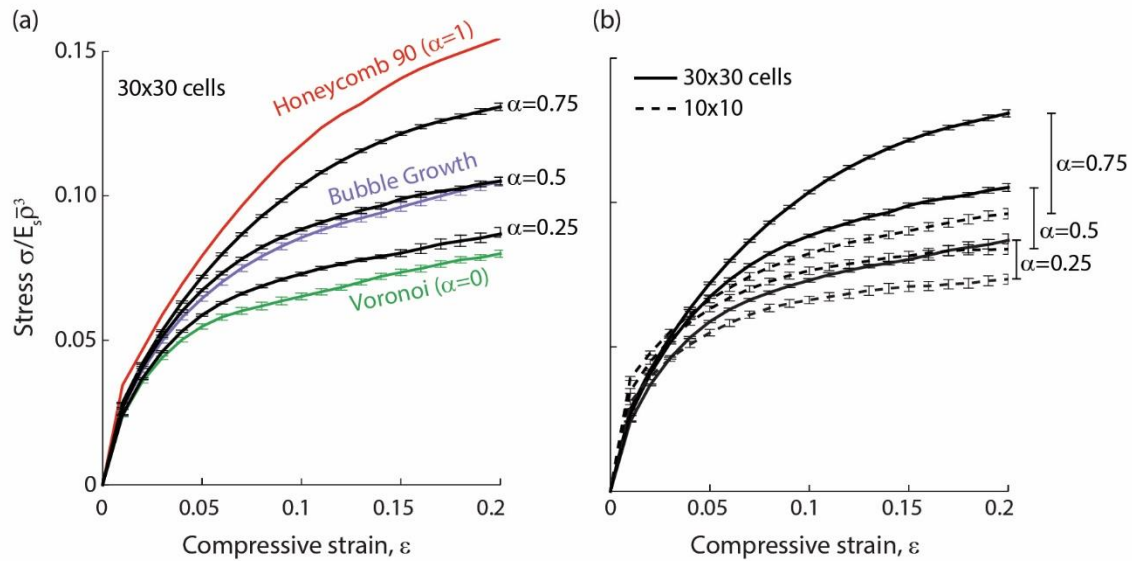


Figure 4.9: (a) Results for 30x30 cell foams are compared to responses of 30x30 cell foams generated using regularity parameters. (b) Results for 10x10 and 30x30 cell foams with varying regularity parameters show that foams with regular microstructures are more sensitive to boundary conditions.

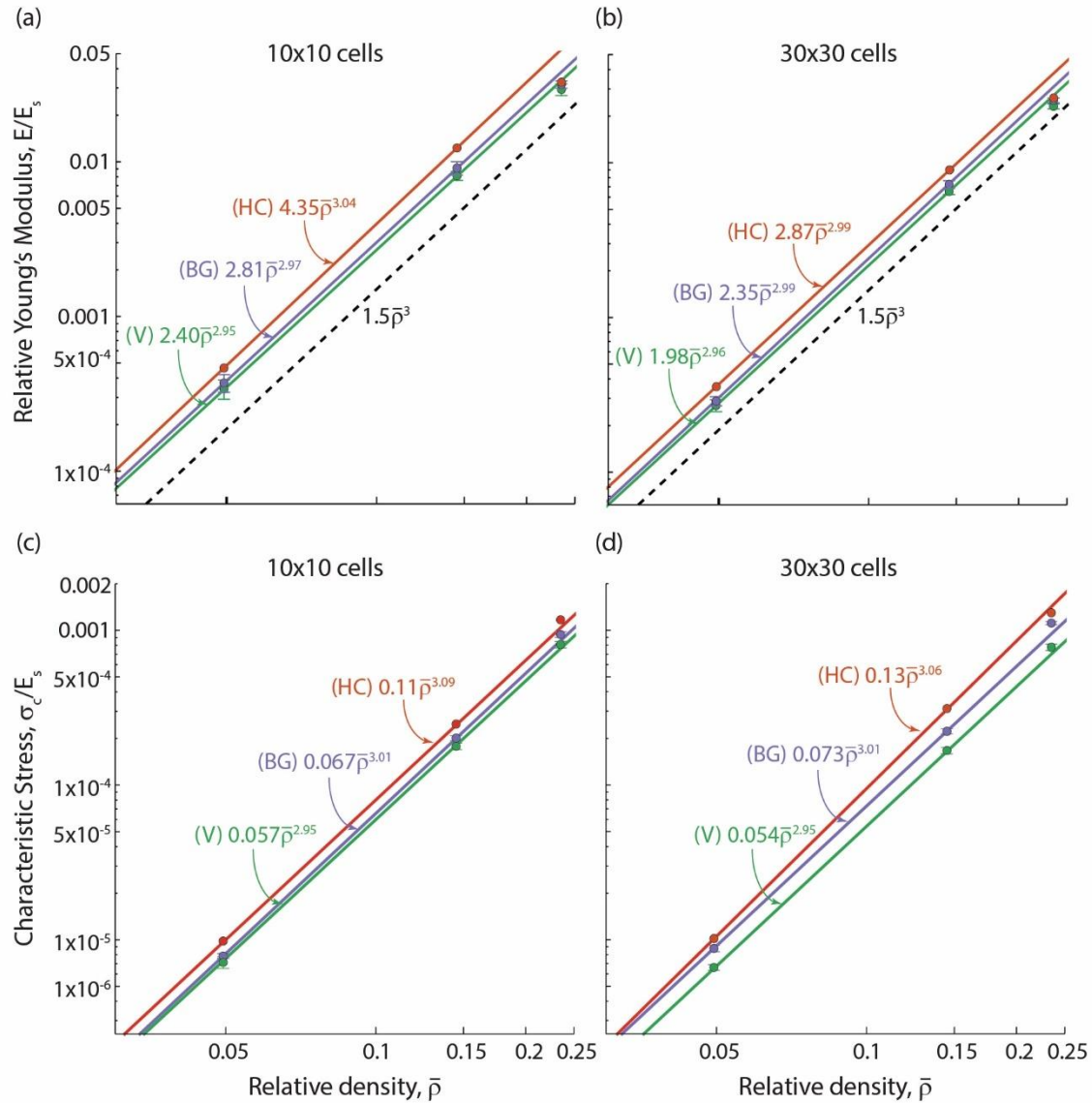


Figure 4.10: (a & b) Comparison of measured Young's modulus values for 10x10 and 30x30 cell foams with predictions from the Gibson-Ashby model (dashed line). (c & d) The characteristic stress is also plotted for each 10x10 and 30x30 cell foam. Red lines are for honeycombs (HC), purple is for bubble growth foams (BG), and green is for random Voronoi foams (V).

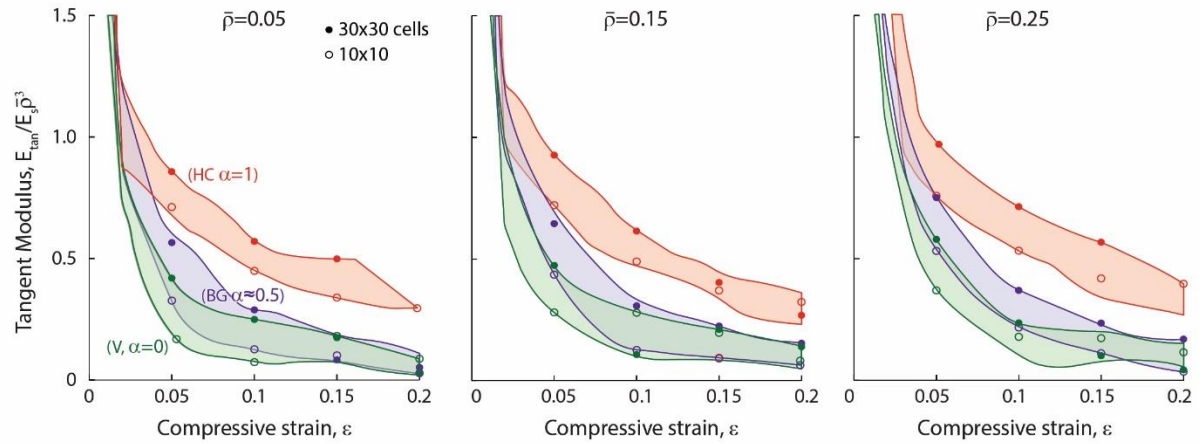


Figure 4.11: Normalized tangent moduli values are plotted for each foam type at three relative densities. Borders of each color outline the minimum and maximum values found from each foam type with different cell densities. Solid circles show measured values for 30x30 cell foams and open circles show the same for 10x10 cell foams at increments of 5% compressive strain.

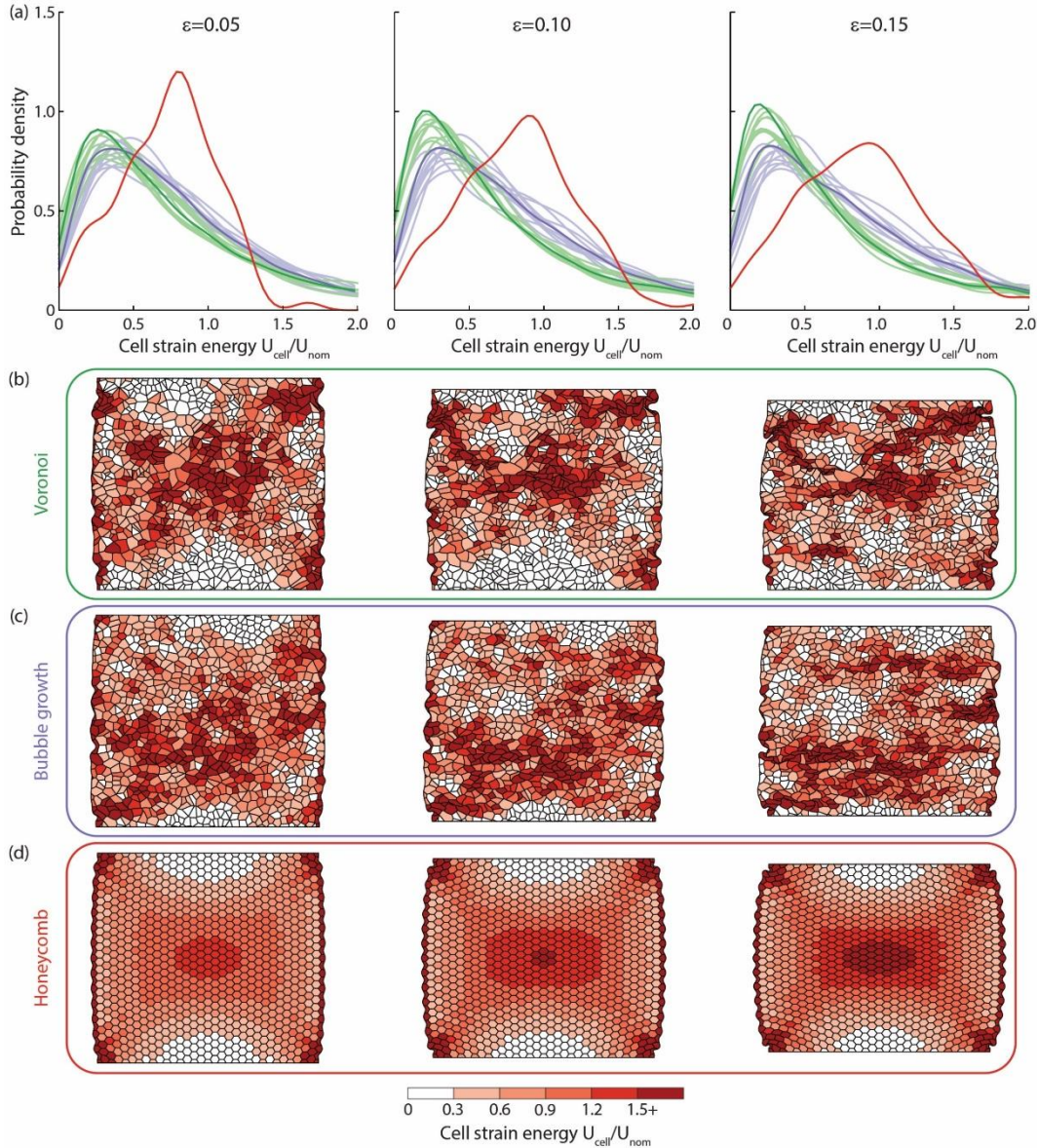


Figure 4.12: (a) Probability density functions are plotted for 30x30 cell Voronoi foams (light green), bubble growth foams (light purple), and honeycombs tested in two orientations (red and blue) at three compressive strains: $\varepsilon = 0.05$, 0.10 , and 0.15 . Dark green and purple curves show the cumulative probability density curves of 10 Voronoi and 10 bubble growth foams respectively. Deformation maps show the distribution and evolution of normalized cell strain energy in a (b) Voronoi foam, (c) bubble growth foam, and (d) honeycomb.

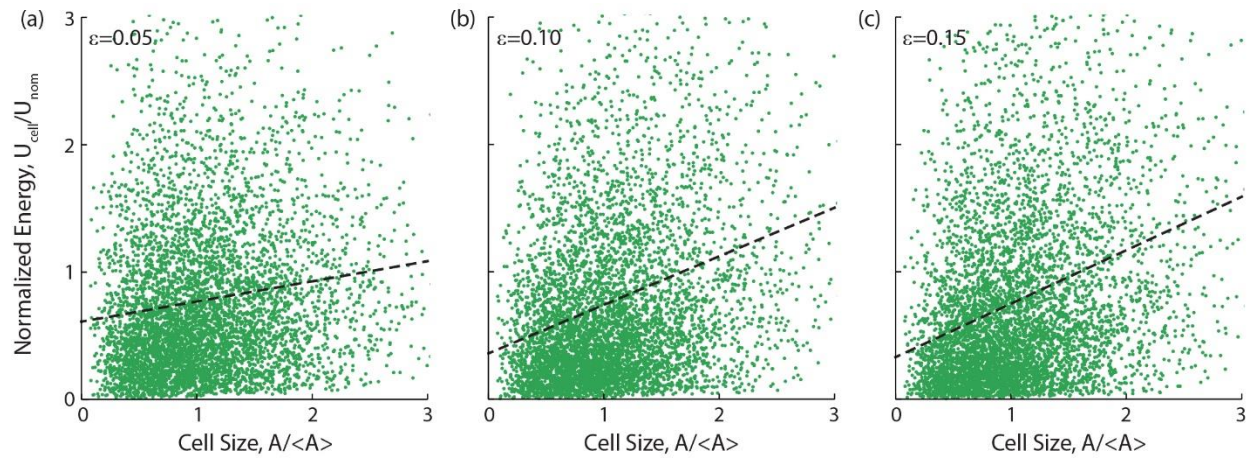


Figure 4.13: For all 30x30 cell Voronoi foams, normalized cell size is plotted against corresponding cell energies at three compressive strains: (a) $\varepsilon = 0.05$, (b) $\varepsilon = 0.10$, and (c) $\varepsilon = 0.15$. Fitted trendlines are plotted as dashed lines. The strength of correlation increases with compressive strain.

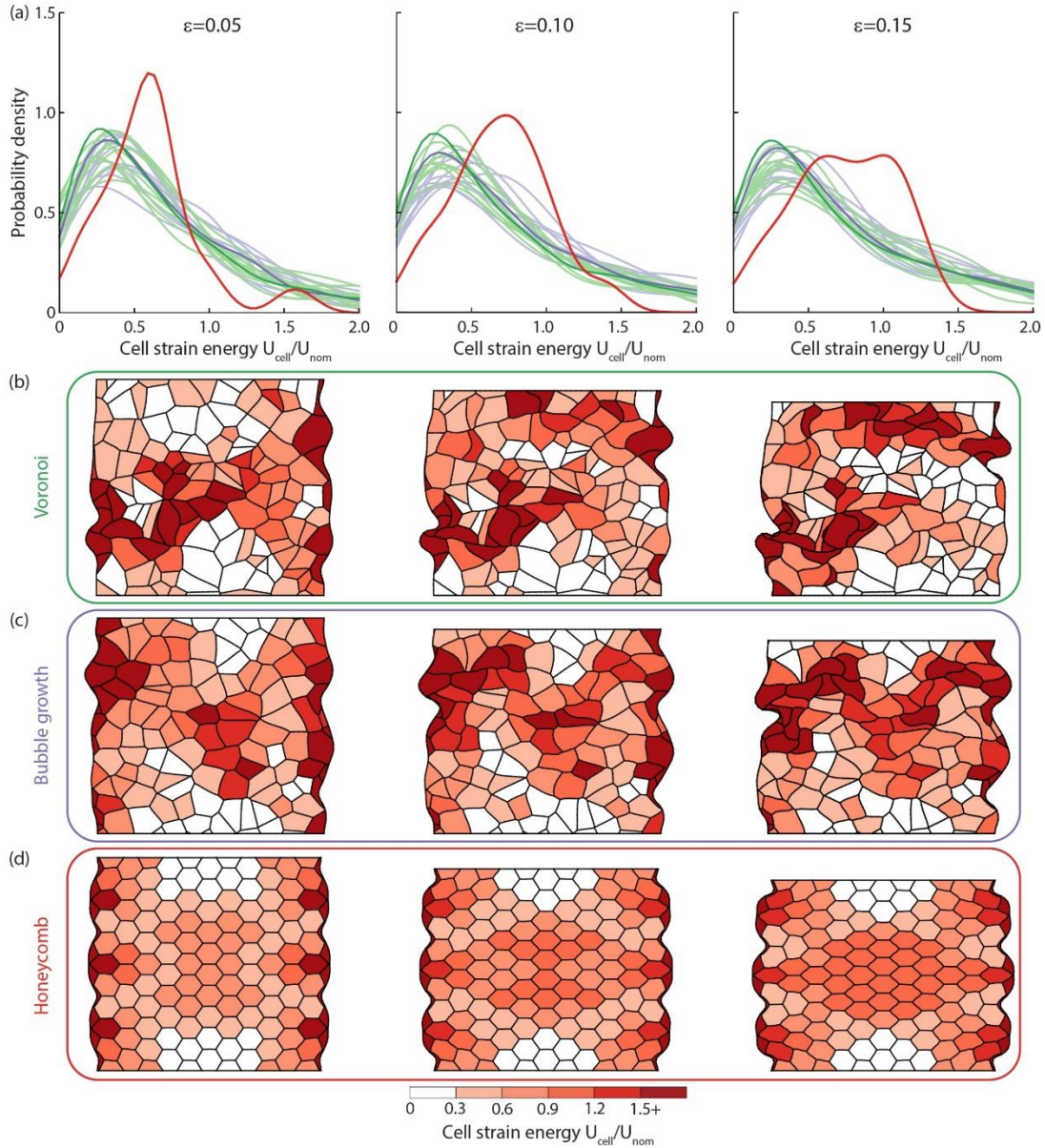


Figure 4.14: (a) Probability density functions are plotted for 10×10 cell Voronoi foams (light green), bubble growth foams (light purple), and honeycombs tested in two orientations (red and blue) at three compressive strains: $\varepsilon = 0.05$, 0.1 , and 0.15 . Dark green and purple curves show the cumulative probability density curves of 10 Voronoi and 10 bubble growth foams respectively. Deformation maps show the distribution and evolution of normalized cell strain energy in a (b) Voronoi foam, (c) bubble growth foam, and (d) honeycomb.

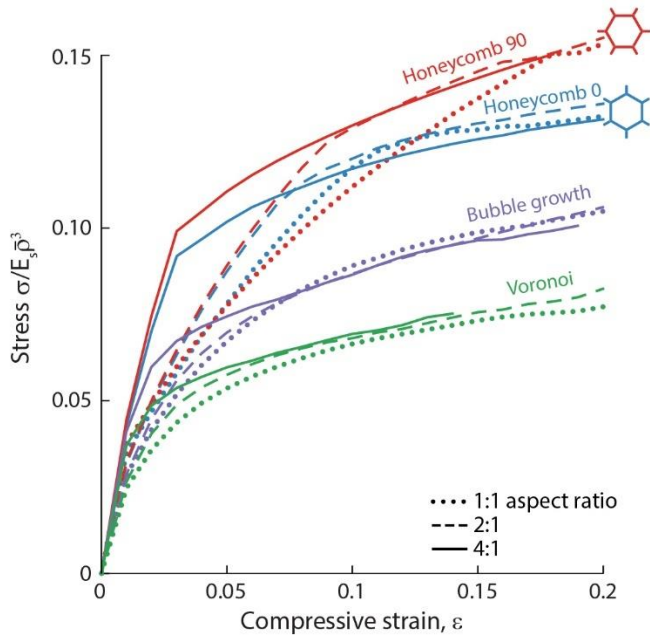


Figure 4.15: (a) Normalized stress-strain results for each of the four foam types at three aspect ratios. All results are for foams at 15% relative density. Voronoi and bubble growth results are averaged across 10 simulations. Honeycomb results are from single simulations.

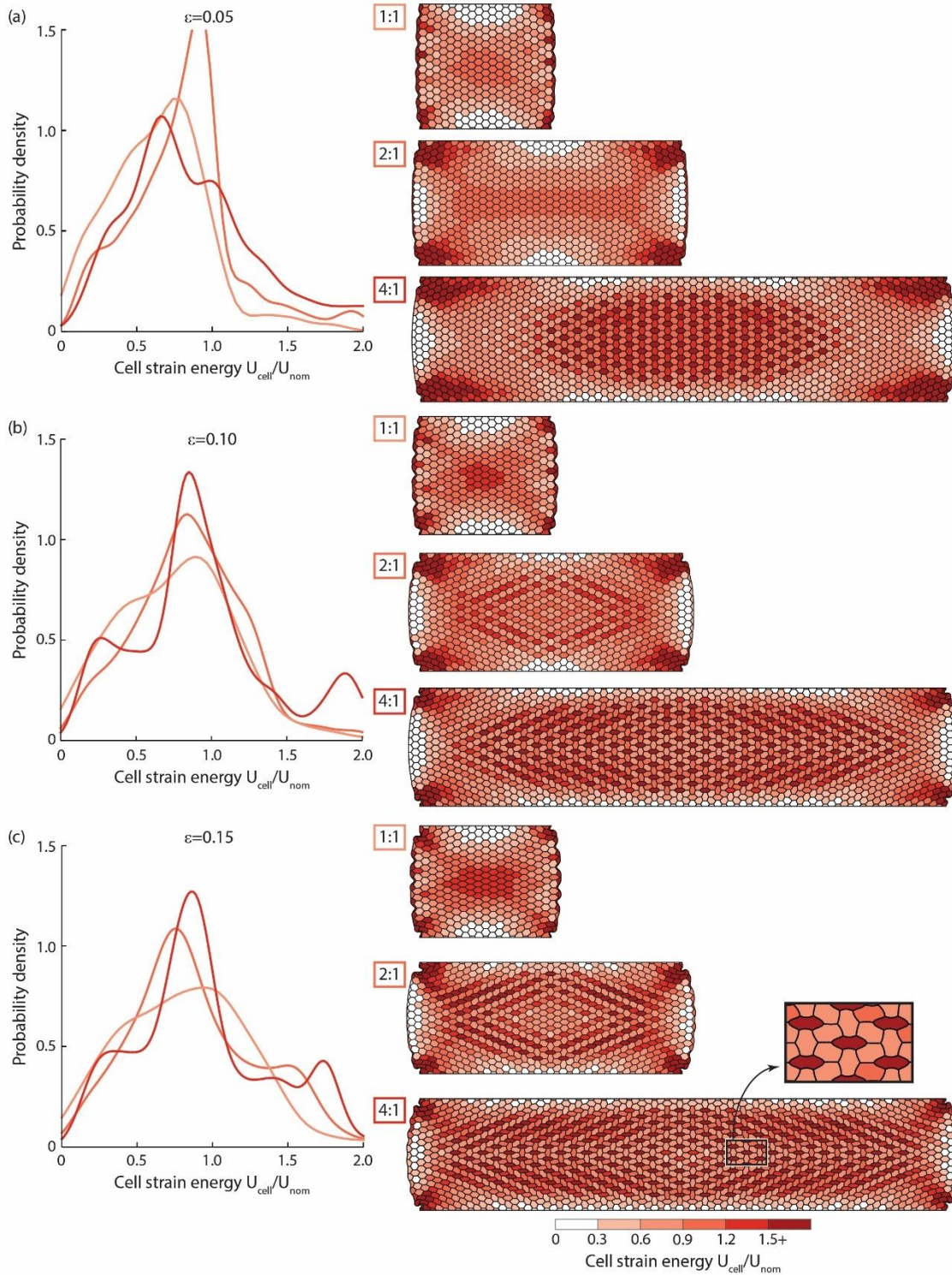


Figure 4.16: Probability density functions and deformation maps of Honeycomb 90 foams are plotted at three compressive strains: (a) $\varepsilon = 0.05$, (b) $\varepsilon = 0.10$, and (c) $\varepsilon = 0.15$. Deformation maps show the distribution and evolution of normalized cell strain energy in each foam and show the emergence of mode II buckling as foam aspect ratio increases. (Corresponding stress-strain curves are plotted in Fig. 4.15)

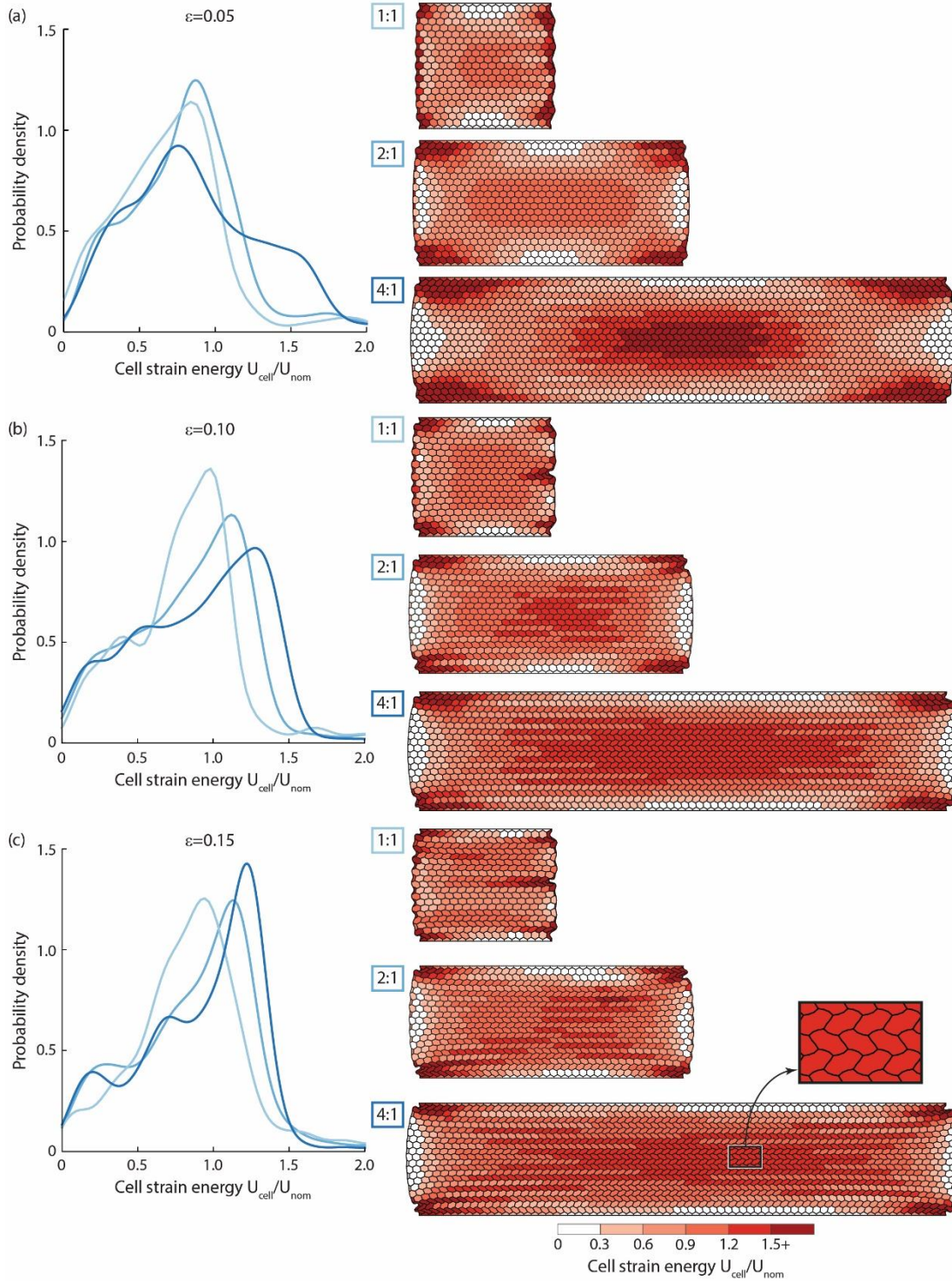


Figure 4.17: Probability density functions and deformation maps of Honeycomb 0 foams are plotted at three compressive strains: (a) $\varepsilon = 0.05$, (b) $\varepsilon = 0.10$, and (c) $\varepsilon = 0.15$. Deformation maps show the distribution and evolution of normalized cell strain energy in each foam and show mode I buckling occurring at lower compressive strains for larger foam aspect ratios. (Corresponding stress-strain curves are plotted in Fig. 4.15)

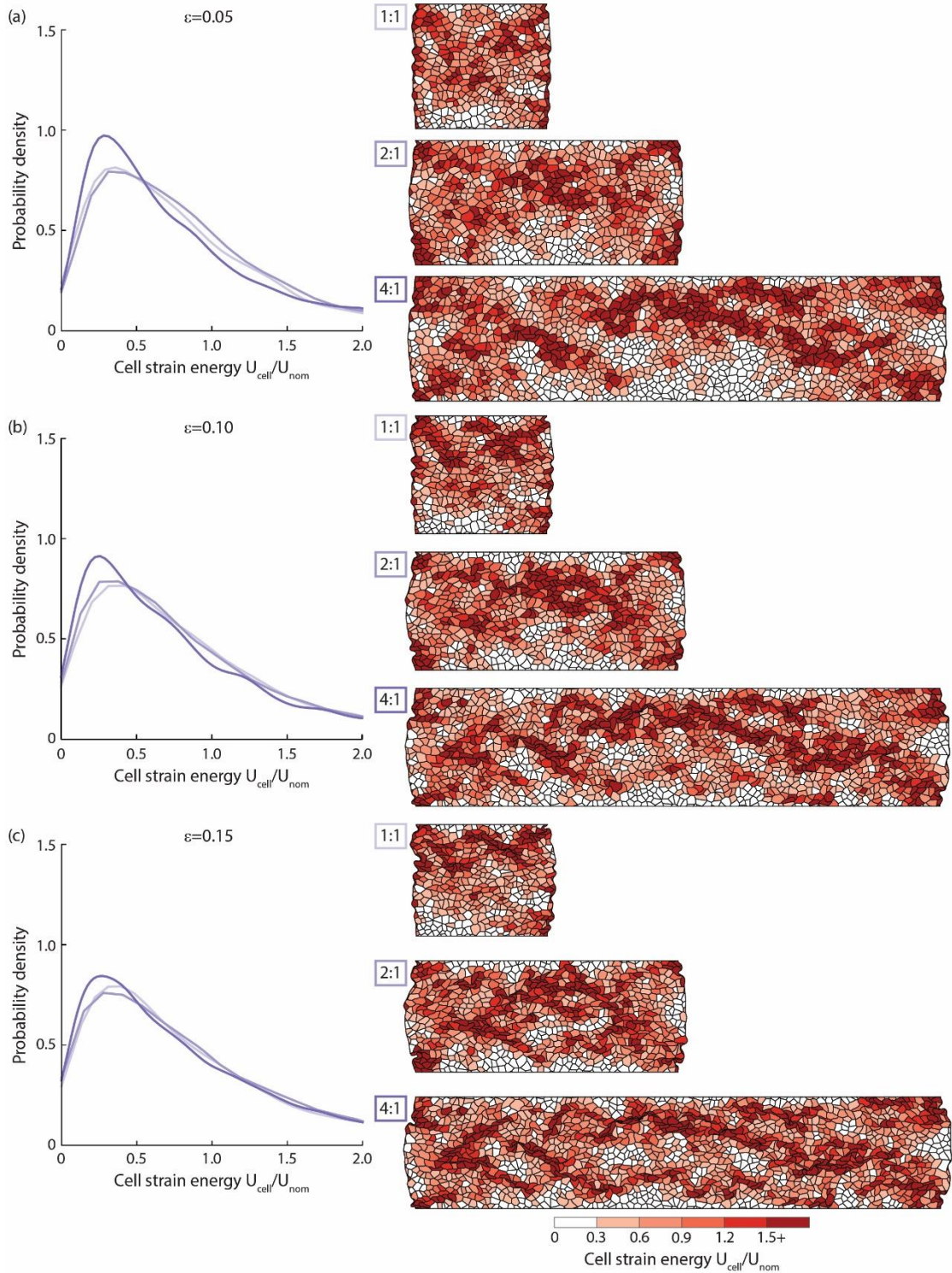


Figure 4.18: Cumulative probability density functions for sets of 10 bubble growth foams and representative deformation maps of are plotted at three compressive strains: (a) $\varepsilon = 0.05$, (b) $\varepsilon = 0.10$, and (c) $\varepsilon = 0.15$. Deformation maps show the distribution and evolution of normalized cell strain energy in each foam and show bands of cells with high normalized energies. (Corresponding stress-strain curves are plotted in Fig. 4.15)

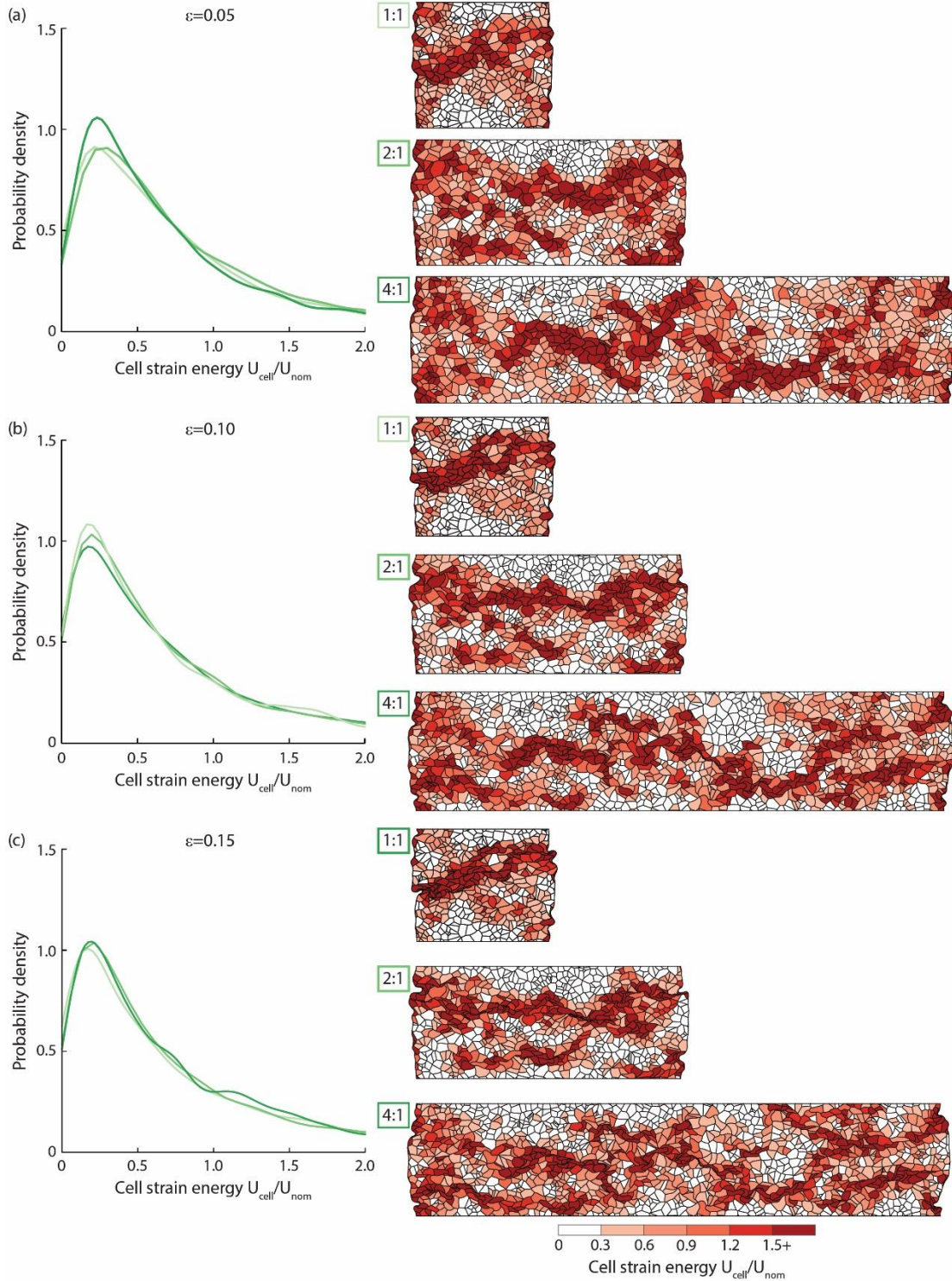


Figure 4.19: Cumulative probability density functions for sets of 10 Voronoi foams and representative deformation maps of are plotted at three compressive strains: (a) $\varepsilon = 0.05$, (b) $\varepsilon = 0.10$, and (c) $\varepsilon = 0.15$. Deformation maps show the distribution and evolution of normalized cell strain energy in each foam and show bands of cells with high normalized energies. (Corresponding stress-strain curves are plotted in Fig. 4.15)

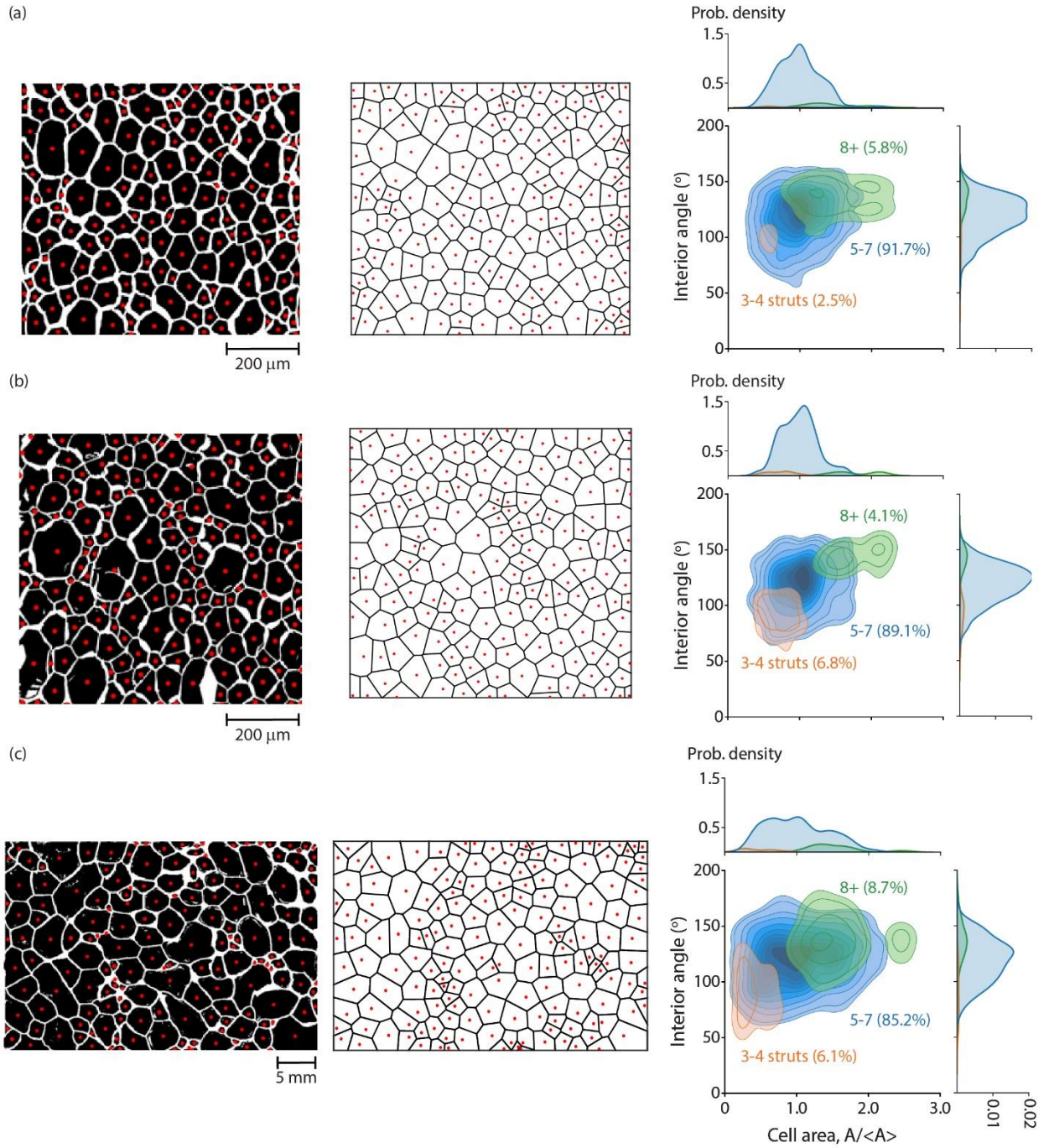


Figure 4.A1: Individual multivariate density plots for three real foams are created by analyzing Voronoi models of gas expanded (a & b) polymer foams²⁷ and a (c) metal foam²⁸.

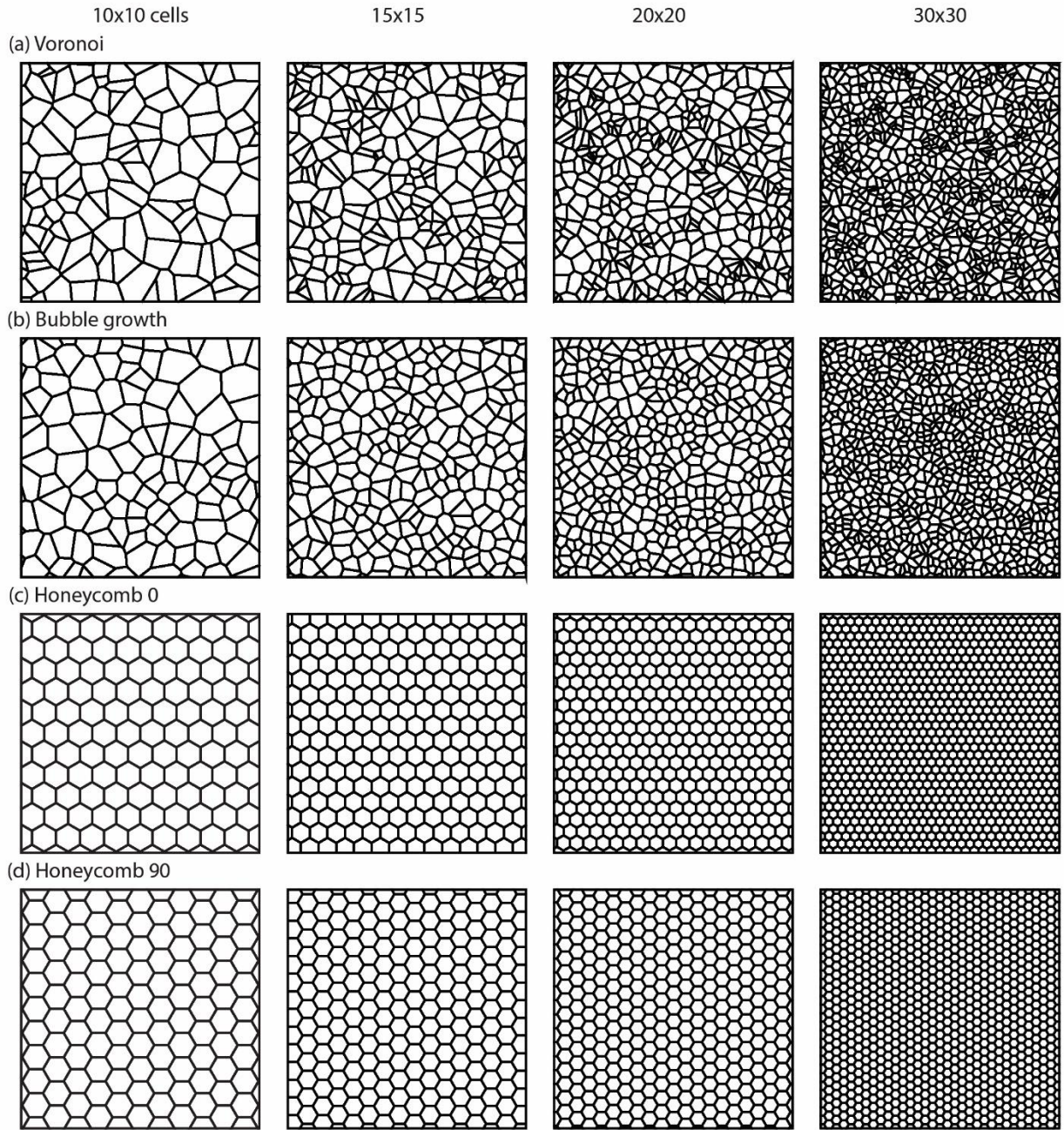


Figure 4.B1: Images of Voronoi, bubble growth, and honeycomb foams used in finite element simulations. Ten different sets of bubble growth and Voronoi foam were used at each relative density in this study. Honeycomb models were the same at each relative density.

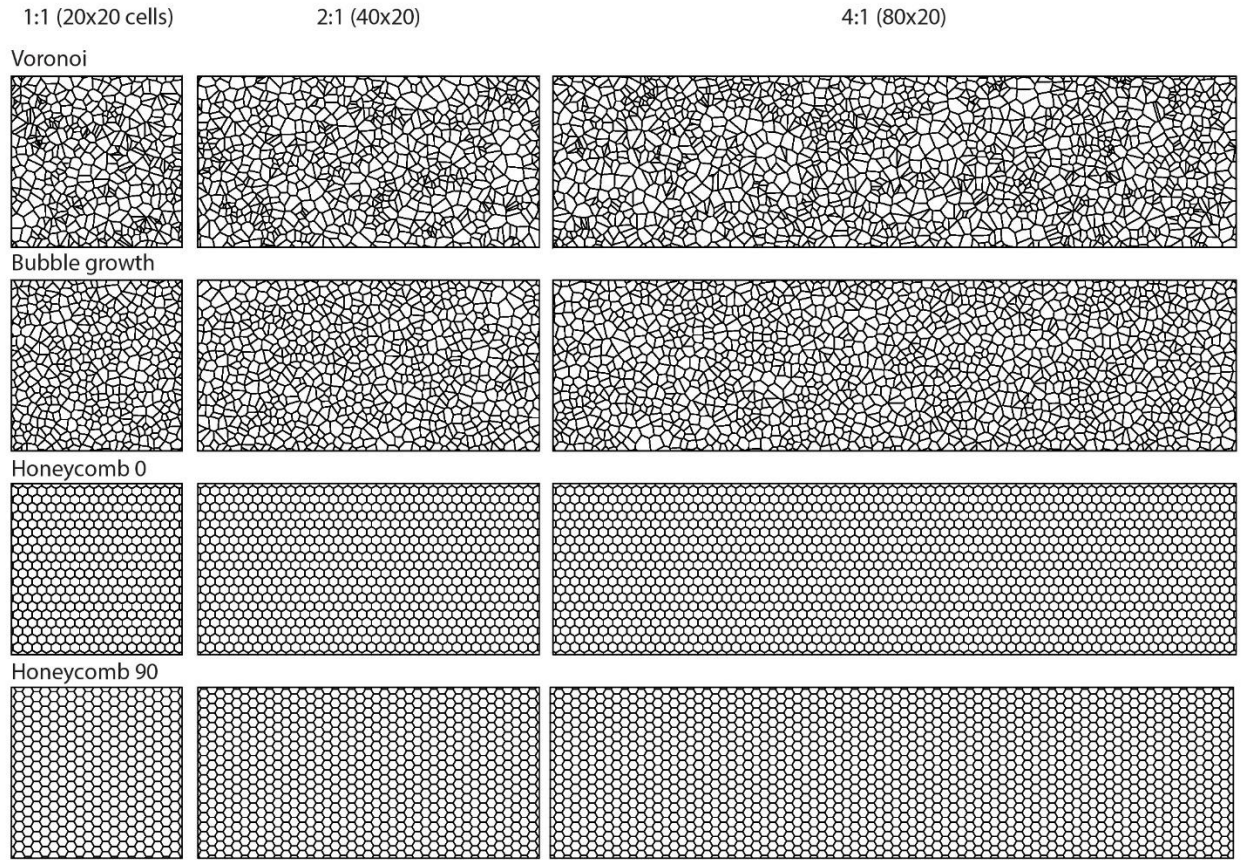


Figure 4.B2: Images of Voronoi, bubble growth, and honeycomb foams used in finite element simulations where the impact of microstructure on macroscopic foam dimensions was studied. Ten sets of bubble growth and Voronoi foam were used in this study.

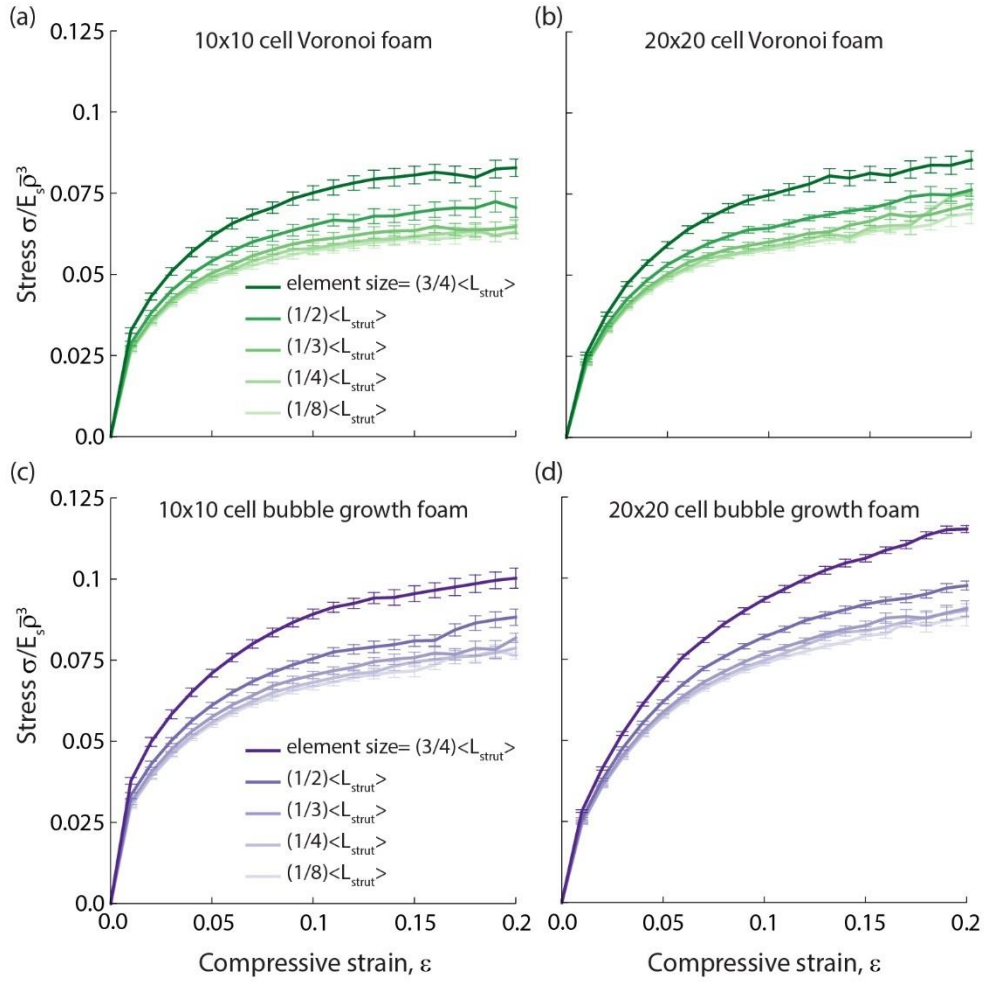


Figure 4.B3: Mesh convergence studies on two types of foams (Voronoi and bubble growth) with different cell densities (approx. 100 and 400 cells) show that the mechanical response converges to a common solution when the element size is approximately 1/3 of an average strut length. Each plotted response is an average of 10 simulations.

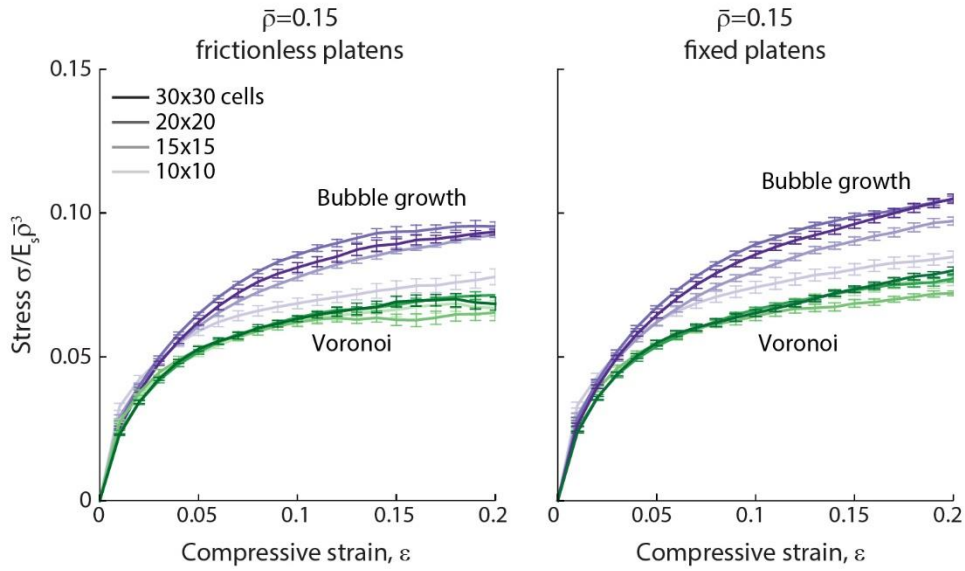


Figure 4.24: Results from bubble growth and Voronoi foam simulations using (left) frictionless platens and (right) fixed platens. Different shades of each color correspond to foams with different numbers of cells. Each curve shows the average of 10 simulations with standard error bars included.

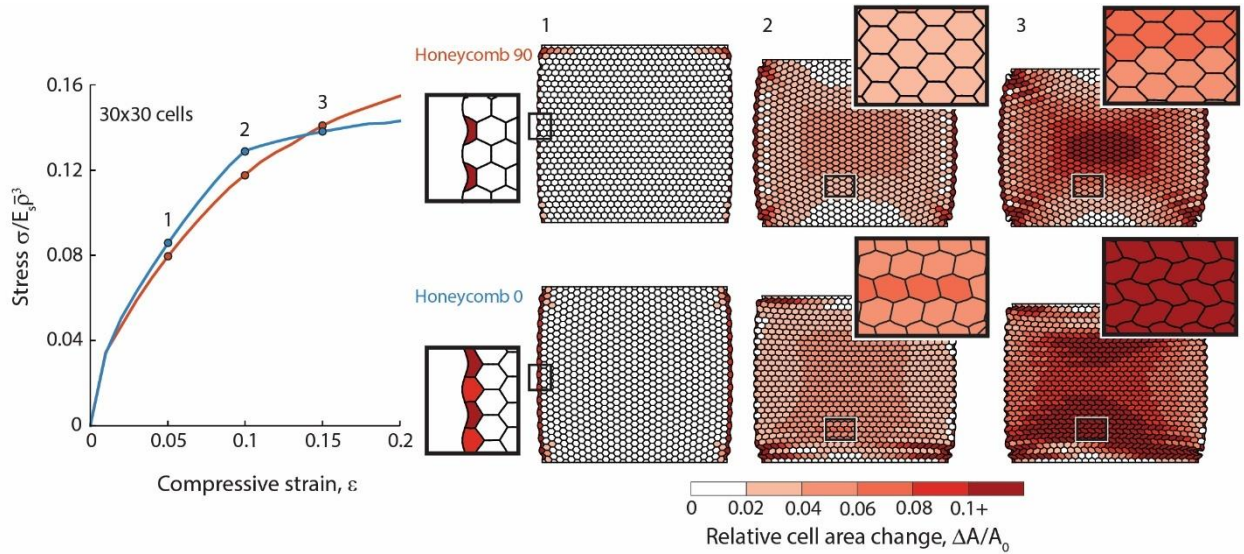


Figure 4.C1: Stress-strain curves for 30x30 cell honeycombs at $\bar{\rho} = 0.15$ are marked with three points of interest to show differences in deformation behavior. At each deformation step, cells are colored by their relative change in area, $\Delta A / A_0$.

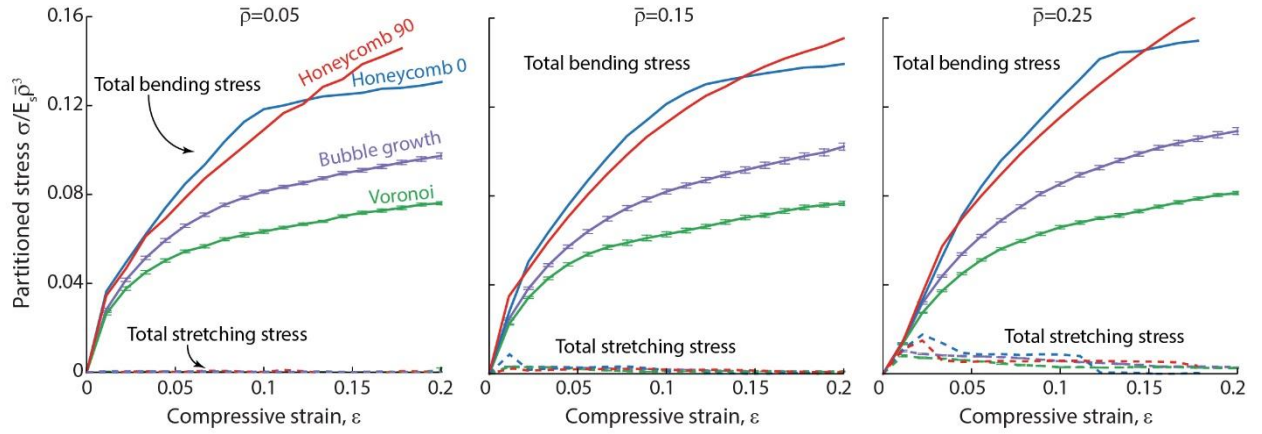


Figure 4.D1: Total bending and stretching stress contributions from all struts averaged over each 30x30 cell foam at (a) 5%, (b) 15%, and (c) 25% relative density. Solid lines show the bending component of the stress-strain response and dashed lines show the stretching component. Results indicate that differences in response are not due to differences in energy partitioning.

Chapter 5

Conclusions and Recommendations

5.1 General Conclusions and Impact

The overarching goal of the research in this dissertation was to identify and analyze concepts to tailor the compressive response of ordered lattices and stochastic foams. Resulting discoveries may expand the design space and attainable responses of cellular structures. A common approach was employed throughout: break the structure of interest down into fundamental structural components, understand the role of the components in the response, and identify which features can be modified to tailor the response in targeted ways.

In Chapter 2, the primary objective was to identify a design concept that allowed for high load-bearing capacity, high straining capacity, and strain reversibility. This was achieved by combining elements from tensegrity structures with those in periodic stretch-dominated lattices. The concept involved two materials with disparate properties: rigid polymers for struts that bear compressive loads and compliant elastomers for struts that are loaded in tension. The topology of the structure produced a stretching-dominated response, with stiffness and load-bearing capacity controlled by the tensile struts. Implementation of this concept requires special consideration of joint design: joints must enable both effective load transfer and strut rotation. For this reason, hinged joints were used in the current implementation. The resulting 2D bi-material structures were able to accommodate large macroscopic compressive strains through strut rotation at the joints and stretching of the tensile struts. The concept showed promise in attaining both high strength and straining capability.

Analytical mechanics models yielded a useful framework for predicting both the stress-strain response and the onset of failure. The analyses showed that the compressive response

depends sensitively on the angle of inclined (compressive) struts and the stiffness of the transverse (tensile) struts. Increasing either variable results in an increased load bearing capacity of the bi-material lattice. The analysis was also useful for developing design guidelines to prevent common failure modes, focusing on properties of the constituent materials, strut morphology, and network morphology. To prevent strut rupture, the ductility of transverse (tensile) struts must be considered. Increased ductility of struts is required for lattices with high inclination angles (compressive struts at $\theta_0 \geq 65^\circ$) compared to that required for lattices with low inclination angles ($\theta_0 \leq 55^\circ$). To prevent compressive failure modes such as strut buckling and strut yielding, *ratios* of characteristics are important to consider: strut material stiffness ratio, E_c / E_t , strut thickness ratio, t_c / t_t , compressive strut slenderness ratio, t_c / L_c , and the ratio between compressive strut yield strength and tensile strut stiffness, $\sigma_{y,c} / E_t$. To achieve the higher load bearing capacity afforded by lattices with high inclination angles, increasing the numerator of each ratio is necessary.

The specific lattice design employed in this part of the study had two shortcomings. The first was the need for large macroscopic changes in lateral dimensions when the lattice was compressed. This introduced large effects of friction along the loaded surfaces. The second shortcoming was undue constraint at the joints leading to some strut bending.

In Chapter 3, the 2D bi-material concept was extended to 3D. Deficiencies in the original 2D design were addressed by selection of a network topology that keeps lateral displacements entirely within the body of the lattice (not affecting the external surfaces) and through the use of knob-and-socket joints with small gaps to minimize rotational constraint. The resulting 3D lattices deformed stably up to high strains and achieved the objective response. Characteristics of the compressive response were similar to those of the 2D lattices:

initial hardening due to stretching of the tensile struts followed by gradual softening due to progressive changes in strut inclination angle. This type of response is promising for impact applications.

The initial 3D designs were modified to further tailor compressive response. Design modifications focused on the elastomeric (tensile) component, since this component governs the compressive response. In one design, curved struts were added to each of the three straight struts (from the previous design). The intended goal was to extend the hardening regime by adding elements that initially carry little load but progressively stiffen and contribute to the macroscopic response at higher compressive strains. Results were less favorable than those predicted by analytical models, and the additional material added for curved struts was inefficiently utilized.

In a second design iteration, a greater expansion of the design and property space was achieved using elastomeric sheets in place of struts, exploiting the stiffer biaxial tensile response of elastomers. This design led to a twofold increase in load bearing capacity. However, both the experimental measurements and the finite element simulations show that this structure is more susceptible to rupture because of the high strain concentrations in the transition regions. This problem was partially mitigated by grading the sheet: essentially moving material from regions of low strain energy to regions of high strain energy. The result was a more uniform distribution of strain energy density, indicating a lower likelihood of rupture. This conclusion was supported by experimental measurements on bi-material structures with graded sheets. More broadly, the results of this study demonstrate the potential for creatively combining elements of open and closed-cell lattices along with multiple materials in further tailoring mechanical response.

To extend unit cell designs to larger multi-cell structures, a tiling concept was proposed. This concept involves arranging unit cells so that struts within one cell do not make contact with those in neighboring cells as the structure is compressed. This concept allows for stable axial deformation of the cell array and prevents large macroscopic changes of the entire structure thereby achieving a plastic Poisson's ratio of zero. It raises some questions, however, about the stability of the structures when subjected to lateral loads. This may require more concepts in tiling and joining: a subject of possible future work.

Shifting from ordered lattices to stochastic foams, the primary objective of the work presented in Chapter 4 was to establish connections between microstructural features and the mechanical response of finite-sized foams. Approaches based on multivariate scatter plots and associated probability density plots were introduced as a means to better visualize distributions in microstructural characteristics and their relations with one another. Characteristics of interest included cell area, number of struts per cell, and cell interior angles. Analyses on *real foams* helped to identify a baseline of realistic features, notably cells having between 5 and 7 struts and interior angles greater than 90° . Using the analysis on *foam models* helped to make connections between regular or irregular microstructures and specific microstructural features. Moving from irregular to regular microstructures results in a reduction of unrealistic features, i.e., cells having 3-4 struts and low interior angles ($\theta \leq 90^\circ$).

Results from finite element simulations revealed that polydispersity in cell size has a large effect on the stress-strain response. Ordered honeycombs, having uniform cell size, exhibit the strongest response, followed by bubble growth-generated foams (cell size coefficient of variation ≈ 0.32), and then Voronoi tessellated foams (cell size $CV \approx 0.52$). Strain energy maps show that a wide distribution in cell sizes results in larger-than-average

cells accommodating deformation while smaller-than-average cells deform less. The nonuniform distribution in strain energy density results in a softer compressive response. Broadly, these results elucidate observations made in previous studies on the effects of irregular and regular microstructures on the compressive response. Increasing regularity indeed leads to a stronger compressive response, an effect caused by tighter cell size distributions and not by other features that vary with regularity.

Additionally, the compressive response of foams with tighter distributions in cell size was found to be more sensitive to boundary conditions. For these foams, the compressive stress increases as the number of cells in the model increases; the results converge for models having containing arrays of 30x30 cells. Conversely, foams having wider distributions in cell size, like the Voronoi foams, show only weak sensitivity to number of cells. These results highlight the importance of cell size polydispersity in applications where only small numbers of cells span a part dimension.

Nuanced changes in the sensitivity of response to cell size polydispersity arise for foams with high aspect ratios. For foams with uniform cell size, e.g., honeycombs, increasing the foams aspect ratio from 1:1 to 4:1 leads to a more abrupt transition from the linear domain to the stress plateau. This type of transition may not be ideal for impact scenarios such as those obtained during running. Here, the more gradual transition obtained in foams with moderate distributions in cell size may be preferable. Collectively, the results demonstrate the coupled effects of cell size polydispersity, boundary conditions, and foam size on compressive response.

5.2 Future Work

Three specific research problems are proposed for future work. The first is to build upon quasi-static results and examine the role of dynamic loading on the mechanical response of multi-material lattices. Rate effects would naturally arise from the intrinsic rate sensitivity of the constituent materials. Additional effects may arise from the rate sensitivity of frictional sliding within bi-material joints. Finally, for very high loading rates, effects of internal inertia and shock waves may come into play.

A second area of future study stems from recognizing that bi-material structures greatly extend the design landscape of lattices. New considerations include: (i) strut material properties, especially ratios between properties, (ii) joint design, surpassing the limits of rigid connections, and (iii) phase distribution to describe how different strut populations are distributed within a lattice. With increasing design variables, an area of future work would be in the generalization and formalization of descriptions of multi-material lattices. This could include devising a unifying taxonomy of lattice structures, building on the work of Zok et al.¹ In that work, concepts from crystallography and geometry were used to describe nodal locations and connectivity of struts. The resulting taxonomy was built on a hierarchy of geometric complexity, starting with elementary cubic lattices, then moving to non-cubic and compound lattices. Existing descriptions of *single-material* compound lattices may prove to be a useful starting point for descriptions of periodic bi-material lattices.

A third area relevant to design of stochastic polymer foams would involve the incorporation of the intrinsic *viscoelastic* characteristics of the constituent material into models of macroscopic cyclic response. In the past, effects of viscoelasticity have been tied to performance of foams in athletic shoes, especially with respect to running economy, comfort,

and injury prevention ²⁻⁵. Viscoelastic effects could be implemented in the types of models used here through, for example, the standard linear solid model commonly employed in the polymer research community. This could reveal additional coupled effects of intrinsic material properties (including damping), foam architecture, foam size, and macroscopic response. In turn, these effects might lead to new strategies to tailoring foam properties.

References

1. Zok, F. W., Latture, R. M. & Begley, M. R. Periodic truss structures. *J. Mech. Phys. Solids* (2016). doi:10.1016/j.jmps.2016.07.007
2. Worobets, J., Wannop, J. W., Tomaras, E. & Stefanyshyn, D. Softer and more resilient running shoe cushioning properties enhance running economy. *Footwear Sci.* 6, (2014).
3. Frederick, E. C., Howley, E. T. & Powers, S. K. Lower Oxygen Demands of Running in Soft-Soled Shoes. <http://dx.doi.org/10.1080/02701367.1986.10762196> 57, 174–177 (2013).
4. Sinclair, J., McGrath, R., Brook, O., Taylor, P. J. & Dillon, S. Influence of footwear designed to boost energy return on running economy in comparison to a conventional running shoe. *J. Sports Sci.* 34, (2016).
5. Hébert-Losier, K. & Pamment, M. Advancements in running shoe technology and their effects on running economy and performance – a current concepts overview. (2022).